First Principles Theory of the Lattice Thermal Conductivity of Semiconductors

Author: Alistair Norman Ward

Persistent link: http://hdl.handle.net/2345/748

This work is posted on eScholarship@BC,
Boston College University Libraries.

Boston College

The Graduate School of Arts and Sciences

Department of Physics

FIRST PRINCIPLES THEORY OF THE LATTICE THERMAL
CONDUCTIVITY OF SEMICONDUCTORS

A dissertation

by

ALISTAIR WARD

submitted in partial fulfillment of the requirements

for the degree of

Doctor of Philosophy

June 2009

First principles theory of the lattice thermal conductivity of semiconductors

Alistair Ward

Advisor: David Broido

Abstract

Using density functional perturbation theory and a full solution of the linearized phonon Boltzmann transport equation (BTE), a parameter-free theory of semiconductor thermal properties is developed. The approximations and shortcomings of previous approaches to thermal conductivity calculations are investigated. The use of empirical interatomic potentials in the BTE approach is shown to give poor agreement with measured values of thermal conductivity. By using the adiabatic bond charge model, the importance of accurate descriptions of phonon dispersions is highlighted. The extremely limited capacity of previous theoretical techniques in the realm of thermal conductivity prediction is highlighted; this is due to a dependence on adjustable parameters.

Density functional perturbation theory is coupled with an iterative solution to the full Boltzmann transport equation creating a theoretical construct where thermal conductivity prediction becomes possible. Validation of the approach is demonstrated through the calculation of a range of thermal properties for a set of polar and non-polar semiconductors which are compared with measured values. The agreement between theory and measurement is very good, confirming the promise of the theoretical approach.

Due to the significant computational effort required by the parameter-free calculations, new forms for room temperature relaxation time approximations are derived. The resulting forms produce thermal conductivity values in very good agreement with the ab initio data across a wide temperature range. It is therefore shown that accurate relaxation time approximations can be

developed, fixing the adjustable parameters to the ab initio theory avoiding any comparison with measured data. This approach improves the accuracy of phonon relaxation times compared with previous models.

1   Contents

2 Introduction

The lattice thermal conductivity, κ_L of semiconductor materials has been studied for many decades using a multitude of theoretical techniques.[1-7] The ultimate goal is the development of a predictive theory for κ_L. As the manufacture and study of nano-scale devices progresses, a microscopic understanding of phonon transport is required. Devices such as novel 3D multilayer electronics, silicon-on-insulator circuits etc. require an understanding of phonon transport[8]. Another rapidly developing field is that of thermoelectrics.[9,10] The figure of merit, ZT, is a measure of the efficiency of a thermoelectric device and is given by

$$ZT = \frac{S^2 \sigma T}{\kappa_e + \kappa_L} \qquad \text{3.1-1}$$

where T is the temperature, S is the Seebeck coefficient, σ is the electrical conductivity and the thermal conductivity has been separated into an electronic, κ_e and lattice contribution, κ_L. For semiconductors, the electronic contribution to the thermal conductivity is much smaller than the lattice contribution, $\kappa_e \ll \kappa_L$ and so only the lattice contribution need be considered. The development of new material structures to increase ZT requires an understanding of and ideally an accurate prediction tool for κ_L.

At room temperature, where κ_L of semiconductors is dominated by three-phonon scattering, an exact solution of the phonon Boltzmann transport equation (BTE) and accurate microscopic descriptions of the interatomic forces are required. This is a very complex problem that, historically, could not be tackled directly. Instead, the Debye approximation was commonly used, where linear dispersions were taken for the acoustic branches (optic branches were omitted from the calculations) and inelastic phonon-phonon scattering was approximated using a relaxation time approximation (RTA).[1-3] The resulting calculations were tractable, but the restrictive approximations and the necessary adjustable parameters ensure that the method has limited predictive capacity.

A full solution to the phonon BTE was developed[6] and heat transport in diamond structure materials studied. The atomic interactions were modeled using a central potential model and a set of adjustable parameters. The next level of sophistication from the RTA is to directly calculate the microscopic interatomic forces using empirical interatomic potentials (EIPs) in conjunction with the BTE[7]. Through symbolic differentiation, both the harmonic and anharmonic interatomic forces can be determined and the BTE solved. As part of this study, a set of EIPs are used to calculate these forces and ultimately κ_L. Comparison of the results of these calculations with experimental data shows poor agreement due to the potentials' failure to accurately describe the phonon dispersions and anharmonic forces. The EIPs also depend on a set of adjustable parameters, which eliminates this method's predictive capacity.

Another approach to calculating κ_L involves molecular dynamics simulations that also depend on EIPs.[4,5] At high enough temperatures where quantum effects are no longer important, this method is very useful; however, its dependence on adjustable parameters means it also cannot be used as a predictive tool.

The failure of the EIPs to accurately describe the phonon dispersions is addressed in this study by using the adiabatic bond charge (ABC) model,[11,12] which succeeds in replicating the observed flattening of the transverse acoustic branches. A drawback of this model is that it does not provide a description of the crystals anharmonic forces. Considering only nearest-neighbor central force interactions, the anharmonicity is treated with the addition of a single adjustable parameter.[13] Combined with the BTE, the κ_L of Si/Ge and GaAs/AlAs superlattices are studied as part of this dissertation and compared with results using a constant relaxation time approximation (CRTA) and a representative EIP. The accurate description of phonon dispersions resulting from the ABC model leads to significantly different behavior than that predicted with both the EIP and the CRTA. The calculations also demonstrate that the strength of extrinsic interface scattering within superlattices is larger than previously estimated.[14] Despite the successes of the ABC model, it is still limited by the use of adjustable parameters and is consequently unable to provide the desired prediction capability.

The power of density functional theory (DFT) as an accurate method of calculating the electronic properties of materials for which electron exchange and correlation effects are relatively weak is well established.[15,16] The linear response of the electron density functional to lattice distortions is accessible through density functional perturbation theory (DFPT)[17] and the "2n+1" theorem.[18] These methods can be employed to accurately derive both the harmonic and third-order anharmonic interatomic force constants.[17,19] By coupling together the power of these "ab initio" techniques and an iterative solution to the phonon BTE equation, a theoretical framework in which thermal properties can be calculated *without* adjustable parameters is developed within this dissertation. To validate the theory, thermal properties of a group of polar and non-polar semiconductors are calculated and show very good agreement with experimental measurements. This establishes the developed theory as a predictive tool capable of performing accurate calculations of the *intrinsic* part of κ_L for newly studied materials.

The computational demands of the ab initio BTE approach are formidable. One major attraction of the relaxation time approximation (RTA) is its computational simplicity. Coming full circle, the final chapter of this dissertation uses the ab initio BTE theory to develop new RTAs that are valid at room temperature and above and do not rely on the restrictive approximations previously used. The usual method of omitting optic phonons from calculations is shown to be inaccurate and the crucial role they play in thermal transport is highlighted. The relaxation time forms and parameters are derived in comparison with the ab initio BTE data and so, while adjustable parameters exist, they are fixed by comparison with the parameter-free theoretical approach, not experimental data. The temperature dependence of κ_L is compared with ab initio results over a wide temperature range and the new RTA forms perform extremely well. Thus, physically reasonable RTAs can be developed without comparison to experimental data.

3 Boltzmann transport equation

3.1 Lattice thermal conductivity

Before undertaking a theoretical analysis of the lattice thermal conductivity, κ_L, its temperature dependence can be described qualitatively with reference to the experimental data of ref. 20 shown in Figure 3-1.
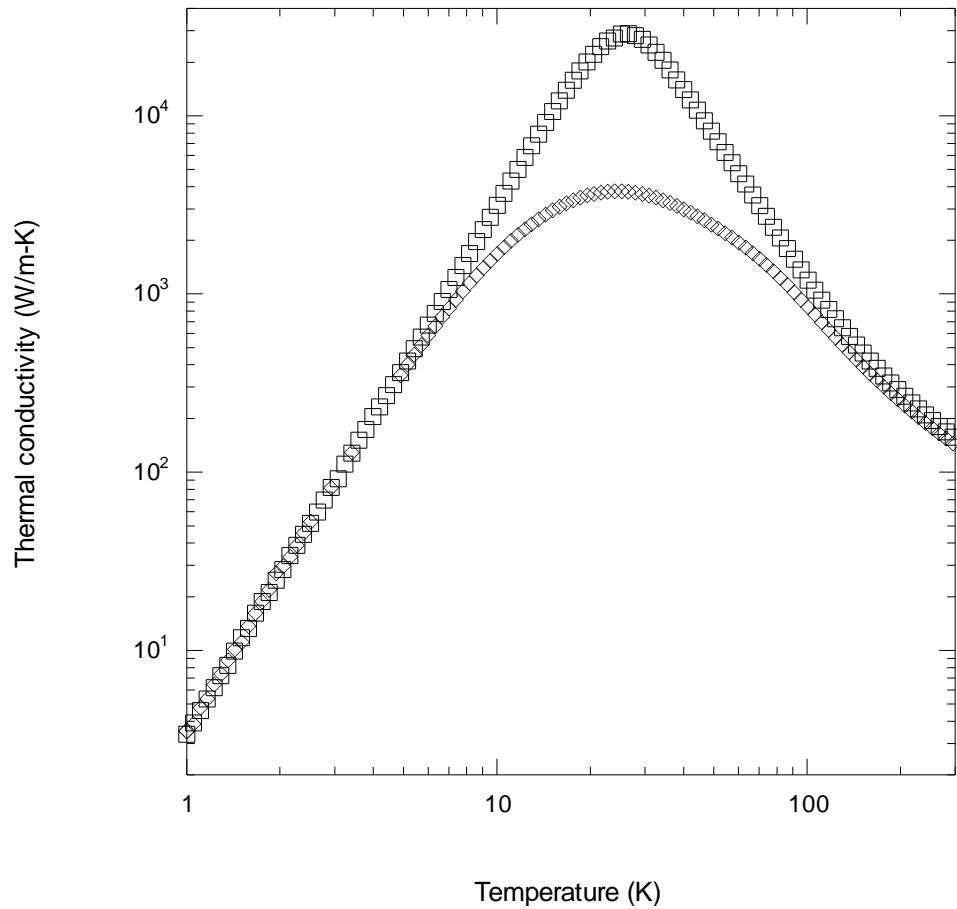
Figure 3-1; The temperature dependence of the lattice thermal conductivity of silicon (ref. 20). Open squares represent κ_L of isotopically enriched silicon and the open diamonds are for naturally occurring silicon.

At low temperatures, the phonon mean free path is of the order of the sample dimensions and phonon-phonon scattering is negligible. The scattering time associated with impurity and boundary

scattering is temperature independent and so the temperature dependence of κ_L is dictated by the specific heat, which varies as T^3 at low temperature.

With increasing temperature, the phonon mean free path becomes of the order of the spatial distribution of impurities in the crystal. Impurity scattering becomes more important, specifically in the region of the peak in κ_L (at approximately 30K in silicon). The height of this peak is dictated by the concentration (and associated mass differences) of impurities in the crystal. This effect can be seen in the two data sets in Figure 3-1 which are for measurements of isotopically enriched (open squares) and naturally occurring (open diamonds) silicon.

At temperatures greater than the peak, phonon-phonon scattering becomes increasingly important and ultimately comes to dominate κ_L. At these higher temperatures, the temperature dependence of κ_L is dictated by the scattering time defined by phonon-phonon scattering. a $T^{-\delta}$ dependence, where $\delta \approx 1$.

These mechanisms are discussed in more detail in the following sections (specifically 3.4, 3.8 and 3.9). The vast majority of the work in this dissertation is directed towards the study of phonon-phonon scattering at room temperature and above. This mechanism is an intrinsic property of the crystal that is present regardless of the dimensions and purity of the crystal.

3.2 Heat transport

In a material in which a thermal gradient ∇T exists, heat is transported through the crystal by both the electrons and crystal lattice vibrations. For semiconductors, the proportion of heat transported by the electrons is small and so the lattice vibrations, quantized into phonons are the dominant thermal transport mechanism. A phonon in branch j with wavevector $\vec{q}$ contributes $\vec{Q}_j^p(\vec{q})$ to the heat current, where

$$\vec{Q}_j^p(\vec{q}) = \hbar\omega_j(\vec{q})\vec{v}_j(\vec{q}) \qquad \text{3.2-1}$$

5

where $\omega_j(\vec{q})$ is the frequency and $v_j(\vec{q})$ is the group velocity of the phonon. If the number of phonons in this branch is given by a distribution function, $n_j(\vec{q})$, then the heat flow per unit volume of the crystal due to all phonons modes is

$$\vec{Q}_j(\vec{q}) = \frac{1}{V} \sum_{j,\vec{q}} \hbar\omega_j(\vec{q})\vec{v}_j(\vec{q})n_j(\vec{q})$$

3.2-2

This heat current is related to the temperature gradient through Fourier's law; the constant of proportionality being defined as the thermal conductivity matrix, $\kappa_{\alpha\beta}$. Thus for a temperature gradient in the βth direction, the thermal current in the αth direction is given by

$$Q_{j\alpha}(\vec{q}) = -\sum_{\beta} \kappa_{\alpha\beta} \frac{\partial T}{\partial x_\beta}$$

3.2-3

In this study, all materials investigated are cubic and so the thermal conductivity matrix is diagonal. For bulk materials, the x- y- and z-directions are equivalent and so κ_{xx}, κ_{yy} and κ_{zz} should all be equal. The superlattices described in section 4.8 are constructed in a rotated coordinate system where the x- and y-directions are equivalent and the z-direction (along the superlattice axis) is not. Therefore, all materials considered here are such that κ_{xx} and κ_{yy} should be equal. This property is used as a check of the theoretical calculations.

Boltzmann transport theory assumes that for a crystal with a temperature gradient across it, the rate of change of phonon occupation in a small volume of the crystal is caused by two mechanisms; phonon drift and collisions. A number of different collisions can occur, specifically, phonons scattering with the crystal boundaries, defects, impurities and each other. In a steady-state there must be no change in the number of phonons in the small volume of the crystal and so the sum of the drift and collision terms must be zero. The rate of change of the distribution function, $n_j(\vec{q})$ due to the phonon motion is $-\vec{\nabla}_r n_j(\vec{q}) \cdot \vec{v}_j(\vec{q})$ and that due to collisions is $\left[\partial n_j(\vec{q})/\partial t\right]_c$ leading to a steady state condition

$$\left.\frac{\partial n_j(\vec{q})}{\partial t}\right|_c = \vec{v}_j(\vec{q}) \cdot \nabla T \frac{\partial n_j(\vec{q})}{\partial T}$$

3.2-4

6

This equation is the phonon Boltzmann transport equation (BTE). The lattice thermal conductivity tensor can be written as

$$\kappa_{\alpha\beta} = \frac{1}{(2\pi)^3} \sum_j \int d\vec{q} C_j(\vec{q}) v_{j\alpha}(\vec{q}) v_{j\beta}(\vec{q}) \tau_{j\beta}(\vec{q})$$

3.2-5

where $C_j(\vec{q})$ is the mode specific heat given by

$$C_j(\vec{q}) = k_B \left(\frac{\hbar\omega_j(\vec{q})}{k_B T}\right)^2 n_j^0(\vec{q})\left(n_j^0(\vec{q}) + 1\right)$$

3.2-6

and the term $\tau_{j\beta}(\vec{q})$ is a scattering time that encompasses all of the scattering mechanisms present. The term $n_j^0(\vec{q})$ is the Bose distribution function

$$n_j^0(\vec{q}) = \frac{1}{\exp\left[\hbar\omega_j(\vec{q})/k_B T\right] - 1}$$

3.2-7

In an infinite, defect-free, isotopically pure crystal, the left hand side of equation 3.2-4 describes the rate of change of the phonon distribution function due to phonon-phonon collisions and is described as the collision term for the remainder of this dissertation. An explicit evaluation of this term and an exact solution of the phonon BTE demand an accurate description of the microscopic forces and treatment of inelastic scattering. This is an extremely difficult task. Historically, the collision term is dealt with by the introduction of a relaxation time approximation (RTA).[1,2]

Within the RTA, the collision term is replaced by

$$\left.\frac{\partial n_j(\vec{q})}{\partial t}\right|_c = -\frac{n_j(\vec{q}) - n_j^0(\vec{q})}{\tau_j(\vec{q})}$$

3.2-8

leading to a much simpler solution for $n_j(\vec{q})$. The relaxation time $\tau_j(\vec{q})$, for each individual scattering mechanism is approximated (as opposed to the explicit calculation performed in this work, specifically equation 3.10-5) using a temperature and frequency dependent expression, whose form is determined by a set of ad hoc approximations (the theoretical framework for this is dealt with in section 7.1.1). These approximations include using a linear Debye model of the phonon dispersions and the assumptions of low temperature and small phonon frequency. Despite these problems, the

7

use of RTAs makes the calculation of κ_L much more tractable. It is often the case, however, that the RTA is used under conditions unsuited to the underlying approximations[21] (e.g. higher temperatures and anisotropic, non-linear dispersion curves).

In the remainder of chapter 3, an iterative solution to the BTE is developed that accurately treats the collision term and is consequently a significant improvement over the RTA. The calculation of the three-phonon scattering phase space and the scattering strengths required to implement the iterative solution is computationally very expensive and has only become practicable with the advances in processing speeds, which explains in part, the difficulty in progressing beyond the RTA. A major focus of this study is addressing this collision term.

3.3   Interatomic lattice potential

To go beyond the RTA and allow direct calculation of the three-phonon scattering times, the interatomic potential, Φ, that describes the atomic forces in the crystal needs to be examined. This potential can be expressed in a Taylor series

$$\Phi = \Phi_0 + \sum_{l\kappa\alpha} \Phi_\alpha(l\kappa)u_\alpha(l\kappa)$$

$$+ \frac{1}{2}\sum_{l\kappa\alpha}\sum_{l'\kappa'\beta} \Phi_{\alpha\beta}(l\kappa; l'\kappa')u_\alpha(l\kappa)u_\beta(l'\kappa') \qquad \text{3.3-1}$$

$$+ \frac{1}{3!}\sum_{l\kappa\alpha}\sum_{l'\kappa'\beta}\sum_{l''\kappa''\gamma} \Phi_{\alpha\beta\gamma}(l\kappa; l'\kappa'; l''\kappa'')u_\alpha(l\kappa)u_\beta(l'\kappa')u_\gamma(l''\kappa'') + \cdots$$

where l refers to the unit cell and κ locates the atom within the unit cell. α, β and γ are Cartesian coordinates and the u_α describe the atomic deviations from their equilibrium positions. The first term on the right-hand side of equation 3.3-1 is a constant that can be ignored and the second term describes the force exerted on a particular atom by all others. In equilibrium, this force must be equal to zero and so this term can also be ignored. The terms of interest in equation 3.3-1 are those involving $\Phi_{\alpha\beta}$ and $\Phi_{\alpha\beta\gamma}$ and are known as the harmonic and the third-order anharmonic interatomic force constants (IFCs) respectively. These can be written

$$\Phi_{\alpha\beta}\left(l\kappa; l^{'}\kappa^{'}\right) = \left.\frac{\partial^2\Phi}{\partial u_\alpha(l\kappa)\partial u_\beta(l'\kappa')}\right|_{\vec{u}=0} \qquad \textbf{3.3-2}$$

$$\Phi_{\alpha\beta\gamma}\left(l\kappa; l^{'}\kappa^{'}; l''\kappa''\right) = \left.\frac{\partial^3\Phi}{\partial u_\alpha(l\kappa)\partial u_\beta(l'\kappa')\partial u_\gamma(l''\kappa'')}\right|_{\vec{u}=0} \qquad \textbf{3.3-3}$$

The harmonic IFCs are used to describe the phonon frequencies and eigenvectors. In the harmonic approximation, the phonons do not interact with one another. The interaction term is treated as a perturbation to the harmonic approximation and is encapsulated in equation 3.3-3. Calculation of the harmonic IFCs has been studied extensively and extremely good agreement with experimentally measured parameters based on them (for example phonon dispersion curves) is now routine. Calculation of the third-order anharmonic terms is a more complex task and parameters derived from them are only now beginning to yield good comparison with experiment.

3.3.1   Harmonic interatomic force constants

The third term on the right-hand side of equation 3.3-1 is the harmonic part of the interatomic potential, which is used to calculate the phonon eigenvalues and eigenvectors. The equation of motion for the atoms in the harmonic approximation is written as

$$M_\kappa \ddot{u}_\alpha(l\kappa) = -\sum_{l'\kappa'\beta} \Phi_{\alpha\beta}\left(0\kappa; l^{'}\kappa^{'}\right) u_\beta\left(l^{'}\kappa^{'}\right) \qquad \textbf{3.3-4}$$

where M_κ is the mass of the κth atom. A solution to equation 3.3-4 is found by assuming the following form for the atomic displacement

$$u_\alpha(l\kappa) = \frac{1}{\sqrt{M_\kappa}}\sum_{\vec{q}} U_\alpha(\vec{q};\kappa)exp[i(\vec{q}\cdot\vec{x}(l) - \omega t)] \qquad \textbf{3.3-5}$$

where $\vec{x}(\hat{l})$ is the equilibrium position of the lth unit cell. Substitution of equation 3.3-5 into equation 3.3-4 yields

$$\omega^2 U_\alpha(\vec{q};\kappa) = \sum_{\kappa'\beta} D_{\alpha\beta}(\kappa\kappa';\vec{q})U_\beta(\vec{q};\kappa')$$

3.3-6

The non-trivial solution to equation 3.3-6 is found by the determinantal equation

$$\left|D_{\alpha\beta}(\kappa\kappa';\vec{q}) - \omega^2\delta_{\alpha\beta}\delta_{\kappa\kappa'}\right| = 0$$

3.3-7

The form of the dynamical matrix, $D_{\alpha\beta}(\kappa\kappa';\vec{q})$ is given as the Fourier transform of $\Phi_{\alpha\beta}$

$$D_{\alpha\rho}(\kappa\kappa';\vec{q}) = \frac{1}{\sqrt{M_\kappa M_{\kappa'}}}\sum_{l'}\Phi_{\alpha\beta}(0\kappa;l'\kappa')exp[i\vec{q}\cdot\vec{x}(l')]$$

3.3-8

Knowledge of the harmonic IFCs allows the dynamical matrix to be constructed for arbitrary $\vec{q}$ and hence all phonon frequencies and eigenvectors can be calculated.

3.3.2 Third-order anharmonic interatomic force constants

The expression for the third-order anharmonic IFCs is given in equation 3.3-3. Here, it is convenient to express the atomic displacements in terms of raising and lowering operators as follows

$$u_\alpha(l\kappa) = \left(\frac{\hbar}{2NM_\kappa}\right)^{\frac{1}{2}}\sum_{j,\vec{q}}\omega_j^{-\frac{1}{2}}(\vec{q})e_\alpha(\kappa|j\vec{q})e^{i\vec{q}\cdot\vec{R}_l}(a_{j\vec{q}} + a_{-j\vec{q}}^+)$$

3.3-9

where N is the number of unit cells and $e_\alpha(\kappa|j\vec{q})$ is the αth component of a phonon eigenvector. By inserting equation 3.3-9 into the fourth term in equation 3.3-1, the following form for the third-order part of the potential is obtained

$$\Phi_3 = \frac{1}{3!}\sum_{l\kappa}\sum_{l'\kappa'}\sum_{l''\kappa''}\sum_{\alpha\beta\gamma}\Phi_{\alpha\beta\gamma}\left(\frac{\hbar}{2N}\right)^{\frac{3}{2}}\frac{1}{\sqrt{M_\kappa M_{\kappa'} M_{\kappa''}}}\sum_{\lambda_1\lambda_2\lambda_3}\frac{e_{\alpha\kappa}^{\lambda_1}e_{\beta\kappa'}^{\lambda_2}e_{\gamma\kappa''}^{\lambda_3}}{\sqrt{\omega_{\lambda_1}\omega_{\lambda_2}\omega_{\lambda_3}}}e^{i\vec{q}_1\cdot\vec{R}_l}e^{i\vec{q}_2\cdot\vec{R}_{l'}}e^{i\vec{q}_3\cdot\vec{R}_{l''}}$$

3.3-10

$$\times\left(a_{\lambda_1} + a_{-\lambda_1}^+\right)\left(a_{\lambda_2} + a_{-\lambda_2}^+\right)\left(a_{\lambda_3} + a_{-\lambda_3}^+\right)$$

In the above, λ has been used to designate the branch index, j and the wavevector $\vec{q}$, $\lambda \equiv (j,\vec{q})$. Similarly, $-\lambda$ designates j and $-\vec{q}$. Adding a lattice vector, $\vec{R}$ to any or all of $\vec{R}_l$, $\vec{R}_{l'}$ or $\vec{R}_{l''}$ should leave

Φ_3 unchanged due to the translational invariance of the interatomic potential. Therefore, adding $\vec{R}$ to all the exponential exponents leads to the following condition,

$$e^{i(\vec{q}_1 + \vec{q}_2 + \vec{q}_3) \cdot \vec{R}} = 1 \tag{3.3-11}$$

$$\vec{q}_1 + \vec{q}_2 + \vec{q}_3 = \vec{K}$$

where $\vec{K}$ is a reciprocal lattice vector. The sum over l in equation 3.3-10 can be eliminated by using the fact that the third-order IFCs do not depend on the absolute position of the ions, only the relative positions. Thus

$$\Phi_{\alpha\beta\gamma}\left(l\kappa; l'\kappa'; l''\kappa''\right) = \Phi_{\alpha\beta\gamma}\left(0\kappa; l'-l\,\kappa'; l''-l\,\kappa''\right) \tag{3.3-12}$$

Then, by redefining $l' \to l' - l$ and $l'' \to l'' - l$, the expression for Φ_3 can be rewritten as

$$\Phi_3 = \frac{1}{6}\left(\frac{\hbar}{2N}\right)^{\frac{3}{2}} N \sum_{\kappa} \sum_{l'\kappa'} \sum_{l''\kappa''} \sum_{\alpha\beta\gamma} \Phi_{\alpha\beta\gamma} \frac{1}{\sqrt{M_\kappa M_{\kappa'} M_{\kappa''}}} \sum_{\lambda_1\lambda_2\lambda_3} \frac{e^{\lambda_1}_{\alpha\kappa} e^{\lambda_2}_{\beta\kappa'} e^{\lambda_3}_{\gamma\kappa''}}{\sqrt{\omega_{\lambda_1}\omega_{\lambda_2}\omega_{\lambda_3}}} e^{i\vec{q}_2 \cdot \vec{R}_{l'}} e^{i\vec{q}_3 \cdot \vec{R}_{l''}} \tag{3.3-13}$$

$$\times \left(a_{\lambda_1} + a^+_{-\lambda_1}\right)\left(a_{\lambda_2} + a^+_{-\lambda_2}\right)\left(a_{\lambda_3} + a^+_{-\lambda_3}\right)$$

The extra factor of N comes from the above redefinition of $\{l\}$ and the resulting evaluation of the sum over l. By expanding the parentheses involving the raising and lowering operators, it is clear that this expression describes processes in which each of the three phonons is either created or destroyed. Energy must be conserved in all these scattering processes and so those terms in equation 3.3-13 that correspond to all three phonons being created or all three phonons being destroyed are not energetically possible and can be disregarded. The three-phonon scattering processes that satisfy the necessary conservation conditions are considered in the following section.

3.4 Three-phonon scattering processes

There are four different three-phonon scattering processes to consider in evaluating the collision term in equation 3.2-4. If the three phonons involved in the collision are in branches j, j' and j'' and

have wavevectors $\vec{q}$, $\vec{q}'$ and $\vec{q}''$ respectively, then these four mechanisms can be described as shown in Table 3-1.
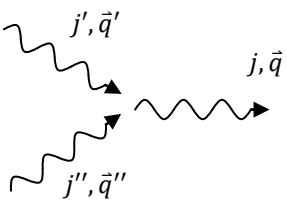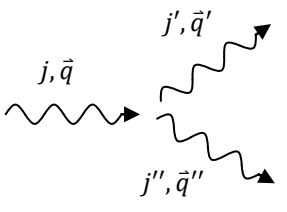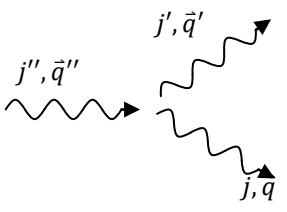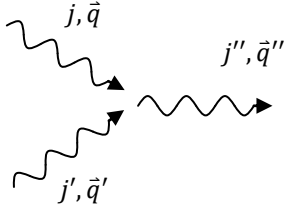
	Phonon mode, $n_j(\vec{q})$	Phonon mode, $n_{j'}(\vec{q}')$	Phonon mode, $n_{j''}(\vec{q}'')$	
Mechanism 1	Increase by 1	Decrease by 1	Decrease by 1	
Mechanism 2	Decrease by 1	Increase by 1	Increase by 1	
Mechanism 3	Increase by 1	Increase by 1	Decrease by 1	
Mechanism 4	Decrease by 1	Decrease by 1	Increase by 1	

Table 3-1; Three-phonon scattering processes that obey the conservation of energy.

The scattering rates are calculated using Fermi's golden rule

$$W = \frac{2\pi}{\hbar}|\langle f|\Phi_3|i\rangle|^2\delta\left(E_f - E_i\right)$$

3.4-1

12

where i and f refer to the initial and final states respectively. The δ-function ensures that energy is conserved and Φ_3 is the third-order part of the interatomic potential. For the scattering process described in Table 3-1 as "mechanism 1", the matrix element in equation 3.4-1 can be evaluated as follows

$$\langle f|\Phi_3|i\rangle_1 = \frac{1}{6}\left(\frac{\hbar}{2N}\right)^{\frac{3}{2}} N \left|\begin{matrix} n_\lambda + 1 \\ n_{\lambda'} - 1 \\ n_{\lambda''} - 1 \end{matrix}\right| \sum_{\lambda_1\lambda_2\lambda_3} \left(a_{\lambda_1} + a^+_{-\lambda_1}\right)\left(a_{\lambda_2} + a^+_{-\lambda_2}\right)\left(a_3 + a^+_{-\lambda_3}\right) \frac{\Phi_{\lambda_1\lambda_2\lambda_3}}{\sqrt{\omega_{\lambda_1}\omega_{\lambda_2}\omega_{\lambda_3}}} \left|\begin{matrix} n_\lambda \\ n_{\lambda'} \\ n_{\lambda''} \end{matrix}\right| \qquad \textbf{3.4-2}$$

For brevity, $\Phi_{\lambda_1\lambda_2\lambda_3}$ has been defined as

$$\Phi_{\lambda_1\lambda_2\lambda_3} = \sum_\kappa \sum_{l'\kappa'} \sum_{l''\kappa''} \sum_{\alpha\beta\gamma} \Phi_{\alpha\beta\gamma}\, e^{i\vec{q}_2\cdot\vec{R}_{l'}}\, e^{i\vec{q}_3\cdot\vec{R}_{l''}} \frac{e^{\lambda_1}_{\alpha\kappa} e^{\lambda_2}_{\beta\kappa'} e^{\lambda_3}_{\gamma\kappa''}}{\sqrt{M_\kappa M_{\kappa'} M_{\kappa''}}} \qquad \textbf{3.4-3}$$

In expanding out the parentheses in equation 3.4-2, only terms with one raising and two lowering operators need to be retained as these are the only terms that yield a non-vanishing matrix element. This expansion gives rise to three terms. Table 3-2 shows which phonons must correspond to the terms in the raising and lowering operators for the correct final state to result.

	λ_1	λ_2	λ_3
$a_{\lambda_1} a_{\lambda_2} a^+_{-\lambda_3}$	λ'	λ''	$-\lambda$
	λ''	λ'	$-\lambda$
$a_{\lambda_1} a^+_{-\lambda_2} a_{\lambda_3}$	λ'	$-\lambda$	λ''
	λ''	$-\lambda$	λ'
$a^+_{-\lambda_1} a_{\lambda_2} a_{\lambda_3}$	$-\lambda$	λ'	λ''
	$-\lambda$	λ''	λ'

Table 3-2; The determination of the different possible permutations of λ, λ' and λ'' that give rise to the scattering process described as mechanism 1 in Table 3-1.

Using the different permutations outlined in Table 3-2, the sum in equation 3.4-2 can be evaluated and the matrix element for the first scattering mechanism (from Table 3-1) can be written

13

$$\langle f|\Phi_3|i\rangle_1 = \frac{1}{6}\left(\frac{\hbar}{2N}\right)^{\frac{3}{2}} N \frac{(n_\lambda + 1)^{\frac{1}{2}}n_{\lambda'}^{\frac{1}{2}}n_{\lambda''}^{\frac{1}{2}}}{\sqrt{\omega_{\lambda_1}\omega_{\lambda_2}\omega_{\lambda_3}}} \qquad \textbf{3.4-4}$$

$$\times \left(\Phi_{\lambda'\lambda''-\lambda} + \Phi_{\lambda''\lambda'-\lambda} + \Phi_{\lambda'-\lambda\lambda''} + \Phi_{\lambda''-\lambda\lambda'} + \Phi_{-\lambda\lambda'\lambda''} + \Phi_{-\lambda\lambda''\lambda'}\right)$$

The third-order anharmonic IFCs obey a set of symmetry operations,[22] one of which states that any pair of indices (λ, λ' or λ'') can be interchanged leaving the IFCs unchanged. Exploiting this property, it is clear that all the Φ terms in equation 3.4-4 are equal and so

$$\langle f|\Phi_3|i\rangle_1 = \left(\frac{\hbar}{2N}\right)^{\frac{3}{2}} N \frac{(n_\lambda + 1)^{\frac{1}{2}}n_{\lambda'}^{\frac{1}{2}}n_{\lambda''}^{\frac{1}{2}}}{\sqrt{\omega_\lambda\omega_{\lambda'}\omega_{\lambda''}}}\Phi_{-\lambda\lambda'\lambda''} \qquad \textbf{3.4-5}$$

This means that the scattering rate for the first scattering mechanism can be written

$$W_1 = \frac{\pi\hbar^5}{4N}\frac{(n_\lambda + 1)n_{\lambda'}n_{\lambda''}}{E_\lambda E_{\lambda'} E_{\lambda''}}|\Phi_{-\lambda\lambda'\lambda''}|^2\delta(E_\lambda - E_{\lambda'} - E_{\lambda''}) \qquad \textbf{3.4-6}$$

where the phonon frequencies have been written as energies, $E_\lambda = \hbar\omega_\lambda$. There are then three other terms for the remaining scattering mechanisms shown in Table 3-1 which, when combined, lead to a rate of change of phonon occupation number due to three-phonon scattering processes as

$$\left[\frac{\partial n_\lambda}{\partial t}\right]_c = \sum_{\lambda'\lambda''}(W_1 + W_2 + W_3 + W_4)$$

$$= \frac{\pi\hbar^5}{4N}\sum_{\lambda'\lambda''}\left[\left(\frac{(n_\lambda + 1)n_{\lambda'}n_{\lambda''}}{E_\lambda E_{\lambda'} E_{\lambda''}} - \frac{n_\lambda(n_{\lambda'} + 1)(n_{\lambda''} + 1)}{E_\lambda E_{\lambda'} E_{\lambda''}}\right)|\Phi_{-\lambda\lambda'\lambda''}|^2\delta(E_\lambda - E_{\lambda'} - E_{\lambda''})\right. \qquad \textbf{3.4-7}$$

$$\left.+ \left(\frac{(n_\lambda + 1)(n_{\lambda'} + 1)n_{\lambda''}}{E_\lambda E_{\lambda'} E_{\lambda''}} - \frac{n_\lambda n_{\lambda'}(n_{\lambda''} + 1)}{E_\lambda E_{\lambda'} E_{\lambda''}}\right)|\Phi_{\lambda\lambda'-\lambda''}|^2\delta(E_\lambda + E_{\lambda'} - E_{\lambda''})\right]$$

To ensure that no identical processes are double counted, each term in equation 3.4-7 is considered. The first term corresponds to two phonons being destroyed and one created. The dispersion curves shown in Figure 3-2 demonstrate how a scattering process could be double counted.
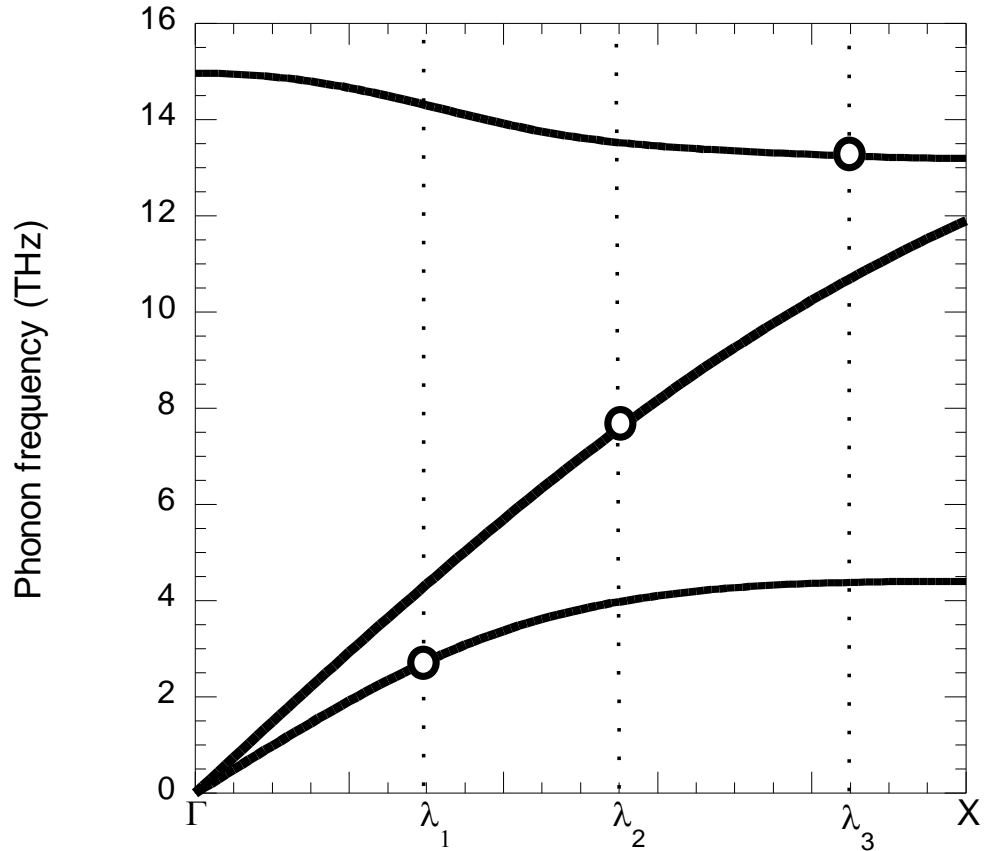
Figure 3-2; Example of a three-phonon scattering process involved in a scattering rate calculation.

If $\lambda = \lambda_3$, is fixed, then when the sum over λ' and λ'' is performed, two terms will be found; the first corresponding to $\lambda' = \lambda_1$, $\lambda'' = \lambda_2$ and the second corresponding to $\lambda' = \lambda_2$, $\lambda'' = \lambda_1$. Both of these terms describe phonons at λ_1 and λ_2 being destroyed and a phonon at λ_3 being created. As the phonons (bosons) are indistinguishable, these two scattering processes are identical and should only be counted once. A factor of one half needs to be included in front of the first term in equation 3.4-7 to account for this. The second term on the right hand side of 3.4-7, on the other hand does not suffer from this problem. This is because with $\lambda = \lambda_1$ fixed, the only event that can be found that satisfies energy conservation for the creation of λ_1 and λ_2 and the destruction of λ_3 is if $\lambda' = \lambda_2$ and $\lambda'' = \lambda_3$. In general, if interchanging λ' and λ'' results in an indistinguishable scattering process, a factor of 1/2 is required. The final expression for the scattering rate can now be written

15

$$\left[\frac{\partial n_\lambda}{\partial t}\right]_c = \frac{\pi\hbar^5}{4N}\sum_{\lambda'\lambda''}\left[\frac{1}{2}\left(\frac{(n_\lambda+1)n_{\lambda'}n_{\lambda''}}{E_\lambda E_{\lambda'}E_{\lambda''}} - \frac{n_\lambda(n_{\lambda'}+1)(n_{\lambda''}+1)}{E_\lambda E_{\lambda'}E_{\lambda''}}\right)|\Phi_{-\lambda\lambda'\lambda''}|^2\delta(E_\lambda - E_{\lambda'} - E_{\lambda''})\right.$$

$$\left. + \left(\frac{(n_\lambda+1)(n_{\lambda'}+1)n_{\lambda''}}{E_\lambda E_{\lambda'}E_{\lambda''}} - \frac{n_\lambda n_{\lambda'}(n_{\lambda''}+1)}{E_\lambda E_{\lambda'}E_{\lambda''}}\right)|\Phi_{\lambda\lambda'-\lambda''}|^2\delta(E_\lambda + E_{\lambda'} - E_{\lambda''})\right]$$

3.4-8

Incorporating this expression into the BTE and recasting it into a form that can be solved iteratively is the subject of sections 3.6 and 3.7. Prior to formulating the equations in a soluble form, the effect of four-phonon processes and the reasons behind their exclusion from this study is discussed.

3.5   Four phonon scattering processes

Four-phonon scattering processes enter into the crystal Hamiltonian in two different ways. Firstly, they enter through first-order perturbation theory using the quartic anharmonicity. Secondly, they enter through second-order perturbation theory using the cubic anharmonicity. The total transition probability can be found in a similar manner to the three-phonon probability using Fermi's golden rule

$$W = \frac{2\pi}{\hbar}\left(|\langle f|\Phi_4|i\rangle|^2 + \sum_{m\neq i,f}\left|\frac{\langle f|\Phi_3|m\rangle\langle m|\Phi_3|i\rangle}{E_i - E_m}\right|^2\right)\delta(E_f - E_i)$$

3.5-1

where E_m is the energy of an intermediate virtual phonon state $|m\rangle$. Using a simplified procedure, Ecsedy and Klemens[23] obtained a high-temperature (four-phonon scattering processes are only of importance at high temperatures) single-mode relaxation time for four-phonon scattering processes that is proportional to T^2. The single-mode relaxation times associated with three-phonon scattering processes are proportional to T (see section 7.5 for ab initio calculations of these relaxation times). At high temperature the temperature dependence of the specific heat saturates to a constant value and so the phonon scattering time, $\tau_j(\vec{q})$, determines the temperature dependence of κ_L. It is therefore expected that if κ_L is dominated by three-phonon scattering, the temperature dependence will show a T^{-1} form. The temperature dependence of four-phonon scattering would enter as a term that varies as T^{-2} and so the relative importance of four-phonon scattering can be estimated by the

measured temperature dependence. For the materials and temperatures considered in this study, the measured thermal conductivities show very close agreement to a T^{-1} variation and so the four-phonon processes can be confidently omitted. Ecsedy and Klemens[23] estimate that the strengths of four-phonon scattering processes are *at least* two to three orders of magnitude weaker than three-phonon scattering processes; a fact that further justifies the omission of four-phonon scattering processes.

3.6   Linearized Boltzmann transport equation

The phonon distribution function in the presence of a small temperature gradient can be written as $n_\lambda = n_\lambda^0 + n_\lambda^1$, where n_λ^0 is the equilibrium Bose distribution. When the system is in equilibrium, the rate of change of n_λ is zero. Using equation 3.4-8, this leads to the following conditions

$$(n_\lambda^0 + 1)n_{\lambda'}^0 n_{\lambda''}^0 = n_\lambda^0(n_{\lambda'}^0 + 1)(n_{\lambda''}^0 + 1)$$

$$(n_\lambda^0 + 1)(n_{\lambda'}^0 + 1)n_{\lambda''}^0 = n_\lambda^0 n_{\lambda'}^0 (n_{\lambda''}^0 + 1)$$

$\hspace{12cm}$ **3.6-1**

The deviation from equilibrium n_λ^1 can be described in terms of a non-equilibrium parameter, ψ_λ such that $n_\lambda^1 = (\partial n_\lambda^0/\partial T)\psi_\lambda$ is assumed to be linear in the temperature gradient. As n_λ^0 is a Bose distribution function, it can easily be differentiated and so

$$n_\lambda^1 = n_\lambda^0(n_\lambda^0 + 1)\beta\Psi_\lambda \hspace{6cm} \textbf{3.6-2}$$

where $\beta = 1/k_B T$. Replacing the terms involving the distribution functions in equation 3.4-8 with the equilibrium and perturbed parts, applying the conditions in 3.6-1 and ignoring terms of second order and above in the perturbations, then replacing all the perturbed parts, n_λ^1 by 3.6-2 yields

$$(n_\lambda + 1)n_{\lambda'}n_{\lambda''} - n_\lambda(n_{\lambda'} + 1)(n_{\lambda''} + 1) \approx n_\lambda^0(n_{\lambda'}^0 + 1)(n_{\lambda''}^0 + 1)\beta(\Psi'' + \Psi' - \Psi)$$

$$(n_\lambda + 1)(n_{\lambda'} + 1)n_{\lambda''} - n_\lambda n_{\lambda'}(n_{\lambda''} + 1) \approx n_\lambda^0 n_{\lambda'}^0 (n_{\lambda''}^0 + 1)\beta(\Psi'' - \Psi' - \Psi)$$

$\hspace{12cm}$ **3.6-3**

Substituting these expressions into equation 3.4-8 gives the final expression for the scattering rate as

$$\left[\frac{\partial n_\lambda}{\partial t}\right]_c = \beta \sum_{\lambda'\lambda''} \left(W^+_{\lambda\lambda'\lambda''} [\Psi_{\lambda''} - \Psi_{\lambda'} - \Psi_\lambda] + \frac{1}{2} W^-_{\lambda\lambda'\lambda''} [\Psi_{\lambda''} + \Psi_{\lambda'} - \Psi_\lambda] \right)$$

<div align="right">3.6-4</div>

where

$$W^\pm_{\lambda\lambda'\lambda''} = \frac{\pi\hbar^5}{4N} \frac{n^0_\lambda \left(n^0_{\lambda'} + \frac{1}{2} \mp \frac{1}{2}\right)\left(n^0_{\lambda''} + 1\right)}{E_\lambda E_{\lambda'} E_{\lambda''}} |\Phi_{-\lambda\lambda'\lambda''}|^2 \delta(E_\lambda \pm E_{\lambda'} - E_{\lambda''})$$

<div align="right">3.6-5</div>

Finally, combining equations 3.6-4 and 3.2-4 leads to the linearized phonon BTE

$$k_B T \vec{v}_\lambda \cdot \vec{\nabla}_r T \frac{\partial n^0_\lambda}{\partial T} = \sum_{\lambda'\lambda''} \left(W^+_{\lambda\lambda'\lambda''} [\Psi_{\lambda''} - \Psi_{\lambda'} - \Psi_\lambda] + \frac{1}{2} W^-_{\lambda\lambda'\lambda''} [\Psi_{\lambda''} + \Psi_{\lambda'} - \Psi_\lambda] \right)$$

<div align="right">3.6-6</div>

The goal is to solve equation 3.6-6 for the non-equilibrium functions, Ψ_λ and from these calculate the thermal conductivity. The manner in which this is achieved is discussed in the rest of this chapter. The first step in achieving this goal is to cast equation 3.6-6 in a form that can be solved iteratively.

3.7 Iterative solution[6]

In this study, the linearized BTE is solved using an iterative technique. The first step in recasting 3.6-6 in a form that can be solved iteratively is to define the non-equilibrium parameter, Ψ_λ in terms of a function F_λ

$$\Psi_\lambda = -\sum_\alpha F_{\lambda\alpha} \frac{\partial T}{\partial x_\alpha}$$

<div align="right">3.7-1</div>

Inserting 3.7-1 into 3.6-6 and extracting the term $F_{\lambda\alpha}$ from the summation over λ' and λ'', the following equation for the αth component results.

$$Q_\lambda F_{\lambda\alpha} = k_B T v_{\lambda\alpha} \frac{\partial n^0_\lambda}{\partial T} + \sum_{\lambda'\lambda''} \left[W^+_{\lambda\lambda'\lambda''} (F_{\lambda''\alpha} - F_{\lambda'\alpha}) + \frac{1}{2} W^-_{\lambda\lambda'\lambda''} (F_{\lambda''\alpha} + F_{\lambda'\alpha}) \right]$$

<div align="right">3.7-2</div>

where the function Q_λ has been defined as

$$Q_\lambda = \sum_{\lambda'\lambda''} \left(W^+_{\lambda\lambda'\lambda''} + \frac{1}{2} W^-_{\lambda\lambda'\lambda''} \right)$$

<div align="right">3.7-3</div>

Evaluating the differential of the equilibrium phonon distribution, $\partial n_\lambda^0 / \partial T$ in 3.7-2 and rearranging leads to the iterative form of the linearized BTE.

$$F_{\lambda\alpha} = F_{\lambda\alpha}^0 + \frac{1}{Q_\lambda} \sum_{\lambda'\lambda''} \left[W_{\lambda\lambda'\lambda''}^+ (F_{\lambda''\alpha} - F_{\lambda'\alpha}) + \frac{1}{2} W_{\lambda\lambda'\lambda''}^- (F_{\lambda''\alpha} + F_{\lambda'\alpha}) \right]$$

3.7-4

where the zeroth-order solution is given by

$$F_{\lambda\alpha}^0 = \frac{\hbar\omega_\lambda n_\lambda^0 (n_\lambda^0 + 1) v_{\lambda\alpha}}{TQ_\lambda}$$

3.7-5

The previous analysis is restricted to the inelastic phonon-phonon scattering that is intrinsic to thermal transport. Naturally occurring materials are not isotopically pure and defect-free, but generally contain significant concentrations of isotopic impurities. In order to compare calculated results with experimental measurements, some account of isotopic impurity scattering must be made. The manner in which equation 3.7-4 is modified to include these extrinsic processes is discussed in the following section.

3.8 Isotopic impurity scattering

Physical samples used for experimental measurements are not the infinite, isotopically pure, defect free crystals assumed by the BTE formalism, which assumes that only three-phonon scattering is present. While many isotopically enriched sample materials have now been artificially produced and measured,[20,24] there still exists a small concentration of isotopic impurities. The presence of these impurities modifies κ_L through the differences in the isotopic masses.

The effects of elastic scattering between phonons and isotopic impurities can be introduced into the formalism of the phonon BTE relatively easily. Using the same arguments as used for the three-phonon scattering, the probability of a phonon λ scattering with an isotopic impurity into a phonon λ' is given by Fermi's golden rule

$$W_{\lambda\lambda'}^{imp} = \frac{2\pi}{\hbar} \left\langle \begin{matrix} n_\lambda - 1 \\ n_{\lambda'} + 1 \end{matrix} \right| H^{imp} \left| \begin{matrix} n_\lambda \\ n_{\lambda'} \end{matrix} \right\rangle \delta(E_f - E_i)$$

3.8-1

where H^{imp} is the perturbation to the harmonic Hamiltonian using the average mass of the isotopic impurities in the crystal. The δ-function ensures that energy is conserved in the scattering process. If the average mass is defined as

$$M_{av} \equiv \sum_{l\kappa} M_\kappa f_\kappa = \frac{1}{N} \sum_{l\kappa} M_\kappa \tag{3.8-2}$$

where f_κ is the fraction of atoms with mass M_κ, then the unperturbed and perturbed parts of the Hamiltonian can be written

$$H = \frac{1}{2} M_{av} \sum_{l\kappa} \left(\frac{\partial \vec{u}(l\kappa)}{\partial t} \right)^2 + \frac{1}{2} \sum_{l\kappa} \Delta M_\kappa \left(\frac{\partial \vec{u}(l\kappa)}{\partial t} \right)^2 \tag{3.8-3}$$

The perturbed part (second term) can be constructed using relation 3.3-9. Carrying through the algebra and inserting back into equation 3.8-1, the scattering rate for phonon-impurity scattering processes is

$$W_{\lambda\lambda'}^{imp} = \frac{\pi}{2} g_2 \omega_\lambda \omega_{\lambda'} n_\lambda^0 (n_{\lambda'}^0 + 1) \sum_\kappa |\hat{e}_{\kappa\lambda}^* \cdot \hat{e}_{\kappa\lambda'}|^2 \delta(\omega_{\lambda'} - \omega_\lambda) \tag{3.8-4}$$

where g_2 is the mass-variance parameter[3,25,26] defined by

$$g_2 = \sum_{l\kappa} f_\kappa \left(1 - \frac{M_\kappa}{M_{av}} \right)^2 \tag{3.8-5}$$

The scattering rate for phonon-impurity processes can be added in a straight-forward manner to the linearized BTE

$$k_B T \vec{v}_\lambda \cdot \vec{V}_r T \frac{\partial n_\lambda^0}{\partial T} = \sum_{\lambda' \lambda''} \left(W_{\lambda\lambda'\lambda''}^+ [\Psi_{\lambda''} - \Psi_{\lambda'} - \Psi_\lambda] + \frac{1}{2} W_{\lambda\lambda'\lambda''}^- [\Psi_{\lambda''} + \Psi_{\lambda'} - \Psi_\lambda] \right)$$
$$+ \sum_{\lambda'} W_{\lambda\lambda'}^{imp} [\Psi_{\lambda'} - \Psi_\lambda] \tag{3.8-6}$$

Consequently, the iteration procedure including the new scattering channel is modified to

$$F_{\lambda\alpha} = F_{\lambda\alpha}^0 + \frac{1}{Q_\lambda} \left\{ \sum_{\lambda' \lambda''} \left[W_{\lambda\lambda'\lambda''}^+ (F_{\lambda''\alpha} - F_{\lambda'\alpha}) + \frac{1}{2} W_{\lambda\lambda'\lambda''}^- (F_{\lambda''\alpha} + F_{\lambda'\alpha}) \right] + \sum_{\lambda'} W_{\lambda\lambda'}^{imp} F_{\lambda'\alpha} \right\} \tag{3.8-7}$$

20

and the term Q_λ described in equation 3.7-3 is also modified to contain a contribution from the isotopic impurity scattering

$$Q_\lambda = \sum_{\lambda'\lambda''} \left(W^+_{\lambda\lambda'\lambda''} + \frac{1}{2} W^-_{\lambda\lambda'\lambda''} \right) + \sum_{\lambda'} W^{imp}_{\lambda\lambda'} \qquad \text{3.8-8}$$

The mass variance parameter is the only parameter introduced in this study that *cannot* be derived from first-principles. It is found experimentally by determining the exact isotopic composition of a *particular* sample. With this term included, it is possible to perform direct comparisons with measurements of materials with known isotopic compositions. In principle, it would be possible to use g_2 as an adjustable parameter to fit the thermal conductivity of a sample of unknown isotopic composition. In this way, the concentration of different isotopes could be estimated.

Isotopic impurities are not the only crystal impurities from which phonons can scatter. For instance, naturally occurring diamond has a rich array of substitutional impurities, the most abundant of which is nitrogen. It is usually the case, however, that isotopic impurities have the highest concentrations and are responsible for the vast majority of impurity scattering. Extreme cases of type Ia diamonds[27] have nitrogen concentrations of approximately a quarter of a percent. In this study the calculations are compared with measurements of type IIa diamonds which have significantly lower nitrogen concentrations. As a result, the substitutional impurities are not considered in this study.

3.9   Boundary scattering

Scattering from sample boundaries can be included in the BTE formalism through a relaxation time, τ_{bs}. If the effective phonon mean free path[3,28] is L_{eff}, which in the regime of boundary scattering is of the order of the sample size, then the boundary scattering relaxation time can be defined as

$$\tau_{bs} = \frac{L_{eff}}{v_{ave}}$$

where v_{ave} is the average velocity of the acoustic phonons

$$v_{ave} = \left[\frac{1}{3}\left(\frac{2}{v_T} + \frac{1}{v_L}\right)\right]^{-1}$$

The introduction of the boundary scattering does not alter the iteration procedure, but modifies the function, Q_λ to

$$Q_\lambda = \sum_{\lambda'\lambda''} \left(W^{+}_{\lambda\lambda'\lambda''} + \frac{1}{2}W^{-}_{\lambda\lambda'\lambda''}\right) + \sum_{\lambda'} W^{imp}_{\lambda\lambda'} + \frac{n^0_\lambda(n^0_\lambda + 1)}{\tau_{bs}}$$

This boundary scattering term is only used in the calculations of κ_L using empirical interatomic potentials described in section 4.7.

3.10 Lattice thermal conductivity

The linearized BTE is solved for $F_{\lambda\alpha}$ by methods discussed in the next section. The goal of the process is the calculation of κ_L and so the non-linear distribution function needs to be linked to the calculated $F_{\lambda\alpha}$. In combining equations 3.2-2 and 3.2-3, the phonon distribution function $n_j(\vec{q})$ is replaced by the sum of the equilibrium and perturbed parts, $n^0_j(\vec{q}) + n^1_j(\vec{q})$ and then the deviation term is expressed as follows

$$n^1_j(\vec{q}) = -\sum_\beta \frac{\partial n^0_j(\vec{q})}{\partial T} F_{j\beta}(\vec{q}) \frac{\partial T}{\partial x_\beta}$$

using equation 3.7-1. This leads to the following

$$\frac{1}{V}\sum_{j,\vec{q}} \hbar\omega_j(\vec{q})v_{j\alpha}(\vec{q})\left[n^0_j(\vec{q}) - \sum_\beta \frac{\partial n^0_j(\vec{q})}{\partial T} F_{j\beta}(\vec{q})\frac{\partial T}{\partial x_\beta}\right] = -\sum_\beta \kappa_{\alpha\beta}\frac{\partial T}{\partial x_\beta}$$

In performing the sum over $\vec{q}$, the first term on the left hand side will disappear. This is a result of the symmetry of the velocity (see section 3.11.2). For phonon $-\vec{q}$, the frequency will be identical, but the velocity will be the negative of that of phonon $\vec{q}$. Thus each term $\vec{q}$ will be identically cancelled by

the corresponding term in $-\vec{q}$. Physically, this is equivalent to there being no heat flow in the absence of a temperature gradient.

Equating components and cancelling the temperature gradient leaves

$$\kappa_{\alpha\beta} = \frac{1}{V} \sum_{j,\vec{q}} \frac{\hbar^2}{k_B T} \omega_j(\vec{q}) v_{j\alpha}(\vec{q}) F_{j\beta}(\vec{q}) n_j^0(\vec{q}) [n_j^0(\vec{q}) + 1] \qquad \text{3.10-3}$$

after evaluating the differential $\partial n_\lambda^0 / \partial T$. Treating $\vec{q}$ as a continuous variable for integration and gathering together the terms for the mode specific heat defined in 3.2-6, the following results

$$\kappa_{\alpha\beta} = \frac{1}{(2\pi)^3} \sum_j \int d\vec{q} \, \frac{C_j(\vec{q}) T v_{j\alpha}(\vec{q}) F_{j\beta}(\vec{q})}{\omega_j(\vec{q})} \qquad \text{3.10-4}$$

Equating 3.10-4 with 3.2-5, the scattering time, $\tau_{j\beta}(\vec{q})$ is recovered

$$\tau_{j\beta}(\vec{q}) = \frac{T F_{j\beta}(\vec{q})}{\omega_j(\vec{q}) v_{j\beta}(\vec{q})} \qquad \text{3.10-5}$$

Therefore, calculation of the function $F_{j\beta}(\vec{q})$ leads to a calculation of the scattering time, $\tau_j(\vec{q})$ (this can be identified with the relaxation time, a point that is exploited in chapter 7 to derive new forms for $\tau_j(\vec{q})$ for use in RTAs) and finally the lattice thermal conductivity, κ_L. The numerical techniques used for performing these calculations are outlined in the following section.

3.11 Solving the iterative equation

The first step in evaluating equation 3.7-4 (or 3.8-7 in the case of isotopic impurities) is performing the sums over λ' and λ''. These can be expanded as sums over the phonon branches, j, and wavevectors, $\vec{q}$. Enforcing the conservation of crystal momentum (3.3-11), the function $Q_\lambda \equiv Q_j(\vec{q})$ can be written

$$Q_j(\vec{q}) = \sum_{j'j''} \sum_{\vec{q}'\vec{q}''} \left(W_{\lambda\lambda'\lambda''}^+ \delta_{\vec{q}+\vec{q}'-\vec{q}''} + \frac{1}{2} W_{\lambda\lambda'\lambda''}^- \delta_{\vec{q}-\vec{q}'-\vec{q}''} \right)$$

$$\text{3.11-1}$$

$$= \frac{\pi\hbar^5 V}{4N(2\pi)^3} \sum_{j'j''} \int d\vec{q}' \left(\widetilde{W}_{\lambda\lambda'\lambda''}^+ + \frac{1}{2} \widetilde{W}_{\lambda\lambda'\lambda''}^- \right) \delta(E_\lambda \pm E_{\lambda'} - E_{\lambda''})$$

where $\vec{q}'$ is treated as a continuous variable and so the sum is replaced by an integral and

23

$$W^{\pm}_{\lambda\lambda'\lambda''} = \frac{\pi\hbar^5}{4N}\widetilde{W}^{\pm}_{\lambda\lambda'\lambda''}\delta(E_\lambda \pm E_{\lambda'} - E_{\lambda''})$$

<div align="right">3.11-2</div>

The conservation of momentum is used to eliminate the sum over $\vec{q}''$. The conservation of energy condition can be used to turn the three-dimensional integral into a two-dimensional one. The crystal volume and number of unit cells can be eliminated by noticing that $V/N = \Omega$, the unit cell volume.

The procedure for calculating the phase space for three phonon scattering is depicted as a flowchart in Figure 3-3 and explained below. This procedure determines the three-phonon scattering processes that satisfy both the conservation of energy and crystal momentum for a particular selection of $\vec{q}, q'_x$ and q'_y and is repeated for all possible values.
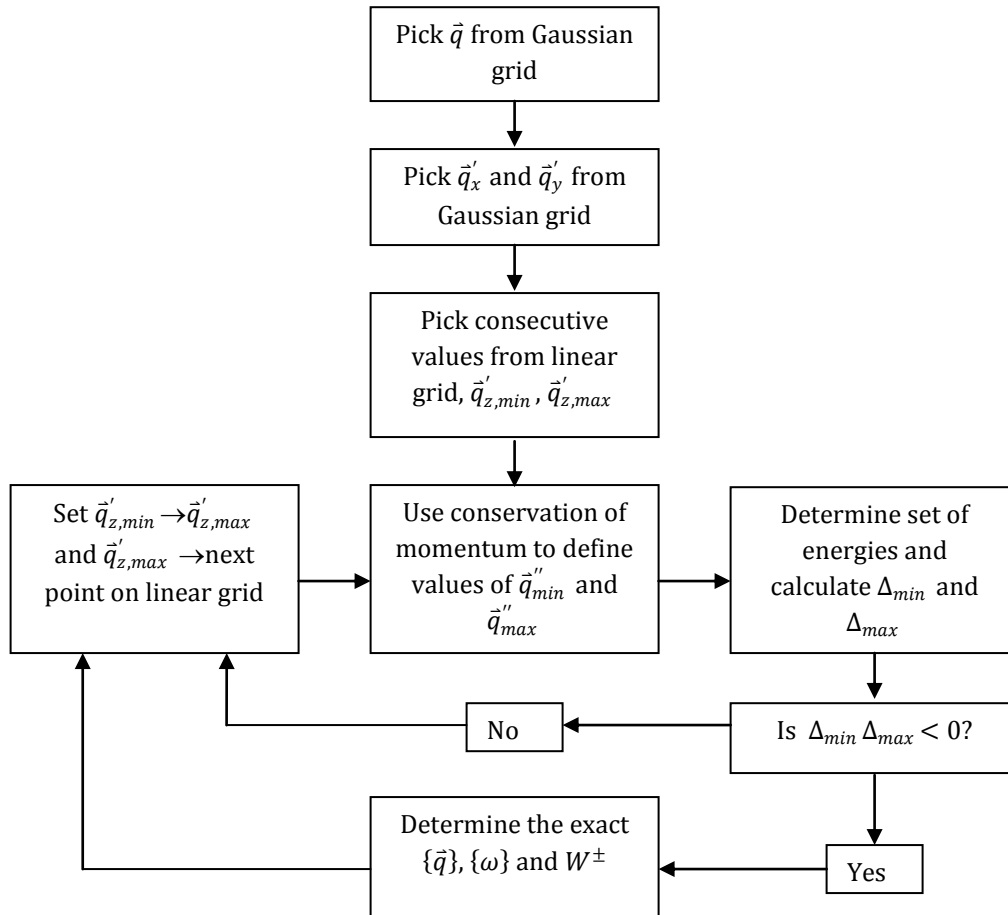

Figure 3-3; Flowchart demonstrating the phase space search process. The above process is performed for all phonon components $\vec{q}, \vec{q}'_x$ and $\vec{q}'_y$.

The integral over $\vec{q}'$ is first split into the three Cartesian components. A Gaussian quadrature is set up over the first Brillouin zone in the three directions and the three components of $\vec{q}$ are picked from the grid. The x- and y-components of $\vec{q}'$ are also picked from this grid and the z-component is chosen from a denser linear grid. In practice, two consecutive values of q'_z are chosen from the linear grid and the two wavevectors $\vec{q}''_{min}$ and $\vec{q}''_{max}$ are determined from the conservation of crystal momentum and the two values of $\vec{q}'_z$. The frequencies of the set of phonons ($\vec{q}, \vec{q}'_{min}, \vec{q}'_{max}, \vec{q}''_{min}$ and $\vec{q}''_{max}$) are calculated for all of the phonon branches and the conservation of energy condition is then imposed by calculating the quantity, Δ

$$\Delta = \omega_j(\vec{q}) \pm \omega_{j'}(\vec{q}') - \omega_{j''}(\vec{q}'') \qquad \textbf{3.11-3}$$

for both the minimum and maximum wavevectors. If these two Δ values are of opposite sign, then there exists a value of $\vec{q}'$ between the minimum and maximum values for which both of the conservation equations are solved exactly. By assuming that the phonon frequencies vary linearly between the end points $\omega_j(\vec{q}'_{min})$ and $\omega_j(\vec{q}'_{max})$, a reasonable assumption given that the two values are very close, the exact solution of $\vec{q}'$ is determined by interpolation. In this way, the set of all allowable three-phonon scattering processes are found and recorded.

The energy conserving δ-function can be written in terms of the z-component of $\vec{q}'$ in the following way

$$\delta\left(E_j(\vec{q}) \pm E_{j'}(\vec{q}') - E_{j''}(\vec{q}'')\right) = \sum_i \left(\left|\frac{\partial f}{\partial q_{z_i}'}\right|\right)^{-1} \delta(q_z' - q_{z_i}') \qquad \textbf{3.11-4}$$

where the differential can be evaluated as

$$\frac{\partial f}{\partial q_{z_i}'} = \frac{\partial E_j(\vec{q})}{\partial q_{z_i}'} \pm \frac{\partial E_{j'}(\vec{q}')}{\partial q_{z_i}'} - \frac{\partial E_{j''}(\vec{q}'')}{\partial q_{z_i}'} \qquad \textbf{3.11-5}$$

Since $E_j(\vec{q})$ is not a function of q'_z, the first term on the right-hand side of 3.11-5 is zero. The conservation of crystal momentum (3.3-11) can then be used to show that

$$\frac{\partial(q_z \pm q_z^{'} - q_z^{''} - K_z)}{\partial q_{z_i}^{'}} = 0$$

$$\frac{\partial q_z}{\partial q_{z_i}^{'}} \pm \frac{\partial q_z^{'}}{\partial q_{z_i}^{'}} - \frac{\partial q_z^{''}}{\partial q_{z_i}^{'}} - \frac{\partial K_z}{\partial q_{z_i}^{'}} = 0$$

3.11-6

Since q_z and K_z have no dependence on q'_z, the first and last terms in 3.11-6 are zero. This means that the following condition can be derived

$$\partial q_z^{''} = \pm \partial q_z^{'}$$

3.11-7

The choice of sign depends on the type of scattering process (i.e. one or two phonons created/destroyed). 3.11-7 can then be used in conjunction with 3.11-5 to show that

$$\frac{\partial f}{\partial q_{z_i}^{'}} = \hbar[\pm v_{\lambda' z} \mp v_{\lambda'' z}]$$

3.11-8

where the phonon velocity $v_{\lambda z} = \partial \omega_{\lambda z}/\partial q_z$ is calculated from the full phonon dispersions. Since the δ-function in 3.11-4 uses the absolute value of this quantity, it is the absolute value of the difference between the z-component of the group-velocities of phonon $\vec{q}'$ and $\vec{q}''$ that is required. The sum over i is dealt with by only considering allowed scattering processes when performing the search over the Gaussian grid. The crystal volume, V appearing in 3.11-1 can be written in terms of the lattice constant, a as $V/N = a^3/4$ and so the quantity $Q_j(\vec{q})$ can now be written

$$Q_j(\vec{q}) = \frac{\hbar^4 a^3}{128\pi^2} \sum_{j'j''} \int \int dq_x^{'} dq_y^{'} \frac{\left(\widetilde{W}_{\lambda\lambda'\lambda''}^{+} + \frac{1}{2}\widetilde{W}_{\lambda\lambda'\lambda''}^{-}\right)}{|v_{j'}(q_z^{'}) - v_{j''}(q_z^{''})|}$$

3.11-9

This expression for $Q_j(\vec{q})$ can be calculated numerically (assuming the existence of the required IFCs) for any specified Gaussian and linear reciprocal space q'_z grids.

3.11.1 Numerical iteration technique

In order to calculate κ_L, a Gaussian grid for defining the wavevector of phonon $\vec{q}$ and the x- and y-components of phonon $\vec{q}'$ as well as a linear grid for the z-component of $\vec{q}'$ are required. An N-point Gaussian grid has N^3 points in the first Brillouin zone. The first Brillouin zone[29] for diamond and zinc-blende structures is shown in Figure 3-4.
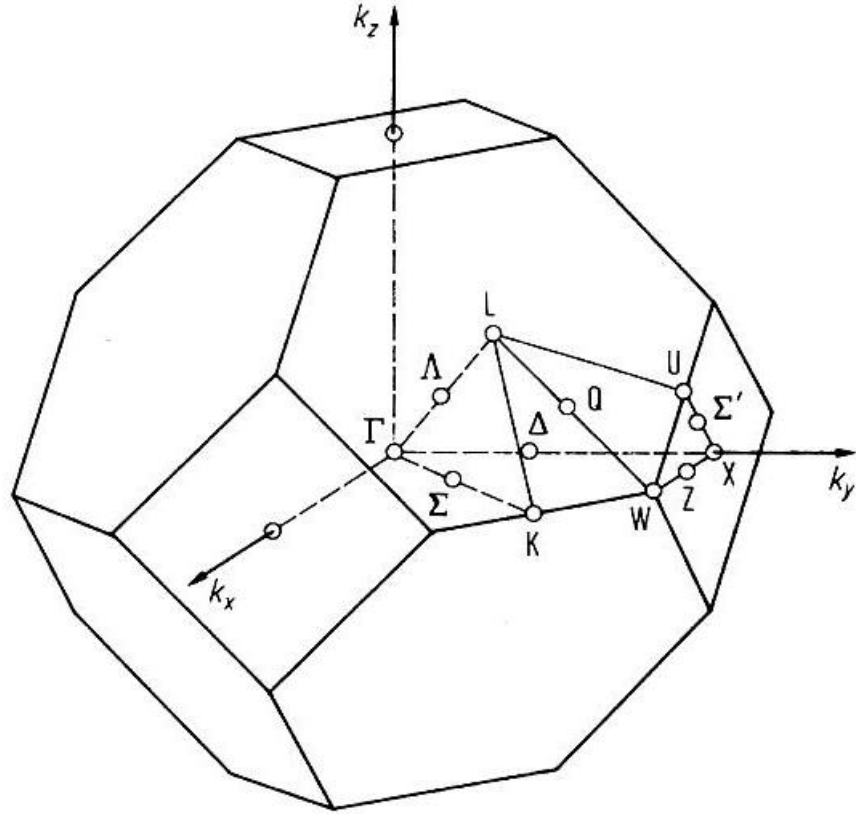
Figure 3-4; The first Brillouin zone with high-symmetry points indicated for diamond and zinc-blende materials.

It is clear from Figure 3-4, that when constructing both the Gaussian and the linear grids, some of the points will fall outside of the Brillouin zone. These points are discarded from the calculations. Any errors introduced by throwing away points should be minimized by systematically increasing the density of the both grids. For all points on the Gaussian grid, all three-phonon scattering processes that obey the conservation equations outlined in 3.11-10 are found and their scattering times, $W^{\pm}_{\lambda\lambda'\lambda''}$ are calculated.

$$\vec{q} \pm \vec{q}\,' = \vec{q}\,'' + \vec{K}$$

$$\omega_j(\vec{q}) \pm \omega_{j'}(\vec{q}') = \omega_{j''}(\vec{q}'')$$

3.11-10

After the three-phonon scattering phase space has been characterized in this manner, the quantity $Q_j(\vec{q})$ and the zeroth-order solution, $F^0_{j\alpha}(\vec{q})$ are calculated on all Gaussian grid points. Since

27

the z-component of $\vec{q}'$ and all components of $\vec{q}''$ are not constrained to lie on the Gaussian grid points, the quantities $F_{j'}(\vec{q}')$ and $F_{j''}(\vec{q}'')$ are found by interpolating the values of $F_j(\vec{q})$ (i.e. $F_j^0(\vec{q})$ on the first iteration) on the grid points surrounding the value of q'_z or $\vec{q}''$. The former case is depicted graphically in Figure 3-5.
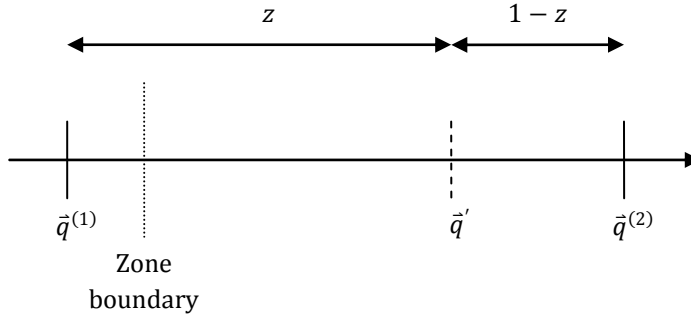

Figure 3-5; Interpolation of the function $F_{j'}(\vec{q}')$.

Points $\vec{q}^{(1)}$ and $\vec{q}^{(2)}$ lie on Gaussian grid points and so the values of $F_j(\vec{q})$ are defined at these points. The fraction z defines the position of the $\vec{q}'$ vector between the two neighboring Gaussian points. Using the value of z, the non-equilibrium function $F_j(\vec{q}')$ is defined as

$$F_{j'}(\vec{q}') = (1-z)F_j\left(\vec{q}^{(1)}\right) + zF_j\left(\vec{q}^{(2)}\right) \qquad \textbf{3.11-11}$$

It is possible that the vector $\vec{q}'$ lies between a Gaussian point and the zone boundary (as would be the case if the zone boundary were positioned as indicated in Figure 3-5). In these circumstances, it is assumed that $F_{j'}(\vec{q}') = F_{j'}\left(\vec{q}^{(2)}\right)$. Any errors introduced by this assumption are assumed to become negligible in the limit of an infinite grid. These assumptions are demonstrated to be valid by determining the convergence of κ_L with increasing grid density.

For the vector $\vec{q}''$, the eight vertices of the cube defined by the Gaussian grid points surrounding $\vec{q}''$ are used in a similar manner to find the value of $F_{j''}(\vec{q}'')$. With the interpolated values of $F_{j'}(\vec{q}')$ and $F_{j''}(\vec{q}'')$, the first order solution, $F_{j\alpha}^1(\vec{q})$ is found from equation 3.8-7. This first-order solution is then used in the interpolation scheme to calculate the nth-order solution. After each iteration, κ_L is

calculated and the iteration terminates when convergence in κ_L is achieved (typically ~30 iterations for room temperature calculations). Figure 3-6 shows the convergence in κ_L as a function of the number of iterations for diamond at room temperature (300K). Included in the plot are the convergences for an 8 point (solid curve), 16 point (dashed curve) and 32 point (dotted curve) Gaussian quadrature grid.
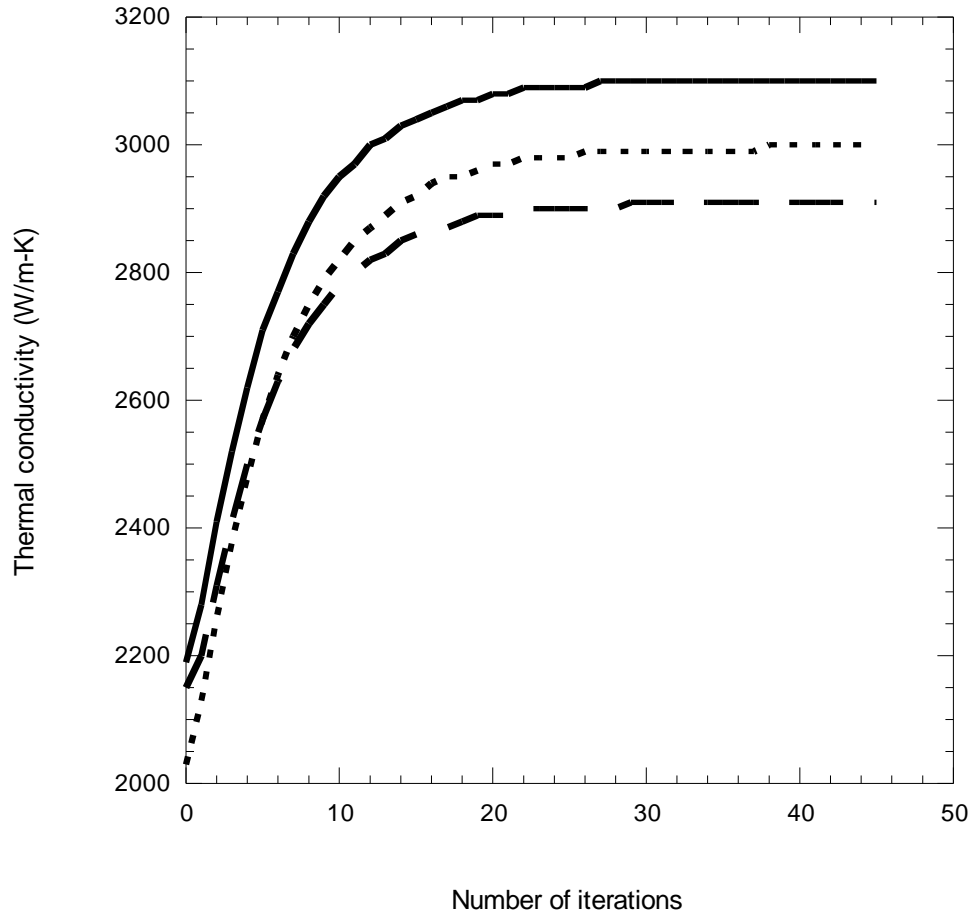
Figure 3-6; Calculated intrinsic lattice thermal conductivity of diamond at 300K as a function of the number of iterations for 8 point (solid curve), 16 point (dashed curve) and 32 point (dotted curve) Gaussian quadrature grids.

For completeness, Figure 3-7 shows the convergence of κ_L of diamond at 300K with increasing point density in the linear grid used for defining q'_z. As in the previous plot, curves are included for

an 8 point (solid curve), 16 points (dashed curve) and 32 point (dotted curve) Gaussian quadrature grid.
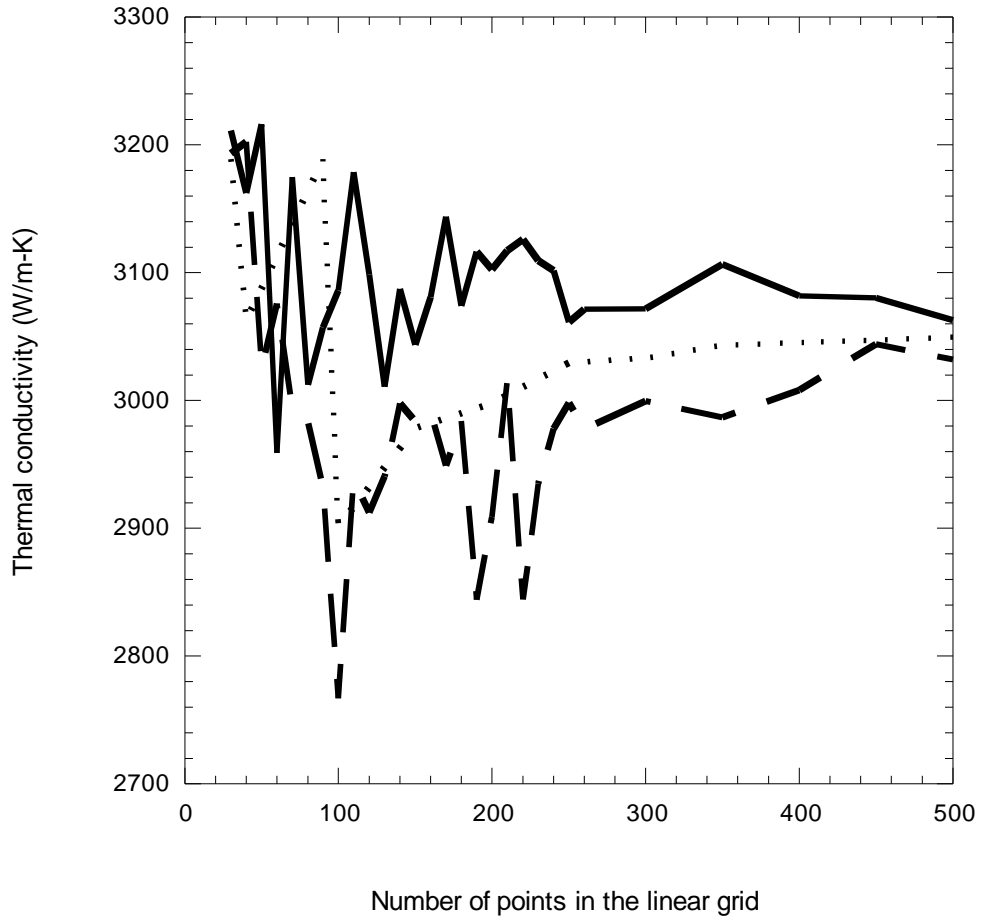
Figure 3-7; Calculated intrinsic lattice thermal conductivity of diamond at 300K as a function of the number of points in the linear grid for an 8 point (solid curve), 16 point (dashed curve) and 32 point (dotted curve) Gaussian quadrature grid.

Diamond is selected to demonstrate the convergence tests as diamond is an unusual material. It has a very small phase space for umklapp scattering and so it takes longer for convergence to be achieved. Similar plots for materials such as silicon show much more rapid convergence with less variation with iteration or grid density.

Inevitably, computational resources (processing time as well as memory requirements) limit the size of the grids used for the κ_L calculations. For example, performing the three-phonon phase space search for Gaussian quadrature grids above 32 points is impracticable due to the sizes of the output files and the processing time required. Using a 32 point grid generates output file on the order of 2Gb and takes a number of processor months for group IV materials and two to three times longer for III-V semiconductors (due to the inclusion of a macroscopic electric field). In this study all calculations are performed on a 32 point Gaussian grid with 200 points in the linear q'_z grid.

3.11.2   Crystal symmetries

In order to maximize the speed of the calculations, certain crystal symmetries are exploited. In order to determine the phonon frequencies in the entirety of the first Brillouin zone, only those in the irreducible wedge (which is one forty-eighth the size of the whole zone) need to be calculated. These calculated frequencies are then mapped into the remainder of the zone. Since all of the materials considered are cubic, the explicit symmetry operations involve all combinations of $\{q_x, q_y, q_z\} \rightarrow \{\pm q_x, \pm q_y, \pm q_z\}$ and all cyclic permutations of $\{q_x, q_y, q_z\} \rightarrow \{q_x, q_z, q_y\}$. There are eight of the first symmetry operations and six of the second, leading to a forty-eight-fold symmetry in the phonon frequencies.

In the calculation of κ_L, the phonon group velocity is required and this quantity does not satisfy the permutation symmetry, e.g. $v_z(q_x, q_y, q_z) \neq v_z(q_x, q_z, q_y)$. The group velocities therefore are calculated over the positive eight of the Brillouin zone and these are mapped into the remainder of the zone using the following condition: $v_z(q_x, q_y, \pm q_z) = \pm v_z(q_x, q_y, q_z)$. In calculating the z-component of the group velocity, setting $q_{x,y} \rightarrow -q_{x,y}$ leaves v_z unchanged, however setting $q_z \rightarrow -q_z$ changes the sign of v_z.

The function $Q_j(\vec{q})$ exhibits the symmetries of the phonon frequencies and $F_j(\vec{q})$ exhibits the symmetries of the phonon group velocities.

31

3.12 Mode Grüneisen parameters

Mode Grüneisen parameters are an important property of materials that provide a measure of the anharmonicity of the crystal. They are a material parameter that can be obtained experimentally and so provide a means of comparing the calculations performed in this study with physical measurements. The linear thermal expansion coefficients can also be calculated from the mode Grüneisen parameters and so their calculation is an important part of this study. Two methods of calculating the mode Grüneisen parameters are employed. The first involves only the harmonic IFCs, while the second requires both the harmonic and the third-order anharmonic IFCs.

3.12.1   Second-order IFC method

The mode Grüneisen parameters are defined as the change in the phonon mode frequency with a small change in the crystal volume

$$\gamma_j(\vec{q}) = -\frac{V}{\omega_j(\vec{q})}\frac{\partial \omega_j(\vec{q})}{\partial V}$$

3.12-1

Numerically, the Grüneisen parameters are obtained by calculating the phonon frequencies at lattice constants slightly offset from the equilibrium lattice constant and evaluating the following,

$$\gamma_j(q) = -\frac{V^0}{\omega_j^0(\vec{q})}\frac{\left[\omega_j(a+\delta a) - \omega_j(a-\delta a)\right]}{\left[V(a+\delta a) - V(a-\delta a)\right]}$$

3.12-2

where $\omega_j^0(\vec{q})$ is the phonon frequency and V^0 is the unit cell volume at the equilibrium lattice constant and $V(a \pm \delta a)$ is the unit cell volume evaluated at a lattice constant slightly larger or smaller that the equilibrium value. The values of the Grüneisen parameters calculated in this way can be dependent on the choice of δa. In order to remove any possible dependence, the phonon frequencies are calculated for a range of lattice constants on a linear grid centered on the equilibrium lattice constant. Each of these calculations requires the calculation of a new set of harmonic IFCs for the given lattice constant. The gradient $\partial \omega_j(\vec{q})/\partial V$ is then calculated using linear regression techniques and the Grüneisen parameter is determined for the $j, \vec{q}$ pair under consideration.

There are some choices of j and $\vec{q}$ for which the Grüneisen parameter is not well defined (e.g. the zone center acoustic phonons for which the frequency at the equilibrium lattice constant is zero). In order to ensure that all of the Grüneisen parameters are well defined, only those with an R-squared value (a least-squares measure of the linear regression fit) of 0.98 or greater are used (for example, in Figure 6-4, there is no data for the acoustic Grüneisen parameters close to the gamma point – open diamonds).

3.12.2 Third-order anharmonic IFC method

Since the Grüneisen parameters provide a measure of the anharmonicity of the crystal, it is to be expected that they can be calculated from the third-order anharmonic IFCs. The expression for the parameters in terms of these IFCs is[7,30]

$$\gamma_j(\vec{q}) = -\frac{1}{6\omega_j^2(\vec{q})} \sum_\kappa \sum_{l'\kappa'} \sum_{l''\kappa''} \sum_{\alpha\beta\gamma} \Phi_{\alpha\beta\gamma}(0\kappa, l'\kappa', l''\kappa'') \frac{e_{\alpha\kappa}^{j*}(\vec{q}) e_{\beta\kappa'}^{j}(\vec{q}')}{\sqrt{M_\kappa M_{\kappa'}}} e^{iq\cdot\vec{R}_{l'}} \vec{r}_{l''\kappa''\gamma} \qquad \textbf{3.12-3}$$

where $\vec{r}_{l\kappa\gamma}$ is the γth component of the vector locating the κth atom in the lth unit cell. The second-order IFCs are still required for calculation of the phonon frequencies and eigenvectors, $e_{\alpha\kappa}^{j}(\vec{q})$.

The experimental characterization of mode Grüneisen parameters is typically limited to high symmetry points. As a result of this, direct comparison of calculation and measurement is difficult over the whole Brillouin zone. Since the accuracy of the harmonic IFCs has been established through comparison with measured phonon dispersions, comparing the two calculation methods of the Grüneisen parameters provides a visual means of determining the accuracy of the anharmonic IFCs.

3.13 Linear thermal expansion coefficients

The material response to a change in temperature is a change in the interatomic bond lengths. Typically, an increase in temperature causes an increase in bond length and consequently, an increase in the crystal volume. The volumetric change as a result of temperature change is determined by the coefficient of linear thermal expansion

$$\alpha(T) = \frac{\kappa_T}{3(2\pi)^3} \sum_j \int d\vec{q}\, C_j(\vec{q}) \gamma_j(\vec{q})$$

<div align="right">3.13-1</div>

where $C_j(\vec{q})$ is the specific heat per mode and $\gamma_j(\vec{q})$ is the mode Grüneisen parameter. The values of κ_T, the isothermal compressibility[29] (itself, the inverse of the bulk modulus) for the materials considered in this study are included in Table 3-3.

Material	Isothermal compressibility[29], κ_T (dynes/cm^2)
Si	1.020×10^{-12}
Ge	1.330×10^{-12}
Diamond	2.260×10^{-13}
GaAs	1.330×10^{-12}
InAs	1.724×10^{-12}
InP	1.408×10^{-12}
GaP	1.140×10^{-12}

Table 3-3; The isothermal compressibilities[29] used in the calculations of the linear thermal expansion coefficients for all of the materials studied in this dissertation.

The calculated values of $\alpha(T)$ are very sensitive to the value of the cut-off energy, E_{cut} used in the DFPT calculations (see chapter 5 for a discussion of DFPT and specifically section 5.4 for the function E_{cut}). The electronic ground state energy and phonon dispersions are far less sensitive to this parameter and so the temperature dependence of $\alpha(T)$ is used to determine the value of E_{cut} required for the DFPT calculations.

3.14 Alternatives to the Boltzmann transport equation

The linearized phonon Boltzmann equation is only one means of calculating the thermal conductivity. Other methods exist that have advantages and disadvantages when compared with the BTE approach. Some of these methods are briefly summarized below.

3.14.1 Molecular dynamics

There are several ways of performing molecular dynamics (MD) simulations. Common methods include the "direct method" and the Green-Kubo method.[31-33] The details of these methods are not the subject of this dissertation, but a brief description of the Green-Kubo method is given to demonstrate the advantages and disadvantages of the method. The thermal conductivity is defined in terms of the autocorrelation of heat current vectors as,

$$\kappa_{\alpha\beta} = \frac{1}{V k_B T^2} \int_0^\infty \langle J_\alpha(\tau) J_\beta(0) \rangle dt \qquad \text{3.14-1}$$

where V is the system volume and $\vec{J}(\tau)$ is the heat current vector as a function of time. The heat current is calculated in terms of the time-dependent atomic coordinates, $\vec{r}_i(t)$ and the site energy $\varepsilon_i(t)$ of atom i as

$$\vec{J}(\tau) = \frac{d}{dt} \sum_i \vec{r}_i(t) \varepsilon_i(t) \qquad \text{3.14-2}$$

In order to calculate $\kappa_{\alpha\beta}$, an atomistic simulation of the evolution of an N-atom system using Newton's second law is used. Periodic boundary conditions are applied to the cell and initial atom velocities are randomly distributed based on the initial temperature. A small time step (of the order of femto-seconds) is used to allow the system to evolve. The first approximately 100ps are used to allow the system to equilibrate and then the remaining time (a typical run is often on the order of 1-5ns) is used for statistical averaging.

The above is a general overview of the process involved in a Green-Kubo calculation of the thermal conductivity. There are a number of aspects to this approach that need to be considered. Firstly, there is the issue of finite-size effects. More pronounced in the "direct method"[31] which does not employ boundary conditions in the direction of the thermal transport, but still a factor in the Green-Kubo method, κ_L is effected by the number of atoms used in the simulation. The more atoms used, the better the result, but the more computationally expensive the calculation. Interpolation techniques can be used to generate κ_L of an infinite crystal, but this requires independent calculations of a number of different cell sizes and so requires a large computational effort. While

this is a drawback, the computational requirements of the three-phonon scattering phase space calculation are also extremely demanding and so both methods suffer to a certain degree from this.

Secondly, MD methods use a classical description of the crystal lattice and do not account for quantum effects. This means that the method is only applicable in the temperature range where the quantum effects are negligible. Below the Debye temperature of a material, the quantum effects become more pronounced and so MD simulations become less accurate. For the materials considered in this study, room temperature is below the Debye temperature and so MD calculations cannot be accurately used and the solution to the linearized Boltzmann equation employed here is more suited.

One final consideration is that the MD calculations use empirical interatomic potentials to calculate the site energy, $\varepsilon_i(t)$. The major advantage of the MD method is that the anharmonicity of the crystal is contained to all orders, whereas the linearized BTE only considers the third-order anharmonic term. A representative set of empirical potentials is discussed in chapter 4. These potentials model the energy of the lattice with varying degrees of accuracy and require a set of parameters that are generated by comparison with experimentally observed properties. Accurate parameters are only available for a small number of well-studied materials and so it is difficult to extend the method to poorly studied materials. The use of ab initio methods coupled with the linearized Boltzmann equation means that there is no limitation to the materials that can be studied and the IFCs that are generated are of a far greater accuracy than those obtained from empirical interatomic potentials.

4 Empirical interatomic potentials

4.1 Introduction

The BTE lattice thermal conductivity calculations require the determination of the phonon frequencies and eigenvectors. Empirical interatomic potentials (EIPs) can be used to describe the crystal potential allowing direct calculation of these quantities. This typically involves assuming a form for the potential and then modifying a set of adjustable parameters to give lattice properties in agreement with experimental measurements. It is then a rapid and straightforward task to calculate the phonon properties. Many modern calculations utilize EIPs for describing the interatomic forces.

There are, however, a number of drawbacks associated with using these EIPs. Firstly, the adjustable parameters are usually determined by comparing calculations and measurements of a small set of physical properties. This ensures that the given potential is accurate when used in calculations of these specific properties, but is not necessarily transferable to calculations of other properties. For instance, the Keating potential discussed in section 4.2 is constructed to correctly reproduce the elastic strain of a crystal. The second-order IFCs are generated by symbolic differentiation of the potential, but the potential was not constructed with the intent of modeling these IFCs.

Secondly, this approach affords little in the realm of prediction. The parameters used in the potential are derived from comparison with experimental data. For purely predictive calculations, it is necessary to have access to the parameters without any comparison with experimental data. This is not possible and so thermal conductivity calculations can only be performed for materials for which significant experimental data already exists.

Due to the extensive use of EIPs, it is a valuable endeavor to quantify the effect of different model potentials on the calculated values of κ_L. Equivalently, it is useful to identify the importance of accurate descriptions of the phonon dispersions and crystal anharmonicity in performing calculations of κ_L.

4.2   Keating potential[34]

The Keating model uses the crystal symmetries and invariance arguments to construct a potential for the elastic strain in a crystal. The elastic data is most sensitive to long wavelength acoustic modes, so the form of the Keating potential attempts to accurately capture the behavior of these non-dispersive modes. The Keating potential contains a central first-nearest neighbor interaction and a non-central second-nearest neighbor interaction term. This leads to a two constant model (α and β describing the central and non-central terms respectively). The form of the potential is

$$V = \frac{1}{2}\sum_l \left[\frac{\alpha}{4a^2} \sum_{i=1}^{4} \left(\vec{R}_{0i}^2(l) - 3a^2 \right)^2 + \frac{\beta}{2a^2} \sum_{i,j>i}^{4} \left(\vec{R}_{oi}(l) \cdot \vec{R}_{oj}(l) + a^2 \right)^2 \right] \qquad \textbf{4.2-1}$$

where $\vec{R}_{oi}(l) = \vec{R}_0(l) - \vec{R}_i(l)$ defines the difference in the nuclear positions of atoms in the lth unit cell and a is the lattice constant. The second-order IFCs in 3.3-2 can be generated by the symbolic differentiation of this potential evaluated at the equilibrium configuration. The constants α and β for silicon, germanium and diamond are listed in Table 4-1.

	Silicon	Germanium	Diamond
α	0.485	0.38	1.29
β	0.138	0.12	0.85

Table 4-1; Constants for the Keating interatomic potential model.

The phonon dispersion curves of silicon generated from the second-order IFCs calculated from the Keating potential are compared with experimental measurements[37] in Figure 4-1. The non-dispersive (long-wavelength) sections of the acoustic branches agree well as the model was constructed with these sections in mind. The optic branches are consistently too high, but due to their small velocities and high energies, they only contribute a very small amount to κ_L. The biggest problem with the Keating model is the failure to describe the flattening of the transverse acoustic branches which is typical of the group IV materials. To accurately describe this flattening, long-range interactions need to be included in the model (see section 4.6).
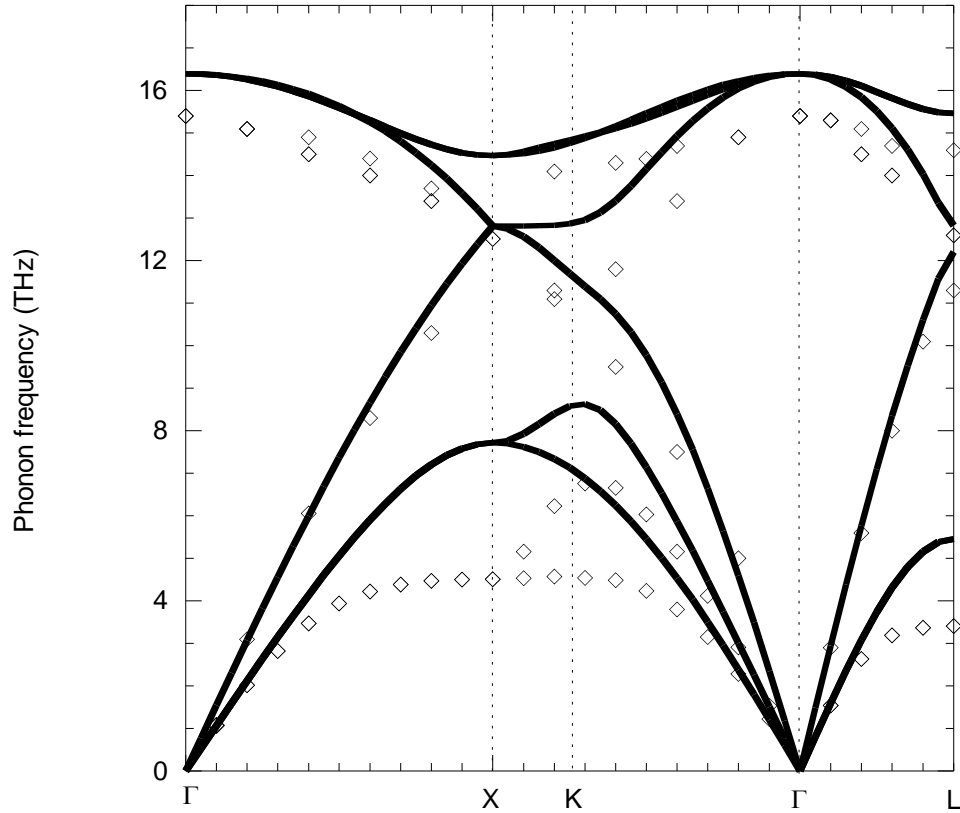
Figure 4-1; Phonon dispersion curves of silicon generated using the Keating potential[34] (solid curve) compared with experimental measurements[37] (open diamonds).

As many thermal conductivity calculations are performed using relaxation time approximations and consider the long-wavelength acoustic branches to be so dominant that these discrepancies can be ignored, potentials of this sort are still often used to calculate the second-order IFCs. The impact on the intrinsic lattice thermal conductivity of using IFCs generated from the Keating potential versus more accurate methods is investigated in section 4.7.

4.3 Tersoff potential[35,36]

The Keating interatomic potential is essentially based on a Taylor expansion centered on the minimum energy and performs poorly when used to generate phonon dispersion curves over the

entire Brillouin zone for all branches. The Tersoff potential was constructed from an observed relationship between the bond-order and local geometry of an atom. A potential of the form

$$V_{ij} = f_C(r_{ij})[f_R(r_{ij}) + b_{ij} f_A(r_{ij})]$$ **4.3-1**

is constructed, where b_{ij} is a measure of the bond-order. The functions within the potential take the forms

$$f_R(r_{ij}) = A exp(-\lambda_1 r),$$

$$f_A(r_{ij}) = -B exp(-\lambda_2 r),$$

4.3-2

$$f_C(r_{ij}) = \begin{cases} 1, & r < R - D \\ \dfrac{1}{2} - \dfrac{1}{2} \sin\left[\dfrac{\pi}{2}\dfrac{(r-R)}{D}\right], & R - D < r < R + D \\ 0, & r > R + D \end{cases}$$

The term $f_C(r_{ij})$ is a cutoff function which ranges from one at equilibrium and then drops to zero between the first and second nearest neighbor shells. The bond-order measure is given by the following.

$$b_{ij} = \left(1 + \beta^n \zeta_{ij}^n\right)^{-\frac{1}{2n}},$$

$$\zeta_{ij} = \sum_{k(\neq i,j)} f_C(r_{ik}) g(\theta_{ijk}) exp\left[\lambda_3^3 (r_{ij} - r_{ik})^3\right],$$

4.3-3

$$g(\theta) = 1 + \frac{c^2}{d^2} - \frac{c^2}{d^2 + (h - \cos\theta)^2}$$

The Tersoff potential is characterized by the ten parameters $\{A, B, \lambda_1, \lambda_2, \lambda_3, \beta, c, d, h, n\}$. The values of these parameters for silicon are determined by calculating a variety of different physical properties and comparing to a database of measurements. Specifically, this database consists of cohesive energies of real and hypothetical bulk polytypes, bulk modulus and bond length in the diamond structure. The parameters determined are included in Table 4-2. Harmonic IFCs are then generated in an analogous manner as for the Keating model. It is again noted that the Tersoff parameters were not generated using phonon dispersions as a guide and so they are not optimized for this calculation.

Parameter	Silicon	Parameter	Silicon
A (eV)	1.8308×10^3	β	1.0999×10^{-6}
B (eV)	4.7118×10^2	n	7.8734×10^{-1}
λ_1 (Å^{-1})	2.4799	c	1.0039×10^5
λ_2 (Å^{-1})	1.7322	d	1.6218×10^1
λ_3 (Å^{-1})	1.7322	h	-5.9826×10^{-1}

Table 4-2; Parameters for silicon in the Tersoff model.

The phonon dispersions generated using the Tersoff EIP are compared with experimental measurements[37] in Figure 4-2.
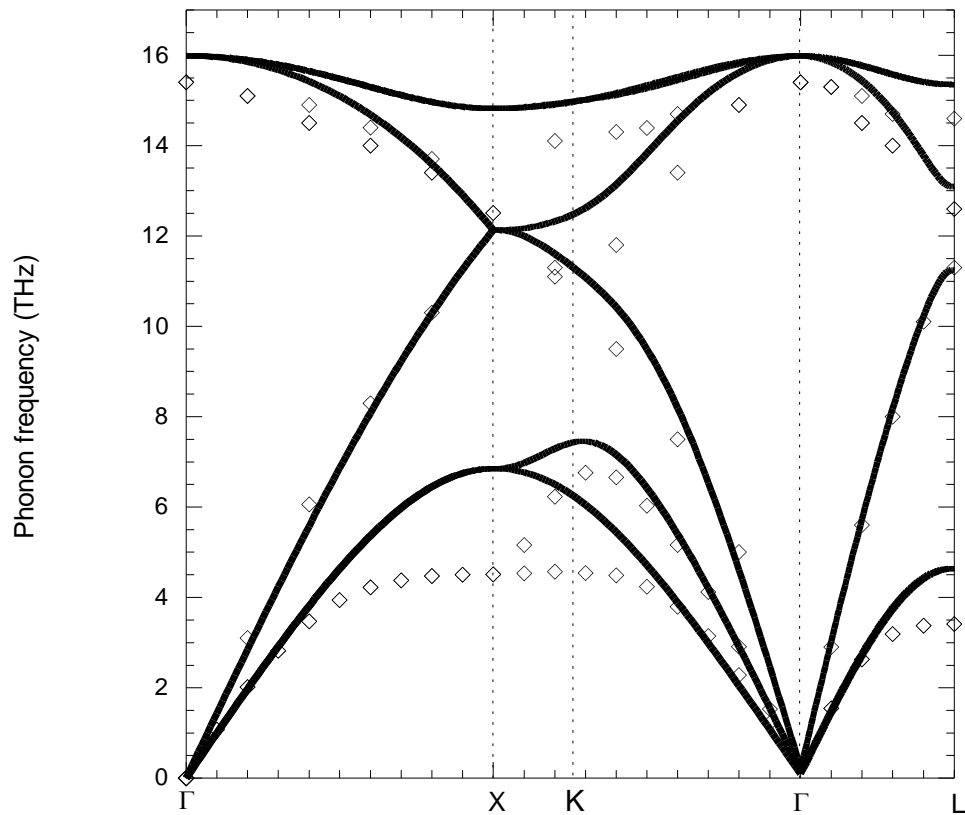

Figure 4-2; Phonon dispersion curves calculated using the Tersoff EIP (solid curves) compared with measured values.[37]

The Tersoff models' deficiency in describing the flattening of the transverse acoustic branches is clearly evident. In order to account for this flattening, some account of longer range interactions needs to be included. This is addressed in the adiabatic bond charge model described in section 4.6.

4.4 Stillinger-Weber[38]

The Stillinger-Weber (SW) EIP gives the total configuration energy $E = \sum_i E_i$ as consisting of a sum of two-body and three-body terms[38]

$$E_i = \sum_{\substack{i,j \\ i<j}} V_2(r_{ij}) + \sum_{\substack{i,j,k \\ i<j<k}} V_3(r_{ij}, r_{ik}) \qquad \text{4.4-1}$$

where r_{ij} and r_{ik} are the distances between atoms i and j and i and k respectively. The two-body term has the form $V_2(r) = A(Br^{-p} - \xi)exp[\sigma/(r - a_c)]$. The SW potential scales the energy and length to the observed atomization energy and lattice constant for silicon in the diamond structure. The parameters ξ and σ are taken to be unity. The parameter a_c gives a cutoff that causes the potential to go to zero smoothly between the first- and second nearest neighbors.

The three-body term is a product of three terms

$$V_3(r_{ij}, r_{ik}) = h(r_{ij})h(r_{ik})g(\theta_{ijk}) \qquad \text{4.4-2}$$

with

$$h(r) = exp\left(\frac{\gamma}{r - a_C}\right) \qquad \text{4.4-3}$$

and

$$g(\theta) = \lambda\left[\zeta\left(1 - e^{-Q\left(cos\,\theta + \frac{1}{3}\right)^2}\right) + \eta Q\left(cos\,\theta + \frac{1}{3}\right)^2\right] \qquad \text{4.4-4}$$

where θ_{ijk} is the angle between r_{ij} and r_{ik}. The SW potential sets the parameter $\zeta = 0$ and $\eta = Q = 1$ and is thus defined by the six parameters, $\{A, B, p, a_c, \gamma, \lambda\}$[38]. The values of the parameters are in part determined by performing lattice sums and checking that the diamond structure is the most stable crystal structure. Fine-tuning of the parameters is achieved by ensuring that the melting point of silicon is in reasonable agreement with experiment.

4.5 Environment dependent interatomic potential[39,40]

The environment dependent (ED) interatomic potential is based on the same two- and three-body terms as the SW potential in equation 4.4-1. It also involves a coordination parameter, Z, which is taken to be $Z = 4$ for diamond/zinc-blende structures. The parameter $\zeta = 1$ in this case and so this potential is specified by the nine parameters, $\{A, B, p, \xi, a_c, \gamma, \lambda, \eta, Q\}$.[40] The parameters are found by comparison with a range of physical properties experimentally measured or calculated using density functional theory in the local density approximation (see section 5 for a discussion of this method).

4.6 Adiabatic bond charge model[11,12]

The adiabatic bond charge (ABC) model is a four- (six-) parameter model for diamond (zinc-blende) structures based on the bond charge models of Phillips[41] and Martin.[42] The metal-like bonding is represented with short-range central forces. Bond charges (bcs) are placed between the ions and their interactions with the ions and each other account for the covalent character. The bond charges are allowed to move adiabatically and a short-range force between the ions and bond charges is introduced to provide stability. The forces included in the ABC model are shown schematically in Figure 4-3 and are described below.
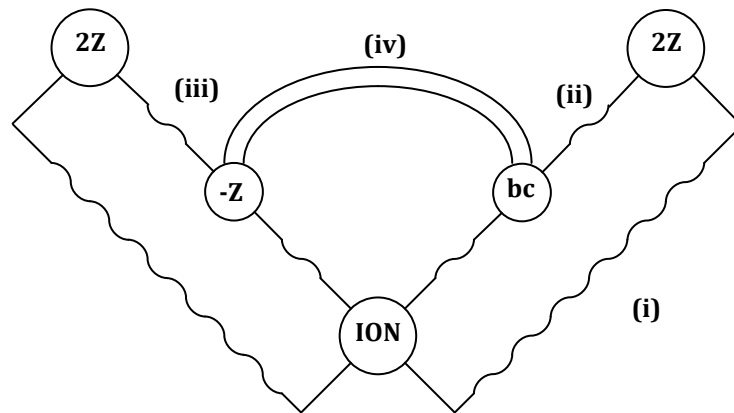

Figure 4-3; The modeled interactions in the adiabatic bond charge model.

    i.   Nearest neighbor (ion-ion) central potential, ϕ_{i-i},

    ii.   Long-range Coulomb interactions between all ions and bcs,

  iii. Ion-bc central potential,

  iv. bc-bc interactions

The cation-bc and anion-bc interactions are taken to be distinct in zinc-blende materials as are the cation-bc-cation and anion-bc-anion interactions.

Instead of defining an interatomic potential and fixing adjustable parameters, the ABC model constructs the dynamical matrix from its constituent parts discussed in the following section.

4.6.1 ABC model dynamical matrix

The dynamical matrix for the ABC model is constructed as the sum of the short-range and the long-range Coulombic parts

$$D_{\alpha\beta}(\kappa\kappa^{'};\vec{q}) = D_{\alpha\beta}^{(SR)}(\kappa\kappa^{'};\vec{q}) + D_{\alpha\beta}^{(C)}(\kappa\kappa^{'};\vec{q}) \qquad \text{4.6-1}$$

where the Coulombic part of the dynamical matrix is constructed using the Ewald transformation[43] and can be written

$$D_{\alpha\beta}^{(C)}(\kappa\kappa^{'};\vec{q}) = \frac{e^2}{V}\frac{z^2}{\epsilon}\begin{pmatrix} 4\underline{C}_R & -2\underline{C}_T \\ -2\underline{C}_T^{\dagger} & \underline{C}_S \end{pmatrix} \qquad \text{4.6-2}$$

In equation 4.6-2, the Coulombic dynamical matrices for the ion-ion, ion-bc and bc-bc interactions are written as $\underline{C}_R$, $\underline{C}_T$ and $\underline{C}_S$ respectively. In the adiabatic approximation, the bond charge masses vanish leading to the following equation of motion

$$M_{\kappa}\omega^2 U_{\alpha}(\vec{q};\kappa) = \left\{\underline{R} + 4\frac{z^2}{\epsilon}\underline{C}_R - \left[\underline{T} - 2\frac{z^2}{\epsilon}\underline{C}_T\right]\left[\underline{S} + \frac{z^2}{\epsilon}\underline{C}_S\right]^{-1}\left[\underline{T}^* - 2\frac{z^2}{\epsilon}\underline{C}_T^*\right]\right\} U_{\alpha}(\vec{q};\kappa) \qquad \text{4.6-3}$$

This means that a renormalized dynamical matrix can be written as

$$D^{(ren)} = D^{(ion-ion)} - D^{(ion-bc)\dagger}\left[D^{(bc-bc)}\right]^{-1}D^{(ion-bc)} \qquad \text{4.6-4}$$

where the individual matrices are the ion-ion, ion-bc and the bc-bc parts of the dynamical matrix. In a unit cell containing $2N$ atoms and $4N$ bond charges (where N is always even), the $18N \times 18N$ dynamical matrix in equation 4.6-1 is reduced to the $6N \times 6N$ renormalized dynamical matrix in

equation 4.6-4. The phonon frequencies $\omega_j(\vec{q})$ and eigenvectors $\hat{e}_j(\vec{q})$ are found by diagonalizing the

eigenvalue equation

$$\sum_{\kappa'\beta} \frac{1}{\sqrt{M_\kappa M_{\kappa'}}} D_{\alpha\beta}^{(ren)}(\kappa\kappa', \vec{q}) e_{\beta\kappa'}(\vec{q}) = \omega^2(\vec{q}) e_{\alpha\kappa}(\vec{q})$$

4.6-5

In order to construct the renormalized dynamical matrix, the harmonic IFCs need to be calculated.

This is the subject of the next section.

4.6.2   ABC model harmonic interatomic force constants

The harmonic IFCs for direct central potential interactions between two basis particles are given

by

$$\Phi_{\alpha\beta} = -\frac{X_\alpha X_\beta}{r_0^2}\left(\phi'' - \frac{\phi'}{r_0}\right) - \delta_{\alpha\beta}\frac{\phi'}{r_0}$$

4.6-6

where r_0 is the equilibrium distance between the two particles, X_α is the αth component of this

distance and ϕ' and ϕ'' are the first and second derivatives of the central potential evaluated at the

equilibrium separation. The bond-bending (bb) interaction gives rise to the ion-bc IFCs

$$\Phi_{\alpha\beta}^{(bb)}(ion\,\kappa, bc\,i) = -\frac{\beta_k^{(\kappa)}}{a^2}\sum_{j\neq i} X_{j\alpha}\left(X_{i\beta} + X_{j\beta}\right)$$

4.6-7

where a is the lattice constant and $\beta_k^{(\kappa)}$ is the Keating IFC that measures the strength of the bc-ion-bc

bond-bending forces with central ion labeled by $\kappa = 1,2$. Using equation 4.6-6, the IFC matrix

describing the direct interaction between ion 1 at position vector $(0,0,0)$ and bond charge 5 at

$(a/8, a/8, a/8)$ is

$$\Phi_{i-bc}(l1, l5) = -\begin{bmatrix} \alpha_1 & \beta_1 & \beta_1 \\ \beta_1 & \alpha_1 & \beta_1 \\ \beta_1 & \beta_1 & \alpha_1 \end{bmatrix}$$

4.6-8

where the constants appearing in the matrix are given by,

$$\alpha_1 = \frac{1}{3}\phi_{i-bc}''^{(1)} + \frac{2}{3}\frac{\phi_{i-bc}'^{(1)}}{r_0} + \frac{1}{2}\beta_k^{(1)},$$

4.6-9

45

$$\beta_1 = \frac{1}{3}\phi_{i-bc}^{''(1)} - \frac{1}{3}\frac{\phi_{i-bc}^{'(1)}}{r_0} - \frac{1}{2}\beta_k^{(1)}$$

In the rotated coordinate frame of the superlattice (described in section 4.8.1), this IFC matrix has the form

$$\Phi_{i-bc}(l1, l5) = -\begin{bmatrix} \alpha_1 + \beta_1 & 0 & \sqrt{2}\beta_1 \\ 0 & \alpha_1 - \beta_1 & 0 \\ \sqrt{2}\beta_1 & 0 & \alpha_1 \end{bmatrix} \qquad \textbf{4.6-10}$$

The interactions between ion 1 and the other three bond charges surrounding it are found in a similar manner. The ion-ion interactions are also found in this way and result in the same form of matrix as shown in equation 4.6-10 with the parameters α_1 and β_1 replaced by α' and β'. The bond-bending interaction with central ion $\kappa = 1$ involving bond charges i and j is found from equation 4.6-7 as

$$\Phi_{\alpha\beta}^{(bb)}(i, j) = -\frac{\beta_k^{(\kappa)}}{a^2}X_{j\alpha}X_{i\beta} \qquad \textbf{4.6-11}$$

Considering the bond charges located at the position vectors $(h1/4, 0, a/8)$ and $(-h1/4, 0, a/8)$ in the rotated superlattice coordinate system, the IFC matrix can be written as

$$\Phi_{bc-bc} = -\begin{bmatrix} \mu_1 + \nu_1 & 0 & \sqrt{2}\delta_1 \\ 0 & \mu_1 - \nu_1 & 0 \\ -\sqrt{2}\delta_1 & 0 & \lambda_1 \end{bmatrix} \qquad \textbf{4.6-12}$$

where the different parameters appearing in equation 4.6-12 are given by,

$$\mu_1 = \nu_1 = \frac{\beta_k^{(1)}}{4} + \frac{\psi_1^{''}}{2}$$

$$\delta_1 = -\lambda_1 = \frac{\beta_k^{(1)}}{4} \qquad \textbf{4.6-13}$$

$$\psi_1^{''} = -\psi_2^{''} = \left(\frac{\beta_k^{(2)} - \beta_k^{(1)}}{8}\right)$$

With all of the IFC matrices known explicitly, the dynamical matrix can be constructed. In order to diagonalize the matrix to find the phonon frequencies and eigenvectors, the four (six) parameters for the diamond (zinc-blende) structure need to be determined.

4.6.3   Adjustable parameters

The four adjustable parameters required for the diamond structures of silicon, germanium and diamond were found by Weber[11] by performing a least-squares fit to experimental elastic constants and to the neutron data of Dolling[44] and Nilsson and Nelin.[45-47] The actual fitting was performed for phonons at X, L and (0.6,0.6,0.6). The elastic constants can be calculated from the parameters in equations 4.6-9 and 4.6-13 using the following expressions,

$$fc_{11} = \frac{1}{2}\alpha + \alpha' + 2\mu + 8\mu' + 2.22\frac{z^2}{\epsilon}$$

$$fc_{12} = \beta + 2\beta' - \frac{1}{2}\alpha - \alpha' + 2\nu + 8\nu' - \mu - 4\mu' - \lambda - 4\lambda' - 28.54\frac{z^2}{\epsilon} \qquad \textbf{4.6-14}$$

$$fc_{44} = \frac{1}{2}\alpha + \alpha' + \mu + 4\mu' + \lambda + 4\lambda' - 1.11\frac{z^2}{\epsilon} - \frac{\left(\frac{1}{2}\beta + \beta' - 17.65\frac{z^2}{\epsilon}\right)^2}{\frac{1}{2}\alpha + \alpha'}$$

The zone center mode could not be used for the fitting as ϕ''_{i-i} and ϕ''_{i-bc} enter into the expressions for the elastic constants and the zone center mode in the same linear combination. The values of the parameters found from the fitting are shown in Table 4-3.

	C	Si	Ge
$\frac{1}{3}\phi''_{i-i}$	-10.0	6.21	6.61
$\frac{1}{3}\phi''_{i-bc}$	50.0	6.47	5.71
z^2/ϵ	0.885	0.180	0.162
β	12.56	8.60	8.40

Table 4-3; Adjustable parameters for the adiabatic bond charge model.

The phonon dispersions of silicon generated using the ABC model are compared with the experimentally measured values[37] in Figure 4-4.
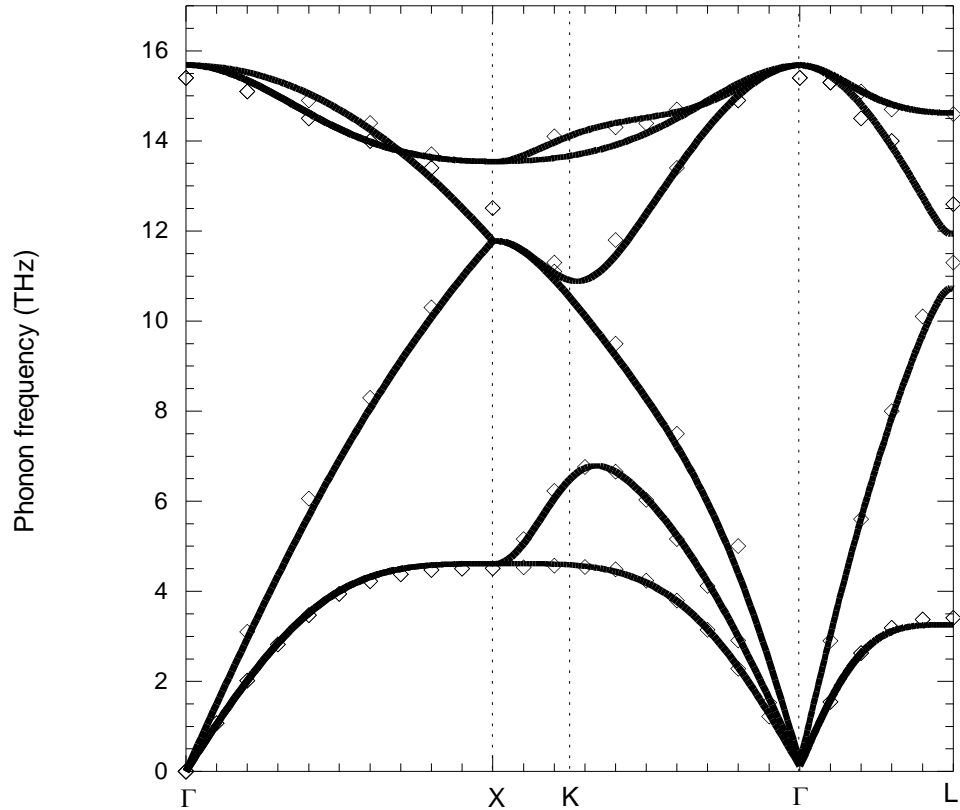
Figure 4-4; Phonon dispersion curves of silicon generated using the ABC model (solid curves) compared with the experimentally measured values (open diamonds).[37]

It should be borne in mind that the adjustable parameters shown in Table 4-3 are found by comparison with experimental phonon dispersions, amongst other parameters. It can be argued that the comparison of the phonon dispersions generated by way of the EIPs introduced in the previous sections with those calculated using the ABC model are not fair. This is a result of the fact that the adjustable parameters for the EIPs were not determined with any reference to the phonon dispersions. While this argument is valid, the failure of the EIPs to accurately reproduce the flattening of the transverse acoustic branches is a result of only modeling short-range forces. There is no way of defining a set of adjustable parameters for these models that would accurately describe this flattening effect. The inclusion of long-range Coulombic forces in the ABC model addresses this problem and allows the accurate calculation of these phonon modes.

The improvement over the EIPs previously described and shown in Figure 4-1 and Figure 4-2 is clear. The flattening of the transverse acoustic branches is accurately represented and agreement over the whole Brillouin zone is extremely good.

4.6.4 Third-order anharmonic interatomic force constants

In order to take account of the crystal anharmonicity, only nearest-neighbor central potential third-order anharmonic IFCs are considered. By only considering these interactions, only one additional parameter, $\phi_{ion-ion}^{'''}$, is required. The IFCs are obtained from equation 4.6-15[48]

$$\Phi_{\alpha\beta\gamma} = -\left[\frac{X_\alpha X_\beta X_\gamma}{r_0^3} \left(\phi''' - 3\frac{\phi''}{r_0} + 3\frac{\phi'}{r_0^2} \right) + \frac{1}{r_0^2} \left(\phi'' - \frac{\phi'}{r_0} \right) \left(X_\alpha \delta_{\beta\gamma} + X_\beta \delta_{\alpha\gamma} + X_\gamma \delta_{\alpha\beta} \right) \right] \qquad \textbf{4.6-15}$$

In 4.6-15, ϕ' and ϕ'' have already been determined from the ABC model. In order to fix the new parameter, ϕ''', κ_L of each material is calculated using a trial value of ϕ'''. The resulting value of κ_L is compared with the experimental measurement, ϕ''' is modified and a new value of κ_L is calculated. This procedure is repeated until the value of ϕ''' yields the measured value of κ_L.

4.6.5 Problems with the ABC model

The phonon dispersions of group IV materials calculated using the ABC model are in extremely good agreement with experimental measurements (Figure 4-4). The corresponding curves for GaAs are compared with experimental measurements[49] in Figure 4-5. The agreement between the calculations and experimental measurements are extremely good for the majority of the zone, however, there is a clear discrepancy around the X point for the optic modes and the longitudinal acoustic mode. It has also been noted[49,50] that the longitudinal phonon eigenvectors are wrong at the X point. These problems are not expected to affect the results of the following sections and so the original parameter sets of ref. 11 are used in this study.

In addition to the problems highlighted above, the crystal anharmonicity is dealt with in a very simplistic manner that cannot hope to achieve an accurate description of the anharmonic forces and,
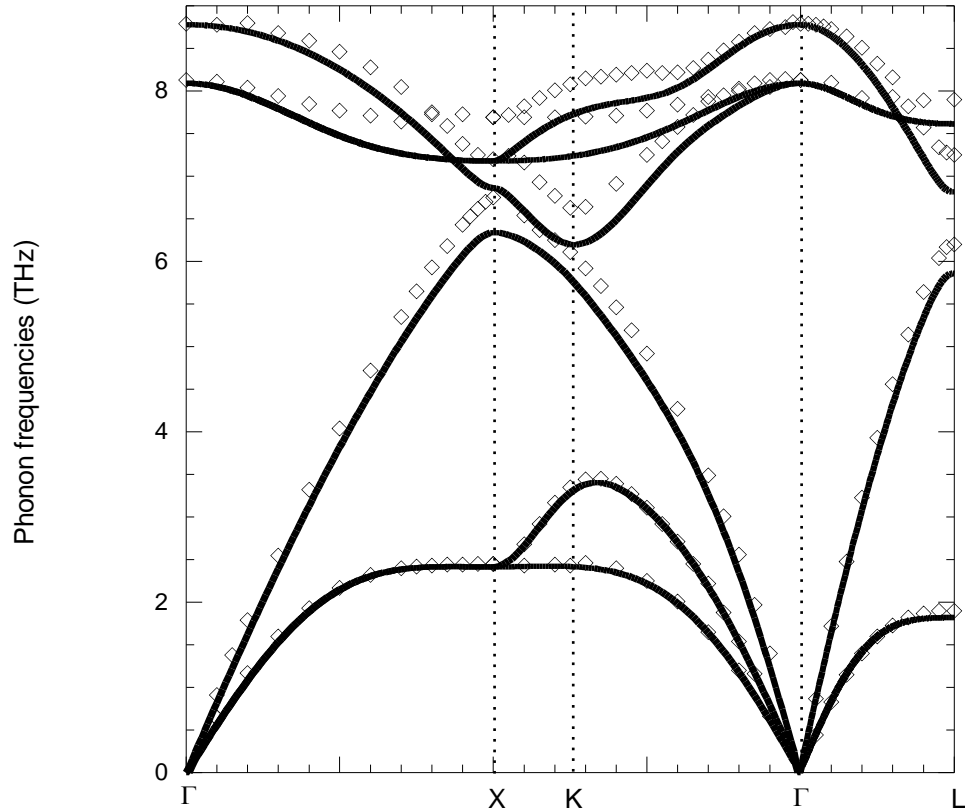
Figure 4-5; Phonon dispersion curves of GaAs generated using the ABC model (solid curves) compared with the measured values[49] (open diamonds).

similar to the EIPs, the required use of a set of adjustable parameters ensures that this model cannot be used for predictive studies.

4.7   Lattice thermal conductivity of silicon[7]

The lattice thermal conductivity of isotopically enriched and naturally occurring silicon is calculated using the BTE approach using mass variance parameters, g_2 of 2.33×10^{-6} and 2.01×10^{-4} respectively. The effective phonon mean free path, L_{eff}, that describes the boundary scattering relaxation time can be treated as an adjustable parameter to fit the low temperature measurements. Values of 1 cm and 0.3 cm are used for the isotopically enriched and naturally occurring samples respectively as they give a reasonable fit to the data and are comparable to previously used

values.[25,26,28] The BTE calculations of κ_L using the SW,[38] ED[39,40] and Tersoff[35,36] EIPs are compared with measured data[25] for both silicon samples in Figure 4-6, Figure 4-7 and Figure 4-8 respectively. In all cases, the isotopically enriched sample is represented by a solid curve (BTE calculation) and open diamonds and squares (measurements).[25] The naturally occurring sample is represented by a dashed curve (BTE calculations) and open triangles and crosses (measurements).[25]
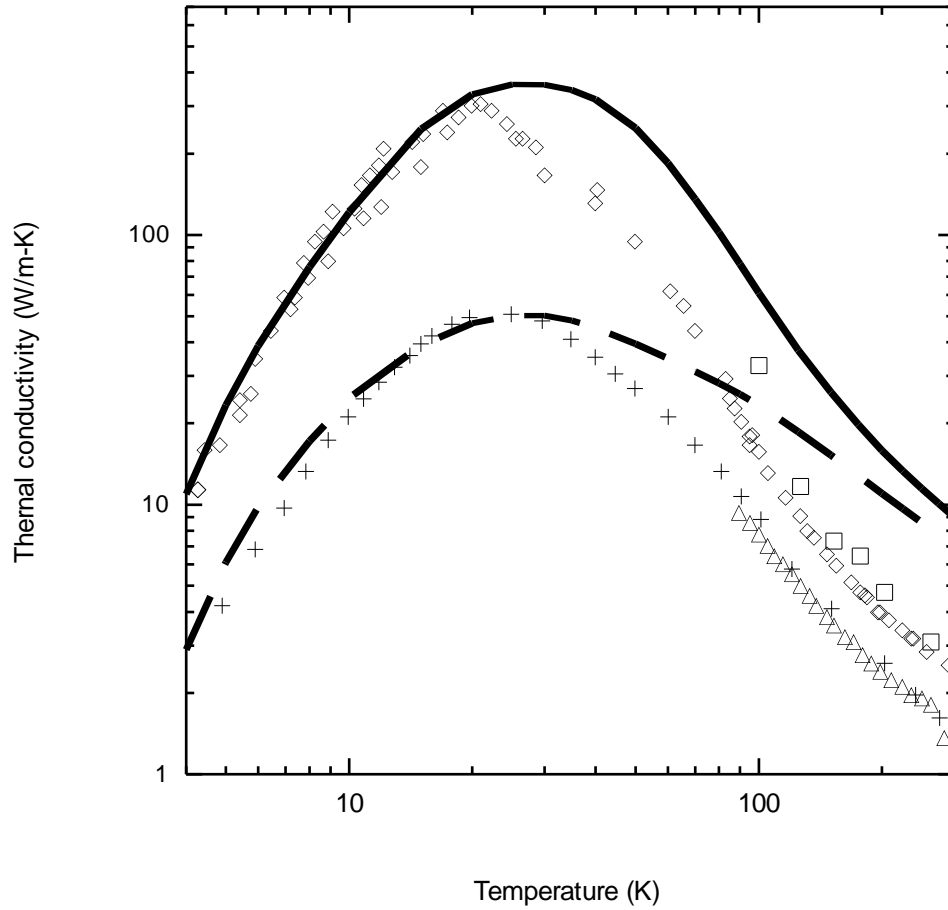

Figure 4-6; Temperature dependence of the lattice thermal conductivity of isotopically enriched and naturally occurring silicon calculated (solid and dashed curves respectively) using the SW interatomic potential. The measured values[25] are as described in the text.

In all of these figures, comparisons between calculation and measurement are good at low temperatures where the boundary scattering is dominant. Above the peak at around 30K, three-

phonon scattering and isotopic impurity scattering dominate and as temperature increases further, the three-phonon scattering processes alone dominate. The agreement with the measurements becomes significantly worse as the temperature is increased. At 300K, the measured κ_L of isotopically enriched silicon is 150W/m-K. The calculated values are 710W/m-K, 409W/m-K and 427W/m-K using the SW, ED and Tersoff interatomic potentials respectively.
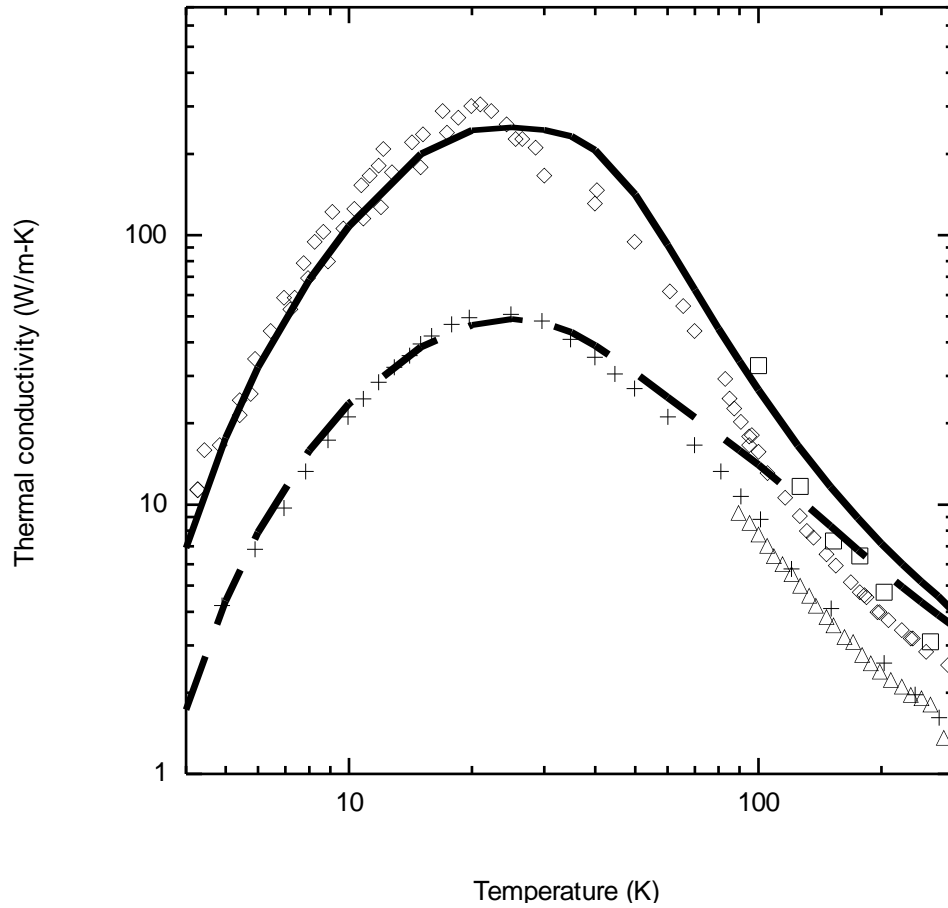

Figure 4-7; As Figure 4-6 but with calculations performed using the ED interatomic potential.

The poor fit to the data can be ascribed to the poor description of the phonon dispersions provided by the EIPs and their inability to accurately describe the crystal anharmonicity. Specifically, the failure of the EIPs to accurately reproduce the flattening of the transverse acoustic branches (see, for example Figure 4-2) yields too high phonon group velocities in the heat-carrying acoustic branches. This results in an over-prediction of κ_L. A poor description of the phonon dispersions also

means that the three-phonon scattering phase space is not accurately characterized, leading to further errors in the calculations.
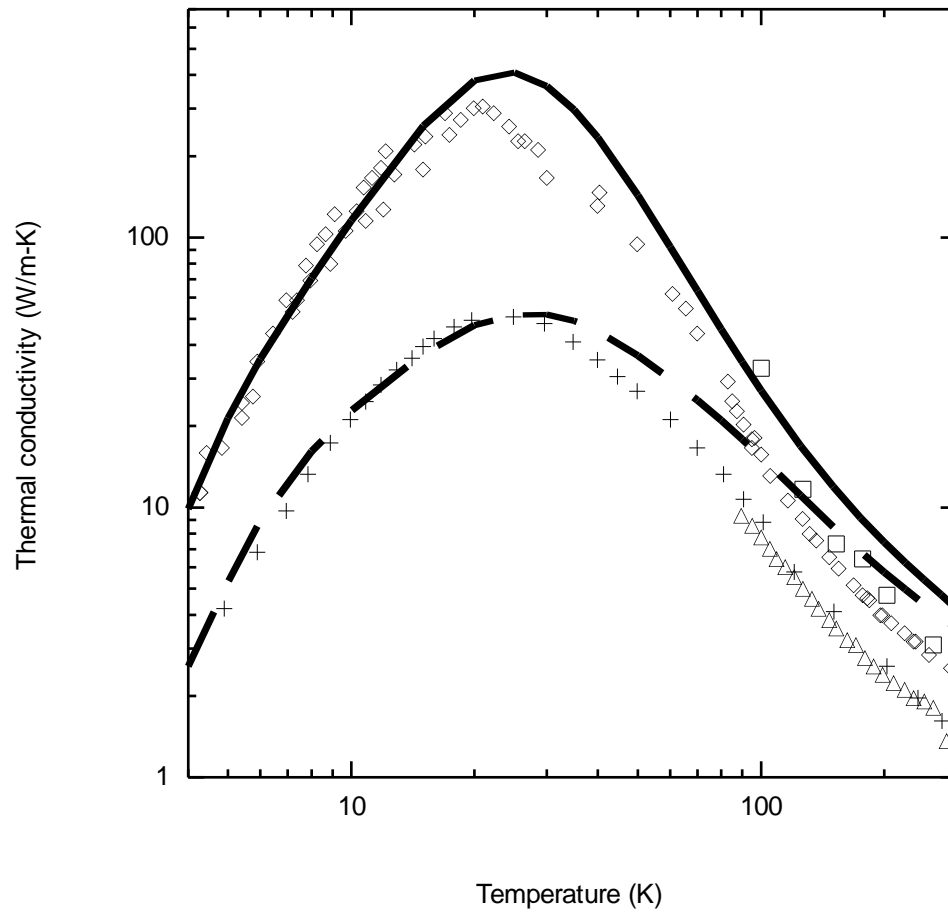

Figure 4-8; As Figure 4-6 but with calculations performed using the Tersoff interatomic potential.

The conclusions that can be drawn from these results are that any potential used to describe the crystal potential must accurately reproduce the phonon dispersion curves. Failure to do so introduces a number of errors, specifically, incorrect calculations of the phonon group velocities and the three-phonon scattering phase space which directly impact the calculations of κ_L. The three-phonon scattering rates also require calculation, demanding that the interatomic potential must also accurately describe the crystal anharmonicity. The interatomic potentials considered here do not

perform these tasks well and consequently are not suitable for use in accurate thermal conductivity calculations.

4.8   Superlattice intrinsic lattice thermal conductivity

4.8.1   Superlattice geometry

The superlattice (SL) is constructed by considering layers of atoms stacked in the z-direction [001]. The x-y plane is rotated by 45° from the coordinate system of the bulk unit cell, e.g. the new x-direction is equivalent to the $[1,-1,0]$ crystallographic direction. This means that the planes are separated by $a/4$, where a is the lattice constant, in the z-direction, but the atoms within each plane are separated by $h_1 = a/\sqrt{2}$. The four distinct layers are shown in Figure 4-9.
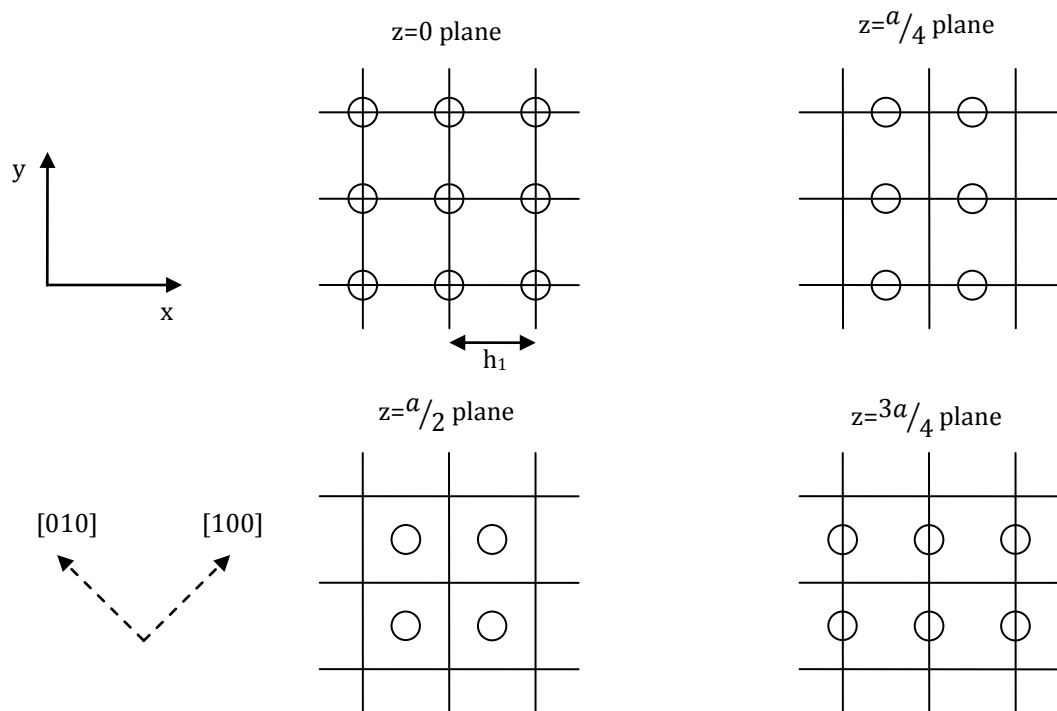

Figure 4-9; The superlattice structure in a coordinate system rotated by 45° from the coordinate system of bulk diamond materials.

The plane at $z = a$ is identical to that at $z = 0$. The SL order, N, indicates the number of consecutive layers of the same atomic species. For example, an $N = 1$ SL would consist of alternating layers of species 1 and 2 and so would be equivalent to a bulk zinc-blende material. An $N = 4$ superlattice would have four layers of species 1, followed by four layers of species 2. Consequently, the unit cell for an $N = 4$ SL would consist of eight atoms (one atom from each layer).

A major benefit of this rotated coordinate system is that the first Brillouin zone is a cuboid. When constructing the Gaussian grid for bulk materials, each Gaussian point needs to be checked to ensure that it falls within the first Brillouin zone (Figure 3-4). This is no longer necessary in the cuboidal Brillouin zone. The drawback of the cuboidal Brillouin zone is that the forty-eight-fold symmetry is replaced by an eight-fold symmetry and so the computational requirements are increased.

4.8.2   Si/Ge superlattices

The investigation of the Si/Ge SLs within the framework of the adiabatic bond charge (ABC) model allows the role of the phonon dispersion curves and the constant relaxation time approximation (CRTA) in thermal conductivity calculations to be analyzed. All calculations performed in this section are for the intrinsically pure SL lattice thermal conductivity, $\kappa_{SL}^{(i)}$, i.e. no impurity or boundary scattering terms are included. The ABC model provides a much more accurate description of the phonon frequencies than the other EIPs and so results from both can be compared to determine the importance of the specific potential. To this end, the κ_L calculations from the ABC model are compared with identical calculations using the Keating potential.

The CRTA is a common simplification of the BTE that avoids the necessity of explicitly calculating the anharmonic effects of the crystal. Replacing the calculation of $\tau_{j\beta}(\vec{q})$ in equation 3.2-5 with a CRTA allows the importance of the full anharmonic solution to be elucidated. The other important study performed in this section is the dependence of $\kappa_{SL}^{(i)}$ on the superlattice order N and the mass ratio of the constituent atomic layers. These studies are performed on a SL constructed from silicon and germanium basis atoms.[13]

All results for the Si/Ge SLs are scaled with reference to a hypothetical template material whose harmonic/anharmonic IFCs, lattice constant and masses are taken to be the geometric means of those for bulk silicon and germanium: $M_t = \sqrt{M_{Si}M_{Ge}}$ with $M_{Si} = 28.09$ and $M_{Ge} = 72.64$. The Si/Ge SL is then constructed by modifying the masses of the atoms along the SL axis (the z-direction). The masses are chosen such that M_1 (M_2) increases to fM_t (decreases to M_t/f) with $f > 1$, but the geometric mean remains equal to the template mass: $\sqrt{M_1 M_2} = M_t$. No account is taken of the crystal strain due to the modified lattice constant.

4.8.3   Effect of mass ratio and CRTA

First, the dependence of $\kappa_{SL}^{(i)}$ on the mass ratio, M_1/M_2 of the constituent atoms of the short-period Si/Ge-based SLs is investigated. The calculated values of $\kappa_{SL}^{(i)}$, scaled by that of the template material, $\kappa_t^{(i)}$, for 1×1, 2×2 and 4×4 period SLs are shown in Figure 4-10. The horizontal dotted lines show the scaled thermal conductivities of bulk silicon and germanium.

The results of the full iterative calculation are plotted with solid curves while those using the CRTA are plotted with dashed curves. The thin vertical line represents the mass ratio of germanium to silicon (i.e. when $M_1 = M_{Ge}$ and $M_2 = M_{Si}$). The CRTA calculations of $\kappa_{SL}^{(i)}$ decrease with increasing mass ratio for all SL periods. The reason for this behavior is that the acoustic branches tend to flatten with increasing M_1/M_2, which results in a lowering of the phonon frequencies and average group velocities in these branches. As the acoustic branches carry the vast majority of the heat, this reduction leads directly to a lowering of $\kappa_{SL}^{(i)}$. This effect becomes more pronounced with increasing SL period.

To illustrate this point, Figure 4-11 shows the phonon dispersion curves along the [001] direction with the x-component of the phonon momentum set to zero and the y-component set at half the size of the Brillouin zone for a 1×1 and a 2×2 Si/Ge SL.

The calculations involving the full iterative solution (solid curves) exhibit a more modest decrease in $\kappa_{SL}^{(i)}$ with increasing mass ratio than the CRTA. This behavior reflects the decrease in the phase space for three-phonon scattering that occurs for increasing M_1/M_2. The kinematic
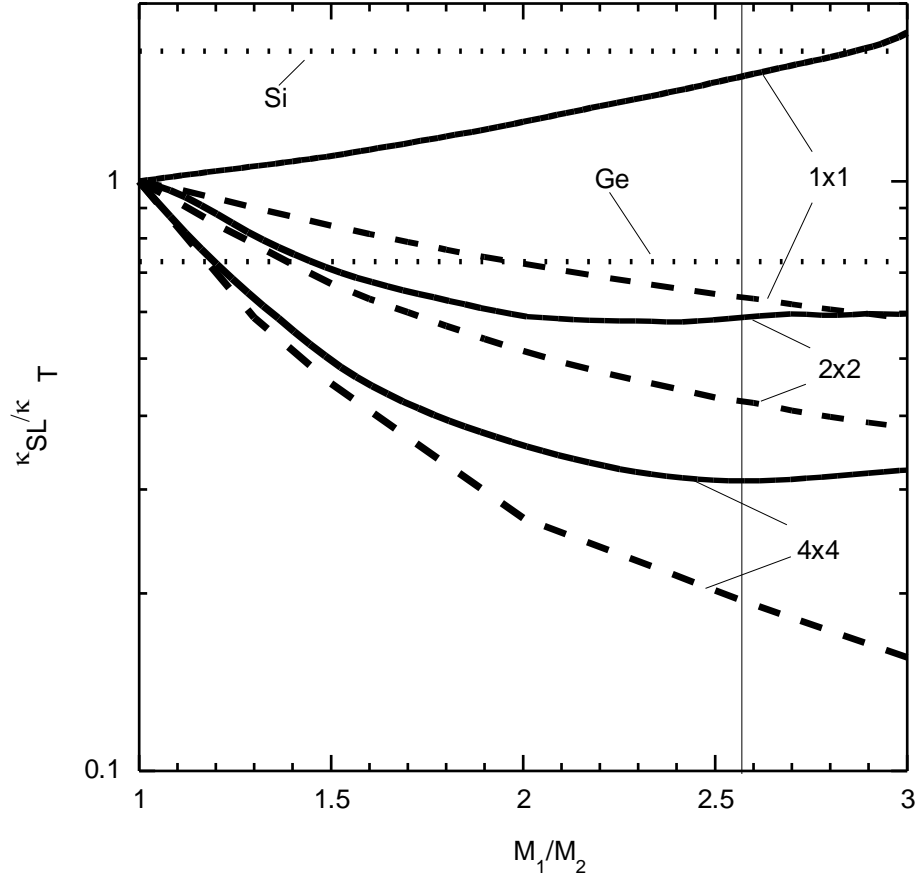

Figure 4-10; Calculated intrinsic lattice thermal conductivity $\kappa_{SL}^{(i)}$ of 1×1, 2×2 and 4×4 Si/Ge-based SLs as a function of mass ratio M_1/M_2. The dashed curves are for the CRTA while the solid curves are for the full calculation. The thin vertical line indicates the Ge/Si mass ratio. The dotted lines show the scaled $\kappa_{SL}^{(i)}$ of bulk silicon and germanium.

constraints in equation 3.11-10 dictate the three-phonon phase space and the flattening of the phonon dispersions that occurs with increasing mass ratio makes these constraints more difficult to satisfy. The corresponding reduction in the three-phonon scattering rates produces increased

scattering times, $\tau_{j\alpha}(\vec{q})$ in equation 3.2-5 and hence larger $\kappa_{SL}^{(i)}$ than in the CRTA case (a smaller
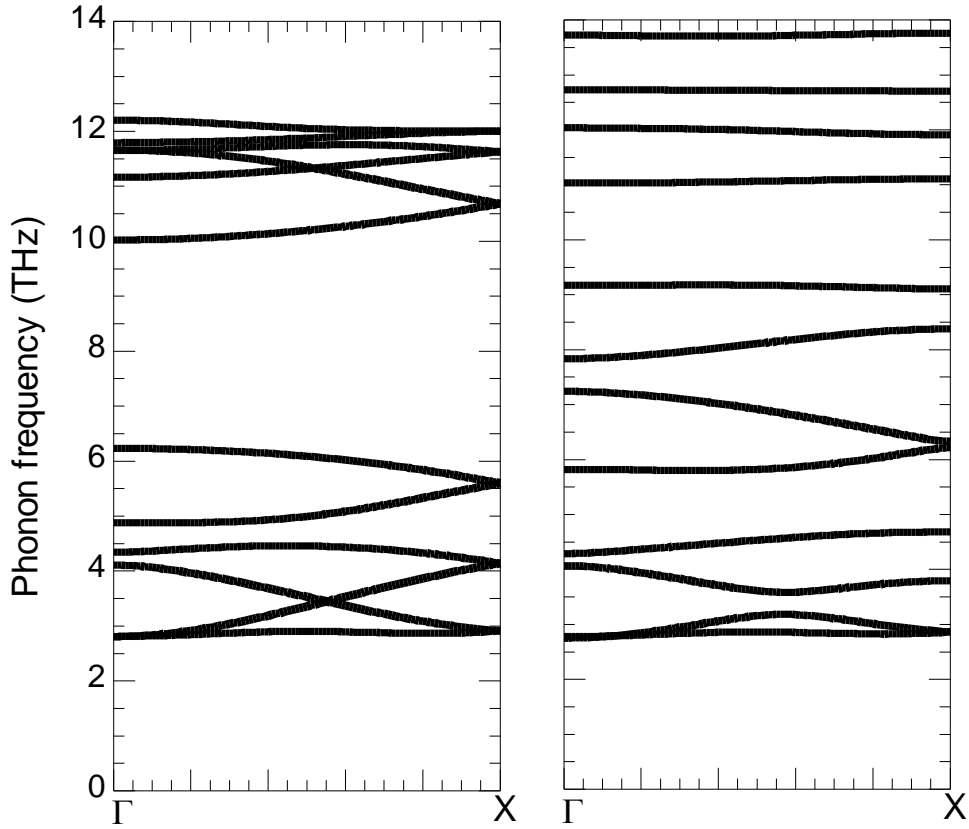

Figure 4-11; Phonon dispersion curves for a 1×1 (left) and 2×2 (right) Si/Ge-based SL along the [001] direction with fixed x- and y-components of the phonon momentum.

phase space leads to less three-phonon scattering and a corresponding decrease in the thermal resistance). It is interesting that $\kappa_{SL}^{(i)}/\kappa_t^{(i)}$ for the 2×2 and the 4×4 SLs saturate for large mass ratios at values significantly larger than the order of magnitude reduction in $\kappa_{SL}^{(i)}$, which have been predicted to occur from calculations based on the CRTA and simple phonon dispersion models.[51,52]

For the 1×1 SL the phase space reduction resulting from the increased mass ratio is strong enough to raise $\kappa_{SL}^{(i)}$ above the template value, $\kappa_t^{(i)}$. This can be understood by noting that along the [001] direction, the 1×1 SL is a zinc-blende structure with silicon and germanium as the basis atoms. It has been pointed out previously[53] that three-phonon scattering in zinc-blende materials is

reduced with increasing mass ratio because of the increased gap between acoustic and optic modes that freezes out triplet scattering channels involving acoustic-optic phonon combinations[54]. This reduced scattering causes the observed increase in $\kappa_{SL}^{(i)}$ above the template value for the 1×1 SL.

Table 4-4 lists the ratio $\kappa_{SL}^{(i)}/\kappa_t^{(i)}$ for the Si/Ge case ($M_1 = M_{Ge}$ and $M_2 = M_{Si}$) for different $N \times N$ SLs using both the CRTA (first row) and full iterative (second row) calculations. Note the higher values of $\kappa_{SL}^{(i)}/\kappa_t^{(i)}$ for the full solution over the CRTA for all cases. Also, the magnitude of the reduction in $\kappa_{SL}^{(i)}/\kappa_t^{(i)}$ decreases with increasing SL period, suggestive of the formation of a minimum, as has been observed experimentally in other SL structures.[55] Consideration of larger period SLs to verify this behavior has been precluded by CPU and memory constraints.

	1x1	2x2	4x4	8x8
CRTA	0.63	0.42	0.19	0.14
Full solution	1.42	0.59	0.30	0.20

Table 4-4; Comparison of the calculated $\kappa_{SL}^{(i)}/\kappa_t^{(i)}$ from the CRTA and full solution for 1×1, 2×2, 4×4 and 8×8 Si/Ge SLs.

To further illustrate the interplay between the flattening of the SL dispersions and the three-phonon scattering that occurs with increasing mass ratio, Figure 4-12 pots the log of the square of the three phonon matrix elements, $|\Phi|^2$, for a 4×4 Si/Ge-based SL versus the number of energy and momentum-conserving scattering events obtained from the three-phonon phase space search algorithm for a typical density of $\vec{q}$ points in the SL Brillouin zone.

The solid curve is for the template case, $M_1 = M_2 = M_t$, the crosses are for a slightly larger value, $M_1/M_2 = 1.001$, the dotted line is for $M_1/M_2 = 1.1$ and the open squares are for the case where the masses are equal to those of silicon and germanium, $M_1/M_2 = 2.58$. Consider first the template case, which exhibits a clearly separated two-peak structure. The smaller right peak corresponds to three-phonon scattering processes that contribute to the three-phonon scattering rates in 3.6-5, whereas the large left peak corresponds to the mini-umklapp processes that are unique to the SL.[56] These

mini-umklapp scattering processes are many orders of magnitude smaller than the right peak and consequently their contribution to the scattering rates is negligible. For this template case $(M_1 = M_2 = M_t)$, the SL is equivalent to a bulk lattice with the diamond structure and so the scattering strength of the mini-umklapp processes must vanish in order that the bulk thermal conductivity, $\kappa_t^{(i)}$, be recovered. This is observed in Figure 4-12.

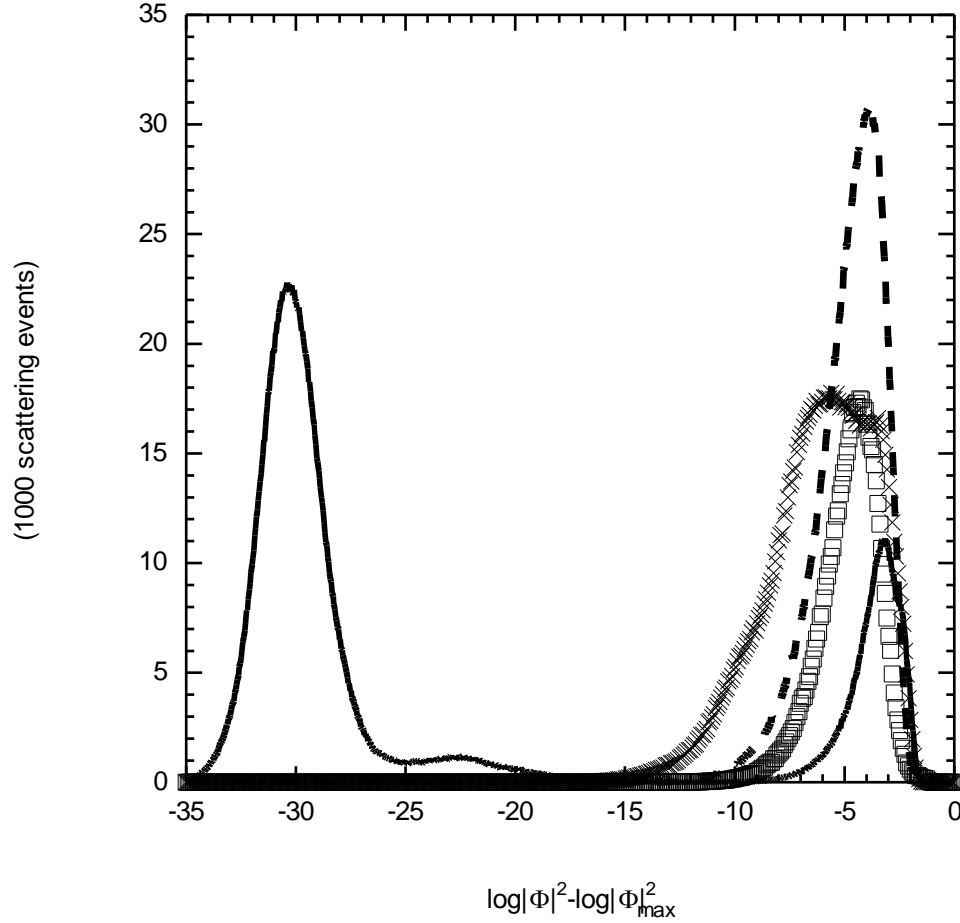**Figure 4-12; The log of the square of the three-phonon matrix elements, $|\Phi|^2$, scaled by the maximum value found for all events, $|\Phi_{max}|^2$, for a 4×4 Si/Ge-based SL versus the number of energy and momentum-conserving scattering events. The solid curve is for $M_1 = M_2$, the crosses are for $M_1 = 1.001 M_2$, the dashed curve is for $M_1 = 1.1 M_2$ and open squares are for $M_1 = M_{Ge}$ and $M_2 = M_{Si}$.**

Increasing the mass ratio from 1 to 1.001 causes the mini-umklapp peak to shift well to the right as these scattering processes now begin to contribute to the scattering rates. Further increase of the mass ratio to 1.1 produces the single strong right peak (dashed curve in Figure 4-12). The absolute number of scattering processes that contribute to $\kappa_{SL}^{(i)}$ is now significantly larger than in the $M_1/M_2 = 1$ case. However there is only a very small decrease in $\kappa_{SL}^{(i)}$ because of the overall decreased magnitudes of $|\Phi|^2$ which manifest themselves as a shift to the left of the contributing peak. As the SL period is increased, the percentage of the total scattering processes which are mini-umklapp processes increases rapidly. The behavior, however, remains as discussed above.

As the mass ratio is increased further from 1.1 to 2.58 (open squares), the number of scattering processes is strongly suppressed while the peak location is shifted only slightly to the left. This suppression reflects the decreased three-phonon phase space for the SL with increasing mass ratio, which, as discussed above, acts to raise $\kappa_{SL}^{(i)}$.

4.8.4   Effect of empirical potential

In order to quantify the significance of the potential used to calculate the phonon frequencies, the full solution of the phonon BTE is employed to calculate $\kappa_{SL}^{(i)}$ using both the Keating EIP and the ABC model. The dependence of $\kappa_{SL}^{(i)}/\kappa_t^{(i)}$ on mass ratio has been investigated[53] and the qualitative behavior is similar to that discussed in section 4.8.3. The phonon dispersion curves calculated with the ABC model (solid curves) and the Keating EIP (dashed curves) are compared with each other and experimental measurements (open diamonds)[37] in Figure 4-13.

As previously noted, the Keating potential fails to reproduce the flattening of the transverse acoustic branches. The ABC model, however, does an extremely good job of fitting the curves for all branches across the whole Brillouin zone. One of the physical reasons for the lowering of $\kappa_{SL}^{(i)}$ with increasing mass ratio is the flattening of the transverse acoustic branches in this limit which acts to lower the average group velocities. Since the Keating model significantly overestimates these

phonon frequencies, increasing the mass ratio produces an unrealistically strong reduction in the
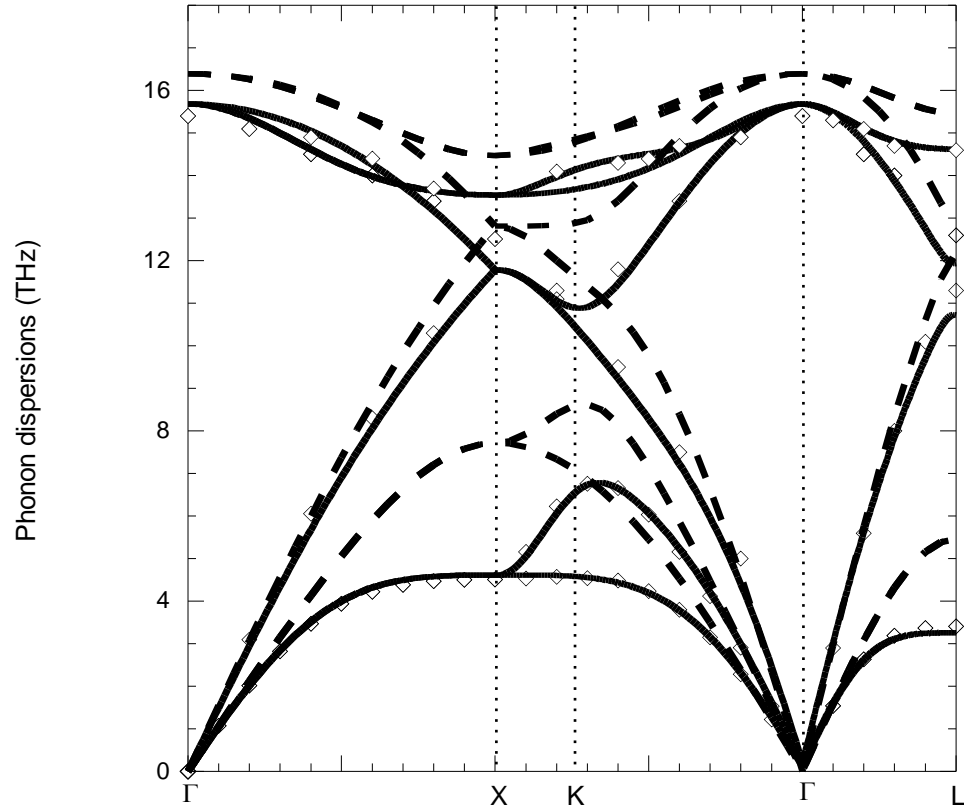

Figure 4-13; Si phonon dispersion curves for the ABC model (solid lines), Keating model (dashed lines) and experiment measurements[37] (open diamonds).

acoustic velocities and consequently, $\kappa_{SL}^{(i)}$. In contrast, the ABC models flat transverse acoustic modes show a less pronounced reduction of the group velocities, leading to a higher overall value of $\kappa_{SL}^{(i)}/\kappa_{t}^{(i)}$ compared with the Keating EIP. This behavior is illustrated in Figure 4-14.

The previous discussion considers only the *intrinsic* contribution to κ_{SL} provided by the three-phonon scattering processes. The behavior of real materials is more complicated and involves a variety of different scattering mechanisms. In the context of short-period SLs, the most important scattering mechanism is expected to be that due to the interfaces between the different atomic layers.
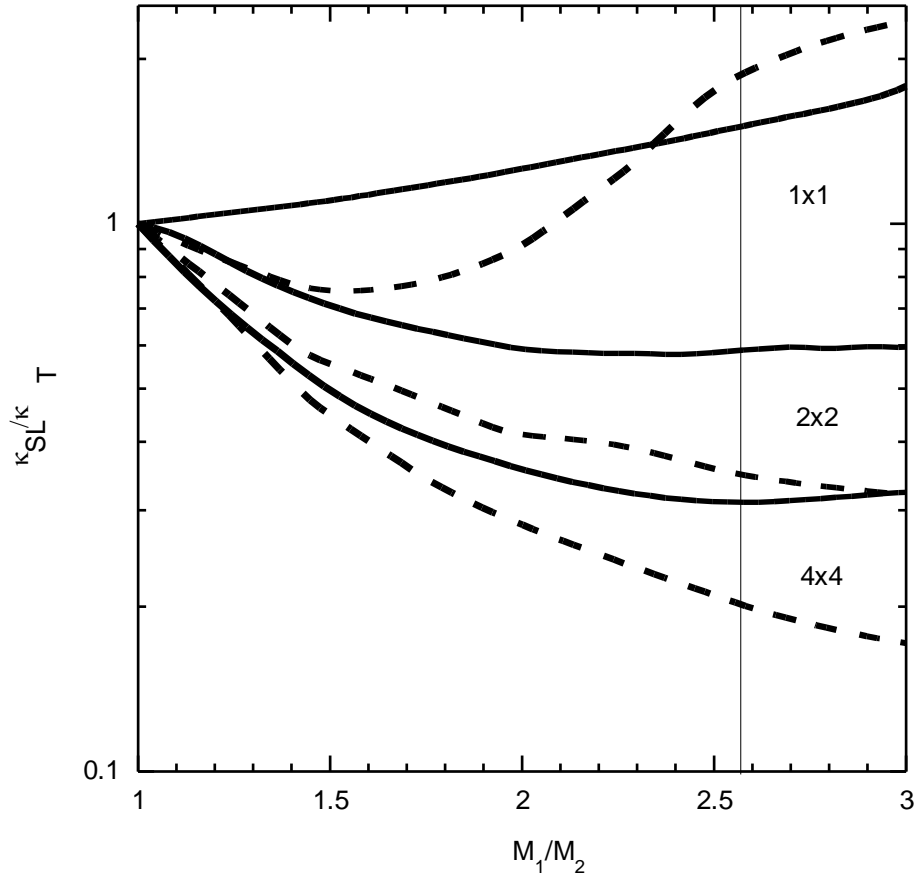
Figure 4-14; $\kappa_{SL}^{(i)}/\kappa_t^{(i)}$ **for** 1×1, 2×2 **and** 4×4 **Si/Ge based SLs as a function of the mass ratio of the constituent atoms,** M_1/M_2. **The solid curves are for the ABC model and the dashed curves are for the Keating model. The thin vertical line represents the Ge/Si mass ratio.**

The relative importance of these other scattering processes are addressed in the following section.

4.8.5   GaAs/AlAs superlattices – extrinsic processes

The lattice thermal conductivity of real SL structures is determined primarily by a combination of the intrinsic (three-phonon) scattering, $\kappa_{SL}^{(i)}$ as described in the previous sections and the extrinsic phonon scattering, $\kappa_{SL}^{(e)}$ resulting from the SL interfaces. These extrinsic processes are dependent on the particular sample and so general calculations are typically difficult to perform. The accurate calculations presented in this section allow the relative strength of $\kappa_{SL}^{(i)}$ and $\kappa_{SL}^{(e)}$ to be investigated by

comparison with experimental data. It is reasonable to assume that interface scattering will be relatively strong in short-period SLs as monolayer fluctuations represent a significant fraction of the SL period. Previously, calculations of $\kappa_{SL}^{(i)}$ have been performed for GaAS/AlAs SLs within the CRTA using a rigid-ion model[14] which accurately represents the phonon dispersions. That work demonstrated an approximate three-fold reduction in the room temperature $\kappa_{SL}^{(i)}$ of 3×3 SLs when compared with bulk GaAs and the conclusion drawn was that this represented an upper bound on $\kappa_{SL}^{(i)}$ if the phonon lifetime is reduced by the mini-umklapp scattering as suggested by Ren and Dow.[56] The measured room temperature κ_{SL}, for 3×3 GaAs/AlAs SLs was found to be reduced by a factor of seven compared to bulk GaAs.[58] Assuming that Matthiessen's rule (equation 7.3-1) holds, the CRTA results from ref. 14 suggest that the intrinsic and extrinsic contributions are comparable. This result is surprising because, as previously noted, the extrinsic contribution is expected to dominate the behavior of κ_{SL}.

To address this issue, $\kappa_{SL}^{(i)}$ has been calculated for $N \times N$ GaAs/AlAs SLs using the ABC model in the phonon BTE approach. For these calculations, an $N \times N$ SL contains $4N$ atoms per SL unit cell as opposed to the $2N$ atoms in the Si/Ge case. The calculations demonstrate that the phonon lifetimes are found to *increase* when compared with bulk GaAs. As in the Si/Ge case, the increase in $\kappa_{SL}^{(i)}$ due to the reduced three-phonon scattering phase space outweighs the decrease from the added mini-umklapp processes. The calculated room temperature values of $\kappa_{SL}^{(i)}$ for 1×1, 2×2 and 3×3 SLs are 36.8, 27.4 and 26.6W/m-K respectively. Thus, for the 3×3 SL there is a reduction of approximately 1.7 from the bulk GaAs value. This is about half that found in ref. 14. From Matthiessen's rule, this means that the reduction due to extrinsic processes is approximately three times larger than that due to intrinsic scattering. This is qualitatively consistent with expectations.

These findings are shown in Figure 4-15. The calculations using the ABC model and the full iterative solution to the phonon BTE for 1×1, 2×2 and 3×3 SLs are the dotted, dashed and solid curves respectively. The CRTA results at 100K, 200K and 300K for 2×2 and 3×3 SLs[14] are included

64

as solid triangles and open squares. Also included are the measured lattice thermal conductivities of bulk GaAs (solid circles),[57] 1×1 (plusses), 2×2 (crosses) and 3×3 (open triangles) GaAs/AlAs SLs.[58]
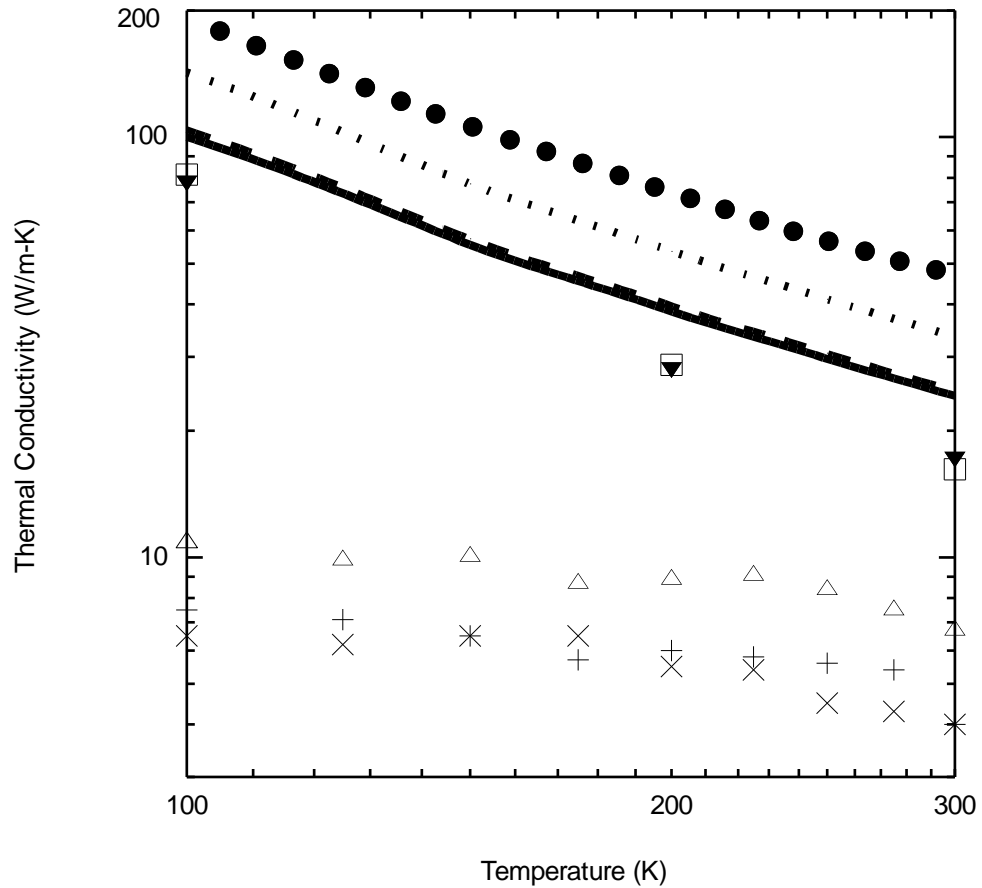
Figure 4-15; $\kappa_{SL}^{(i)}$ **for** 1×1 **(dotted curve),** 2×2 **(dashed curve) and** 3×3 **(solid curve) GaAs/AlAs SLs as a function of temperature compared to the CRTA results for** 2×2 **(solid triangles) and** 3×3 **(open squares) SLs, and to measured lattice thermal conductivities of bulk GaAs[57] (solid circles). Also included are measurements for** 1×1 **(plusses),** 2×2 **(crosses) and** 3×3 **(open triangles) GaAs/AlAs SLs.[58]**

The temperature dependence of the calculated $\kappa_{SL}^{(i)}$ is similar to that of the bulk GaAs, whereas the measured κ_{SL} of the GaAs/AlAs SLs shows a very weak dependence on the temperature. The bulk

GaAs samples are of a very high quality and so κ_{SL} is dominated by the three-phonon scattering, yielding the expected T^{-1} dependence. The GaAs/AlAs SLs, conversely have a strong contribution from the extrinsic scattering processes, specifically interface scattering between the GaAs and the AlAs layers, which masks the temperature dependent three-phonon scattering.

Also, the values of $\kappa_{SL}^{(i)}$ for the GaAs/AlAs SLs calculated with the full solution to the phonon BTE show only a modest reduction compared to those of bulk GaAs. In fact, $\kappa_{SL}^{(i)}$ is reduced by factors of 1.2 for 1×1 SLs and 1.7 for both 2×2 and 3×3 SLs over the full temperature range. The experimentally measured values,[58] on the other hand, are significantly lower than the bulk GaAs values.

Both of these observations suggest that the dominant scattering mechanism in the GaAs/AlAs SLs is not the three-phonon scattering but extrinsic processes, the most significant of which is expected to be phonon scattering at the material interfaces. This is consistent with the rough interfaces expected for short-period SLs and with results of molecular dynamics simulations.[59]

The CRTA results suggest that the intrinsic and the extrinsic scattering mechanisms are of equal importance at room temperature (the CRTA results also necessarily show the T^{-1} dependence). This is at odds with the findings here and reinforces the importance of the rigorous approach presented in this dissertation.

5 Density functional perturbation theory

Density functional theory (DFT) has grown into an extremely important, accurate method of calculating the ground state electron densities of many different systems, from molecules to infinite crystal lattices. Hohenberg and Kohn[60] showed that the total energy of a many-body system of interacting particles could be determined as a unique functional of the electron density. The minimum in this total energy functional, $E[n]$ is the ground state energy of the system. While of theoretical interest, the theory provides no practicable way of performing theoretical calculations. The work of Kohn and Sham[61] mapped the many-body problem into a non-interacting independent electron problem with all exchange and correlation effects collected into an exchange-correlation potential included in the Hamiltonian. The local density approximation (LDA) is used to calculate the exchange-correlation term, leading to lattice property calculations within a few percent of experimentally measured values. For systems whose electrons are not highly correlated, the exchange-correlation term calculated in the LDA is small and the resulting calculations are extremely accurate.

5.1 Kohn-Sham functional and equations

The Kohn-Sham functional for the electronic wavefunction ψ_i can be written

$$E[\{\psi_i\}] = 2 \sum_i \int d\vec{r}\psi_i \left[-\frac{\hbar^2}{2m}\right] \nabla^2 \psi_i + \int d\vec{r} V_{ion}(\vec{r})n(\vec{r}) + \frac{e^2}{2} \int \int d\vec{r}d\vec{r}' \frac{n(\vec{r})n(\vec{r}')}{|\vec{r}-\vec{r}'|} + E_{xc}[n(\vec{r})]$$
$$+ E_{ion}(\{\vec{R}_I\})$$

<div align="right">5.1-1</div>

In 5.1-1, $V_{ion}(\vec{r})$ is the static ion-electron potential, $E_{xc}[n(\vec{r})]$ is the exchange-correlation functional, $E_{ion}(\{\vec{R}_I\})$ is the Coulomb energy of the ions at positions $\vec{R}_I$ and $n(\vec{r})$ is the electron density given by

$$n(\vec{r}) = 2 \sum_i |\psi_i(\vec{r})|^2$$

<div align="right">5.1-2</div>

The set of wavefunctions, $\psi_i(\vec{r})$ that minimize equation 5.1-1 are the ground state electron wavefunctions. These are found by self-consistently solving the one-electron Kohn-Sham equations.

$$\left[-\frac{\hbar^2}{2m}\nabla^2 + V(\vec{r}) + V_H(\vec{r}) + V_{xc}(\vec{r})\right]\psi_i(\vec{r}) = \varepsilon_i\psi_i(\vec{r})$$

5.1-3

The Hartree potential for the electrons and the exchange-correlation potentials appearing in equation 5.1-3 are

$$V_H(\vec{r}) = e^2 \int d\vec{r}' \frac{n(\vec{r}')}{|\vec{r} - \vec{r}'|},$$

$$V_{xc}(\vec{r}) = \frac{\delta E_{xc}[n(\vec{r})]}{\delta n(\vec{r})}$$

5.1-4

and $V(\vec{r})$ is the external potential. The differential in the definition of the exchange-correlation potential is a functional derivative. The three potentials appearing in equation 5.1-3 are often collected together into a single effective potential known as the self-consistent field potential, $V_{SCF}(\vec{r})$. The key idea is that variation of the energy functional of interacting electrons under the constraint that the number of electrons remains fixed formally leads to the same equations as hold for a system of non-interacting electrons subject to the effective potential, $V_{SCF}(\vec{r})$.

The self-consistency condition means that trial wavefunctions are assumed and can then be used to find the electron density and hence the potentials defined in equation 5.1-4. These potentials can then be used to solve the Kohn-Sham equations, resulting in a new set of electronic wavefunctions. Self-consistency is achieved when the calculated wavefunctions are equal to the input wavefunctions. Note that the Kohn-Sham eigenvalues in 5.1-3 are not the single-particle ground state energies. The ground state energy of the system is the solution to equation 5.1-1 using the Kohn-Sham wavefunctions.

5.1.1 Exchange-correlation and the local density approximation

If the exchange-correlation functional appearing in equation 5.1-1 were known exactly, then the solution arrived at by the solution of the Kohn-Sham equations would be exact. This term is essentially a gathering together of the terms for which an exact form is not known, specifically the

electron-electron interactions. The accuracy of DFT calculations is necessarily dependent on the relative size of the exchange-correlation term and so, for highly correlated systems, this term becomes more and more important and DFT becomes less accurate. For the materials considered in this study, the exchange-correlation term is weak and can be dealt with in an approximate manner using several methods. The most common (and remarkably accurate) method is the use of the local density approximation (LDA). The simplest method of dealing with $E_{xc}[n(\vec{r})]$ is to assume that the exchange-correlation energy per electron at a point $\vec{r}$ in the electron gas being studied is equal to that of a homogeneous electron gas whose density is the same as that at point $\vec{r}$. In the case of the homogeneous electron gas, this has been solved exactly[62] and the results parameterized[63].

$$E_{xc}[n(\vec{r})] = \int d\vec{r}\varepsilon_{xc}^{hom}[n(\vec{r})]\,n(\vec{r})$$

5.1-5

The LDA has been used extensively and has shown remarkable agreement with experiment. Within this study, the LDA is used in all calculations. The computational methods of calculation using the parameter-less DFT formalism are often known as "ab initio" methods and so this term is used throughout this text.

The LDA is an approximation to the exchange-correlation energy and it is not surprising that problems exist with the method. Specifically, the LDA is known to "overbind", leading to lattice constants smaller than those experimentally measured. This often leads to errors in the calculation of other properties, e.g. the over-prediction of bulk moduli. In the context of this study, the main problem with the LDA is its tendency to overbind. Section 6.2 discusses some of the affects on silicon properties of using a lattice constant that is smaller than the measured value.

Many extensions to the LDA have been proposed and developed since its inception. One method in particular is the generalized gradient approximation (GGA)[64,65]. Within the GGA, the non-uniformity of the electron charge densities are accounted for by considering the local gradient of the charge density. For the case of phonon dispersions in group IV and III-V materials, however, the LDA already performs extremely well and in the case of silicon specifically, the GGA gives a poorer fit to

69

experimental data than the LDA[17,66]. For this reason, the inclusion of the GGA was unnecessary and all results in this work are performed in the LDA framework.

5.2 Linear response

The first and second derivatives of the total energy are given by the Hellmann-Feynman[67,68] theorem as

$$\frac{\partial E}{\partial \lambda_i} = \int d\vec{r} \frac{\partial V_\lambda(\vec{r})}{\partial \lambda_i} n_\lambda(\vec{r})$$

$$\frac{\partial^2 E}{\partial \lambda_i \partial \lambda_j} = \int d\vec{r} \frac{\partial^2 V_\lambda(\vec{r})}{\partial \lambda_i \partial \lambda_j} n_\lambda(\vec{r}) + \int d\vec{r} \frac{\partial n_\lambda(\vec{r})}{\partial \lambda_i} \frac{\partial V_\lambda(\vec{r})}{\partial \lambda_j}$$

5.2-1

The Hellmann-Feynman theorem is here stated in terms of a general set of parameters, $\{\lambda_i\}$. In the case of lattice dynamics, these parameters correspond to the ionic displacements. In general, this equation needs extra terms that account for the variation in the wavefunction as well as the potential. These correction are usually called "Pulay" terms.[69] In the limit of a complete basis set, the contribution from these Pulay terms tends to zero; a situation that is not possible to achieve in actual calculations. By expanding the wavefunctions in a set of plane waves, the Pulay terms vanish exactly and so the Hellmann-Feynman theorem can be confidently used in this situation. The calculations performed in this study employ a plane-wave basis and so the Pulay terms can be ignored.

In order to evaluate the terms in equation 5.2-1, standard first-order perturbation theory is used. The resulting extension of DFT is known as density functional perturbation theory (DFPT). Using perturbation theory, the first-order correction to the self-consistent field potential, ΔV_{SCF} can be written

$$\Delta V_{SCF}(\vec{r}) = \Delta V(\vec{r}) + e^2 \int d\vec{r}' \frac{\Delta n(\vec{r}')}{|\vec{r} - \vec{r}'|} + \frac{dv_{xc}(n)}{dn}\bigg|_{n=n(\vec{r})} \Delta n(\vec{r})$$

5.2-2

where

$$\Delta n(\vec{r}) = 4 \sum_{n=1}^{N/2} \psi_n^*(\vec{r}) \Delta \psi_n(\vec{r})$$

5.2-3

is the linearized variation of the density functional and N is the number of electrons. The variation of

the Kohn-Sham wavefunctions are obtained through

$$(H_{SCF} - \epsilon_n)|\Delta\psi_n\rangle = -(\Delta V_{SCF} - \Delta\epsilon_n)|\psi_n\rangle \qquad \textbf{5.2-4}$$

where

$$H_{SCF} = -\frac{\hbar^2}{2m}\frac{\partial^2}{\partial\vec{r}^2} + V_{SCF}(\vec{r}) \qquad \textbf{5.2-5}$$

is the unperturbed Kohn-Sham Hamiltonian and the first-order variation of the Kohn-Sham

eigenvalues are given by

$$\Delta\epsilon_n = \langle\psi_n|\Delta V_{SCF}|\psi_n\rangle \qquad \textbf{5.2-6}$$

The above set of equations can be solved self-consistently analogously to the original

unperturbed Kohn-Sham equations. It can be seen from equation 5.2-2 that $\Delta V_{SCF}(\vec{r})$ has a linear

dependence on $\Delta n(\vec{r})$, which itself depends linearly on the $\Delta\psi_n$. Thus the whole problem can be

written in terms of a generalized linear problem.

The first-order correction to the Kohn-Sham wavefunction can be written as a sum over the

unperturbed wavefunctions

$$\Delta\psi_n(\vec{r}) = \sum_{m\neq n}\psi_m(\vec{r})\frac{\langle\psi_m(\vec{r})|\Delta V_{SCF}|\psi_n(\vec{r})\rangle}{\epsilon_n - \epsilon_m} \qquad \textbf{5.2-7}$$

Substituting equation 5.2-7 into equation 5.2-3, the correction to the density functional can be

written

$$\Delta n(\vec{r}) = 4\sum_{n=1}^{N/2}\sum_{m\neq n}\psi_n^*(\vec{r})\psi_m(\vec{r})\frac{\langle\psi_m(\vec{r})|\Delta V_{SCF}|\psi_n(\vec{r})\rangle}{\epsilon_n - \epsilon_m} \qquad \textbf{5.2-8}$$

All terms in the sum over $m \leq N/2$, will cancel with the term where n and m are interchanged.

This means that the summation over m only needs to be performed for $m > N/2$. As each state is

assumed to be double occupied, the first $N/2$ states are occupied and the remaining states are

unoccupied. This means that the perturbing potential only causes a correction to the density when

coupling occupied and unoccupied states. In the case of metals, there is no gap between the occupied

and unoccupied states and so an infinitesimal perturbation can cause a change in the density

functional. This means that modifications to DFPT need to be made to deal with metals.[70,71] Since all of the materials considered in this study have a finite gap, this does not present a problem.

This section is not intended to derive the entirety of the DFPT theory, but give a physical picture of the problem to be solved. The development of the theories and the computational tools to solve them are discussed in much greater detail in ref. 17.

5.3 Macroscopic electric field

In the case of polar materials (for example, the group III-V semiconductors), the long range character of the Coulomb interaction gives rise to a macroscopic electric field with which vibrational waves in the long wavelength limit ($q \to 0$) can couple. The long wavelength acoustic phonons represent lattice vibrations where the atoms in the unit cell move in unison and are thus unaffected by the field. The optic modes, on the other hand, represent vibrations in which the two atoms move in opposite directions to each other. It is these optic phonons that couple with the electric field. The most notable difference between the dispersion curves of a group IV material (for example silicon in Figure 6-2) and those of a group III-V material (for example GaAs in Figure 6-20) is the splitting of the degeneracy of the optic phonons at $\vec{q} = 0$. An explanation of this splitting as well as how the macroscopic field is handled in DFPT is dealt with briefly in the following sections.

5.3.1 Breaking of the optic mode degeneracy

The optic mode splitting can be understood in the following way. The total electronic energy, ε (in its most general quadratic form) in terms of the phonon coordinates, $\vec{u}$ and the electric field $\vec{E}$ can be written as[17]

$$\varepsilon(\vec{u}, \vec{E}) = \frac{1}{2} M \omega_0^2 u^2 - \frac{\Omega}{8\pi} \epsilon_\infty |E|^2 - eZ^* \vec{u} \cdot \vec{E} \qquad \textbf{5.3-1}$$

where M is the nuclear reduced mass, Ω is the unit cell volume, ϵ_∞ is the static dielectric constant, Z^* is the Born effective charge of the ions and ω_0 is the optic frequency in the absence of an electric

field. The Born effective charge is defined later in this section (see equation 5.3-10). The force acting on the ions and the electrical induction are related to the total energy and can be written

$$\vec{F} \equiv -\frac{\partial \varepsilon}{\partial \vec{u}} = -M\omega_0^2 \vec{u} + eZ^* \vec{E} \qquad \text{5.3-2}$$

and

$$\vec{D} \equiv -\frac{4\pi}{\Omega}\frac{\partial \varepsilon}{\partial \vec{E}} = \epsilon_\infty \vec{E} + \frac{4\pi}{\Omega}eZ^* \vec{u} \qquad \text{5.3-3}$$

Using the expression, $\vec{E} = \vec{E}_0 e^{-i(\omega t - \vec{q}\cdot\vec{r})}$, the operator $\vec{\nabla} \to i\vec{q}$ and so in the absence of free charges, Maxwell's equations give

$$\vec{\nabla} \times \vec{E} \sim i\vec{q} \times \vec{E} = 0 \qquad \text{5.3-4}$$

and

$$\vec{\nabla} \cdot \vec{D} \sim i\vec{q} \cdot \vec{D} = 0 \qquad \text{5.3-5}$$

In the case of transverse optic phonons, the electric field is perpendicular to the wavevector and so $\vec{E}_T = 0$, leading to a transverse frequency $\omega_T = \omega_0$ from equation 5.3-2. Thus the transverse phonons are unaffected by the presence of the electric field and their vibrational frequency is unmodified. The longitudinal phonons have their wavevector parallel to the electric field and so from equation 5.3-5, $\vec{D} = 0$ and so equation 5.3-3 can be rewritten as

$$\vec{E} = -\frac{4\pi}{\Omega\epsilon_\infty}eZ^* \vec{u} \qquad \text{5.3-6}$$

Substituting this into equation 5.3-2 and using $\vec{F} = -M\omega_L^2 \vec{u}$,

$$\omega_L = \sqrt{\omega_0^2 + \frac{4\pi e^2 Z^{*2}}{\Omega\epsilon_\infty M}} \qquad \text{5.3-7}$$

The longitudinal frequency is modified by an amount dependent on the dielectric constant and the Born effective charges. The degeneracy originally present in the optic modes has thus been lifted in the presence of the electric field.

5.3.2   Macroscopic electric field in DFPT

The macroscopic field is not straightforward to deal with in the DFPT framework since the electrostatic potential, $V_{\vec{E}}(\vec{r}) = e\vec{E} \cdot \vec{r}$, is not compatible with the lattice periodicity imposed upon the wavefunctions.   This means that the matrix elements of the electrostatic potential between wavefunctions satisfying Born-von-Kármán boundary conditions are ill-defined. The matrix element of the position operator between the unperturbed wavefunction can be recast in terms of the commutator between the Hamiltonian and the position operator, $[H_{SCF}, \vec{r}]$.

$$\langle \psi_m | \vec{r} | \psi_n \rangle = \frac{\langle \psi_m | [H_{SCF}, \vec{r}] | \psi_n \rangle}{\epsilon_m - \epsilon_n}, \qquad \forall m \neq n \qquad \textbf{5.3-8}$$

This is a lattice-periodic operator and so the matrix elements are well-defined. The electronic response is to a screened electric field, $\vec{E} = \vec{E}_0 + 4\pi\vec{P}$, where $\vec{P}$ is the electronic polarization induced by the screened field. A set of self-consistent equations can be generated[17] using equation 5.3-8 which ultimately leads to the calculation of $\vec{P}$.

The Born effective charges and the static dielectric constant are defined in terms of the electric polarization calculated within DFPT, which can be written[17]

$$\vec{P} = \frac{1}{\Omega} \sum_{\kappa} e Z_{\kappa}^{*} \vec{u}_{\kappa} + \frac{\epsilon_{\infty} - 1}{4\pi} \vec{E} \qquad \textbf{5.3-9}$$

Evaluating the differential of $\vec{P}$ with respect to the atomic displacements and the electric field yields

$$eZ_{\kappa}^{*\alpha\beta} = \Omega \left. \frac{\partial P_{\alpha}}{\partial u_{\kappa}^{\beta}(\vec{q} = 0)} \right|_{\vec{E}=0} \qquad \textbf{5.3-10}$$

and

$$\epsilon_{\infty}^{\alpha\beta} = \delta_{\alpha\beta} + 4\pi \left. \frac{\partial P_{\alpha}}{\partial E_{\beta}} \right|_{u_l(\vec{q}=0)=0} \qquad \textbf{5.3-11}$$

The calculation of these terms is necessary in calculating the dynamical matrix. In the long-wavelength limit, the dynamical matrix can be split into an analytic and a non-analytic part,[72,73]

where the analytic part is calculated from the linear response to a zone-center phonon in the absence

of an electric field (as in the case of a non-polar material). The non-analytic part can be written as[73]

$$D_{\alpha\beta}^{na}(\kappa\kappa'; \vec{q}) = \frac{4\pi}{\Omega} e^2 \frac{(\vec{q} \cdot \vec{Z}_\kappa^*)_\alpha (\vec{q} \cdot \vec{Z}_{\kappa'}^*)_\beta}{\vec{q} \cdot \vec{\epsilon}_\infty \cdot \vec{q}} \qquad \textbf{5.3-12}$$

The important point is that the constituent parts of equation 5.3-12 are all available from DFPT by

means of the calculation of the electronic polarization. The dynamical matrix for a polar material can

thus be calculated in the same way as that for a non-polar material with the addition of the non-

analytic part to the dynamical matrix in the long-wavelength limit.

The method outlined above using the electronic linear-response is equivalent to the Berry's phase

approach.[74,75]

5.4   Plane wave basis set

Due to the periodicity of a bulk crystal, the electronic wavefunctions can be expanded in a set of

plane waves. In principle an infinite set of plane waves are required to fully expand a wavefunction

with wavevector, $\vec{k}$. The plane waves with small kinetic energies are usually the most important

terms, however, and so the expansion can be truncated at some cut-off energy, E_{cut}, enabling

calculations to be performed with a finite basis.

There are several advantages to a plane wave basis. Firstly, it is a simple matter to ensure that

E_{cut} (and hence the number of plane waves) is sufficiently large by performing calculations with

increasing E_{cut} until a convergence in the results is seen (for an example of this convergence, see

section 6.2.4). The plane waves are orthonormal by construction and they do not require the

calculation of "Pulay"[69] terms in energy derivatives. As previously mentioned, this means that the

Hellman-Feynman[67,68] expression for the interatomic forces is valid.

The major problem with the use of plane waves is that the core electrons require a very large

number of plane waves to describe them. This is a result of the large number of nodes in the

wavefunctions of these electrons. In order to make computation practicable, the number of plane

waves needs to be kept as small as possible and so plane waves are usually used in conjunction with pseudopotential theory.

5.5   Pseudopotential theory

While it is possible to expand the wavefunctions in terms of a truncated set of plane waves, this is not a good method of describing the tightly bound core orbitals or the rapidly oscillating valence wavefunctions in the core region. In order to accurately describe these particular wavefunctions, a very large set of plane waves is required which increases significantly the computational workload required to calculate the ground state density. A solution to this problem is to replace the core electrons and the strong ionic potential by a weaker pseudopotential acting on a set of pseudo-wavefunctions. The goal in constructing pseudopotentials is to recreate the scattering properties of the ions and core electrons but with wavefunctions that are nodeless and as smooth as possible in the core region. A wavefunction that correctly accounts for scattering inside a core radius, R_C and is identical to the full potential outside this radius is termed "norm-conserving".

The pseudopotential seeks to recreate the scattering of the *valence* electrons by the core region with a weak, nodeless core potential. The scattering properties of the core region are essentially determined by a phase shift, ϕ. Modifying the potential within the core region changes the scattering properties of the valence electrons through the phase shift. Thus, if the core potential is systematically weakened, the phase shift will slowly decrease. A change of π, however, will leave the scattering properties of the valence electrons unchanged. Therefore, there exists a set of pseudopotentials for which the scattering phase shift is unchanged (to within an integer number of π) as compared with the true core potential. Any one of these pseudopotentials can be used to replace the core potential.

In order to maximize the consistency of the results in this dissertation, all ab initio calculations are performed using pseudopotentials generated by Bachelet, Hamann and Schlüter[76]. These

pseudopotentials will be referred to as BHS pseudopotentials and their construction is briefly discussed below.

The BHS pseudopotentials were derived through full-core atom calculations and are cast in a non-local form, i.e. each angular momentum component of the valence pseudo-wavefunction feels a different potential arising from different core states. Relativistic effects are accounted for using Dirac's formulation of the kinetic energy[77] and are included in such a way that the pseudopotentials can still be used in non-relativistic formulations.

In order to ensure that the pseudopotentials have maximum transferability, i.e. that the pseudopotential for a particular atomic species is valid regardless of the local environment, the following criterion[76,78] related to the Friedel sum rule is adhered to,

$$-2\pi \left[(r\phi)^2 \frac{d}{d\epsilon} \frac{d}{dr} \ln\phi \right]_R = 4\pi \int\limits_0^R \phi^2 r^2 dr \tag{5.5-1}$$

where ϕ is the solution to the radial Schrödinger equation at energy ϵ. If there exist two potentials, V_1 and V_2 whose solutions to the radial Schrödinger equation are ϕ_1 and ϕ_2 at energy ϵ, which have the same integrated charge density within the core radius (and $\phi_1(R_C) = \phi_2(R_C)$), then the linear energy variation around ϵ of their scattering phase shifts (at R_C) is identical.

BHS[76] pseudopotentials exist for all elements from H to Pu and so they are easy to implement in all ab initio calculations performed in this study.

5.6 Harmonic IFCs

The reciprocal space harmonic IFCs are defined as the second derivative of the electron ground state energy with respect to the atomic displacements

$$\Phi_{\alpha\beta}(\vec{q}\kappa, \vec{q}'\kappa') = \left. \frac{\partial^2 E_{tot}}{\partial u_\kappa^\alpha(\vec{q}) \partial u_{\kappa'}^\beta(\vec{q}')} \right|_{\{\bar{u}=0\}} \tag{5.6-1}$$

It is computationally more convenient to calculate the IFCs on a reciprocal space grid and determine the real space IFCs by Fourier transform

$$\Phi_{\alpha\beta}(0\kappa, l'\kappa') = \frac{1}{N}\sum_{\vec{q}} e^{i\vec{q}\cdot\vec{R}}\Phi_{\alpha\beta}(\vec{q}\kappa, \vec{q}'\kappa')$$

<div align="right">5.6-2</div>

where N is the number of unit cells in the crystal. Typically, the IFC matrix is split into two parts: an ionic part which is the second derivative of an Ewald sum and an electronic contribution. In calculating phonon frequencies and eigenvectors, reciprocal space dynamical matrices can be constructed *at any wave vector* by Fourier transforming the real space IFCs back into reciprocal space. Thus, the matrices are not limited to calculation on points on the original reciprocal space grid. These dynamical matrices are then diagonalized to yield the eigenfrequencies and eigenvectors, as shown in equation 3.3-7.

The density of the grid on which the reciprocal space IFCs are calculated depends on the range of the forces. The denser the reciprocal space grid, the further the real space IFCs will extend. The shorter-ranged the forces, the coarser the reciprocal space grid can be. When considering polar materials, the real space IFCs are long-ranged in all directions, often leading to a requirement for a finer reciprocal space grid.

5.7 Anharmonic IFCs[17,19]

The third-order anharmonic IFCs are defined as the third derivative of the total energy,

$$\Phi_{\alpha\beta\gamma}(\vec{q}\kappa, \vec{q}'\kappa', \vec{q}''\kappa'') = \frac{\partial^3 E_{tot}}{\partial u_\kappa^\alpha(\vec{q})\partial u_{\kappa'}^\beta(\vec{q}')\partial u_{\kappa''}^\gamma(\vec{q}'')}\bigg|_{\{\vec{u}=0\}}$$

<div align="right">5.7-1</div>

The goal is to be able to calculate this term using variables that are readily available to first-order perturbation theory. This is possible via the "2n+1" theorem that was first proved in the context of DFT by Gonze and Vigneron.[18] A proof of the theorem is not give here, but the third-derivative of the total energy due to a one-dimensional perturbation can be written as

$$E^{(3)} = \sum_\alpha \left(\left\langle \psi_\alpha^{(1)} | v_{ext}^{(2)} | \psi_\alpha^{(0)} \right\rangle + \left\langle \psi_\alpha^{(1)} | H^{(1)} - \varepsilon_\alpha^{(1)} | \psi_\alpha^{(1)} \right\rangle + \left\langle \psi_\alpha^{(0)} | v_{ext}^{(3)} | \psi_\alpha^{(0)} \right\rangle + \left\langle \psi_\alpha^{(0)} | v_{ext}^{(2)} | \psi_\alpha^{(1)} \right\rangle \right)$$

<div align="right">5.7-2</div>

$$+ \frac{1}{6}\int\int\int d\vec{r}d\vec{r}'d\vec{r}'' \frac{\delta^3 E_I[n^{(0)}]}{\delta n(\vec{r})\delta n(\vec{r}')\delta n(\vec{r}'')} n^{(1)}(\vec{r})n^{(1)}(\vec{r}')n^{(1)}(\vec{r}'')$$

where the superscripts refer to the (n[th]) derivative, ε_α are the Kohn-Sham eigenvalues and v_{ext} is the external potential. In order to calculate the anharmonic IFCs, 5.7-2 needs to be generalized to the case of a three-dimensional perturbation (i.e. the perturbation due to the three atomic displacements). According to Gonze and Vigneron[18], for multiple perturbations, the following is defined,

$$E^{\lambda_1^i \lambda_2^j \lambda_3^k} = \frac{1}{(i+j+k)!} \frac{\partial^{i+j+k} E}{\partial^i \lambda_1 \partial^j \lambda_2 \partial^k \lambda_3}\bigg|_{\lambda_1 = 0, \lambda_2 = 0, \lambda_3 = 0}$$

5.7-3

which means that the third-order derivative of the total energy generalizes as

$$E^{\lambda_1 \lambda_2 \lambda_3} = \frac{1}{6} \left(\tilde{E}^{\lambda_1 \lambda_2 \lambda_3} + \tilde{E}^{\lambda_2 \lambda_1 \lambda_3} + \tilde{E}^{\lambda_1 \lambda_3 \lambda_2} + \tilde{E}^{\lambda_3 \lambda_1 \lambda_2} + \tilde{E}^{\lambda_3 \lambda_2 \lambda_1} + \tilde{E}^{\lambda_2 \lambda_3 \lambda_1} \right)$$

5.7-4

with

$$\tilde{E}^{\lambda_1 \lambda_2 \lambda_3} = \sum_\alpha \left(\left\langle \psi_\alpha^{\lambda_1} \middle| v_{ext}^{\lambda_2 \lambda_3} \middle| \psi_\alpha^{(0)} \right\rangle + \left\langle \psi_\alpha^{\lambda_1} \middle| H^{\lambda_2} - \varepsilon_\alpha^{\lambda_2} \middle| \psi_\alpha^{\lambda_3} \right\rangle + \left\langle \psi_\alpha^{(0)} \middle| v_{ext}^{\lambda_1 \lambda_2 \lambda_3} \middle| \psi_\alpha^{(0)} \right\rangle \right.$$

$$+ \left\langle \psi_\alpha^{(0)} \middle| v_{ext}^{\lambda_1 \lambda_2} \middle| \psi_\alpha^{\lambda_3} \right\rangle \right)$$

5.7-5

$$+ \frac{1}{6} \int \int \int d\vec{r} d\vec{r}' d\vec{r}'' \frac{\delta^3 E_I[n^{(0)}]}{\delta n(\vec{r}) \delta n(\vec{r}') \delta n(\vec{r}'')} n^{\lambda_1}(\vec{r}) n^{\lambda_2}(\vec{r}') n^{\lambda_3}(\vec{r}'')$$

The purpose of explicitly writing out 5.7-5 is to demonstrate that only first-order corrections to the electron density functional and one-electron wavefunctions are required to evaluate the third-derivative of the total energy.

As in the case of the harmonic IFCs, it is computationally preferable to calculate the third-order anharmonic IFCs in reciprocal space and then use the relation

$$\Phi_{\alpha\beta\gamma}(\vec{q}\kappa, \vec{q}'\kappa', \vec{q}''\kappa'') = \sum_{ll'} \Phi_{\alpha\beta\gamma}(0\kappa, l'\kappa', l''\kappa'') e^{i\vec{q}' \cdot \vec{x}'(l')} e^{i\vec{q}'' \cdot \vec{x}(l'')}$$

5.7-6

to determine the real-space IFCs. A $4 \times 4 \times 4$ mesh is used for the two vectors, $\vec{q}'$ and $\vec{q}''$ and the third vector is determined by $\vec{q} + \vec{q}' + \vec{q}'' = 0$. This mesh leads to the calculation of forty-two $\vec{q}$-pair anharmonic IFC tensors in reciprocal space. From these reciprocal space IFCs, the real-space IFCs are recovered. Instead of performing a direct Fourier-transformation, the real space IFCs are calculated via the solution of a set of linear differential equations. The calculations result in real

space IFCs including atomic triplets out to seventh nearest neighbors.   The Fortran program used for performing these calculations was developed by D. Strauch's group at the University of Regensburg[19,79].

All other DFPT calculations are performed using the Quantum-Espresso package.[80]

6 Ab initio calculations of lattice thermal conductivity

The results of chapter 4 emphasize the importance of accurately modeling the phonon dispersions and the anharmonicity of the crystal potential. The major drawback, however, of employing an approach using *any* empirical interatomic potential, regardless of how well it reproduces measured values, is the lack of predictive power in the approach and the limitation of studying materials for which parameter sets can be determined.

A satisfying solution to this problem is the use of the density functional theory (DFT) of Kohn and Sham[61] extended to calculate linear response in the density functional perturbation theory[81-83] (DFPT). This method allows calculation of both the harmonic and the anharmonic IFCs from first-principles. DFPT and the associated pseudopotential theory are discussed in chapter 5. The power of this approach lies in the lack of adjustable parameters and consequently, the requirement of comparison with experimental data in order to calculate κ_L is removed. In fact, the only required inputs are the harmonic and third-order anharmonic IFCs, a pseudopotential with a cut-off energy, E_{cut} to determine the plane wave basis as well as the mass-variance parameter, g_2, if isotopic impurities are being considered. The pseudopotentials themselves are derived from all electron calculations and so require no comparison with measured data in their generation. The cut-off energy, E_{cut} is determined from the convergence in the linear thermal expansion coefficients (discussed in section 6.2.4).

Within this study, phonon dispersions curves, mode Grüneisen parameters, the linear thermal expansion coefficients and the lattice thermal conductivities (with and without isotopic impurity scattering) are calculated in a consistent manner for several diamond and zinc-blende structured materials *without any adjustable parameters*.

The calculations for the studied group IV and III-V materials are discussed in the following sections and build on work first demonstrated in ref. 84.

6.1   Group IV materials

The procedure adopted for modeling the different material parameters is common to all the considered materials. The harmonic and third-order anharmonic IFCs are calculated using BHS pseudopotetials[76] in the LDA formalism. The harmonic IFCs are calculated on a $6 \times 6 \times 6$ Monkhorst-Pack k-point mesh and the third-order anharmonic IFCs are calculated on a $4 \times 4 \times 4$ k-point mesh. The lattice constants are determined from the minimum in the electronic ground state energy and the cut-off energies, E_{cut} are determined from the convergence in the linear thermal expansion coefficients. Table 6-1 lists the lattice constants and cut-off energies used for the group IV materials studied. Included in parentheses are the experimentally determined lattice constants[29].

	Lattice constant (Bohr)	Cut-off energy, E_{cut}
Si	10.150 (10.267)	80Ry
Ge	10.520 (10.696)	35Ry
Diamond	6.675 (6.743)	100Ry

Table 6-1; The calculated lattice constants and cut-off energies for the studied group IV materials. Included in parenthesis are the experimentally measured[29] lattice constants.

As a result of the commonality of the approach, the calculations are presented and discussed in depth for silicon and then the other materials are afforded little discussion. The unusual nature of diamond, however, necessitates further individual discussion.

The DFPT calculations are essentially zero temperature calculations. This means that all comparisons with finite temperature measurements will have some error associated with them. At room temperature, crystals tend to expand with increasing temperature and so zero temperature lattice constants will necessarily be different to finite temperature ones. The lattice constant is a fundamental parameter that then feeds into all other calculations. The effects of this problem are initially discussed in section 6.2.1 and recur throughout the discussion of silicon.

6.2 Silicon

Several parameters need to be calculated as well as some convergence tests performed, prior to calculation of κ_L. The procedure adopted for the calculation of κ_L is

1. Calculate the lattice constant by minimizing the ground state energy.

2. Calculate the harmonic and third-order anharmonic IFCs for a range of cut-off energies.

3. Calculate the Grüneisen parameters and find convergence in the linear thermal expansion coefficients with increasing E_{cut}.

4. Calculate the three-phonon phase space and hence calculate κ_L.

The computational bottle-neck is the calculation of the three-phonon phase space. For silicon, this step, with the IFC meshes stated in section 6.1 and the Gaussian grids stated in section 3.11.1, takes several processor months. Each of the procedural steps is treated separately in the following sections.

6.2.1   Lattice constant

The first step in the calculation of κ_L is the determination of the lattice constant. This is achieved by calculating the electronic ground state energy of bulk silicon for a range of lattice constants and finding the minimum in the ground state energy curves. The calculation of the lattice constants also gives an initial indication of the required cut-off energy, E_{cut}. For cut-off energies that lead to a basis with an insufficient number of plane-waves to describe the electronic wavefunctions, some fluctuation can be observed in the curve of ground state energy versus lattice constant. A smooth curve and a converged minimum value of the ground-state energy give a good initial indication of the required value of E_{cut}. As previously remarked, the actual value of E_{cut} used in this work is determined by finding convergence in the linear thermal expansion coefficients. The variation of the electronic ground state energy with lattice constant for 25Ry (solid curve), 35Ry (long-dashed curve), 45Ry (short-dashed curve) and 60Ry (dashed-dotted curve) is shown in Figure 6-1.
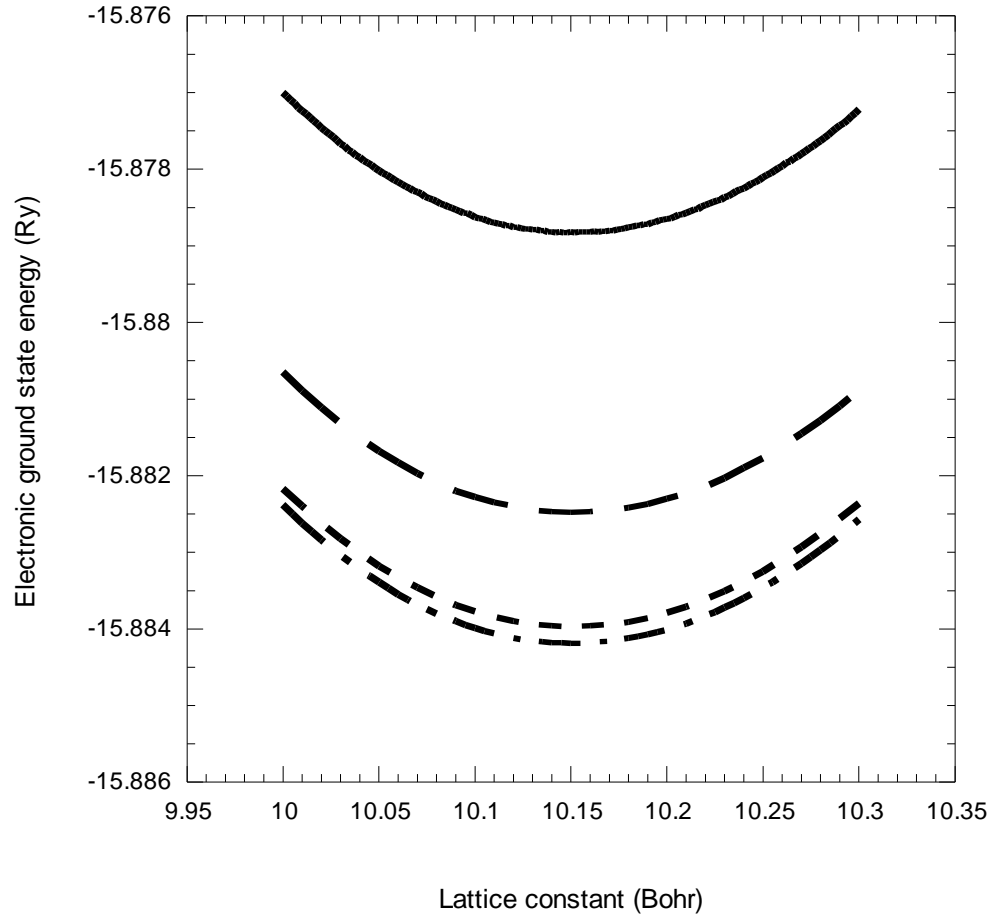
Figure 6-1; Variation of the electronic ground state energy with lattice constant for silicon with cut-off energies of 25Ry (solid curve), 35Ry (long-dashed curve), 45Ry (short-dashed curve) and 60Ry (dashed–dotted curve).

Convergence in the minimum of the electronic ground state energy, E_0 is achieved at 60Ry (the 50Ry curve is omitted from Figure 6-1 as it obscures the 60Ry curve). The difference in E_0 for cut-off energies of 50Ry and 60Ry is approximately 7×10^{-5}Ry (less than 0.0005%) and between 25Ry and 60Ry is only 0.03%. The lattice constant corresponding to E_0 is 10.15 Bohr, which is less than the measured value at 300K. Since it is known that the LDA formalism leads to "overbinding"[17] and that the DFPT calculations are 0K calculations, a lattice constant that is smaller than measured values is expected. The effects of using different lattice constants is investigated further in section 6.2.3.

6.2.2   Phonon dispersions

With the lattice constant determined, the phonon dispersion curves can be calculated. The remarkable accuracy of ab initio plane-wave pseudopotential calculations within the LDA formalism at calculating lattice dynamical properties of semiconductors is well documented[15,16]. In Figure 6-2 the calculated 0K phonon dispersions of silicon using an E_{cut} of 35Ry (solid curves) and 80Ry (dashed curves) are compared with 300K measurements[37] (open diamonds).
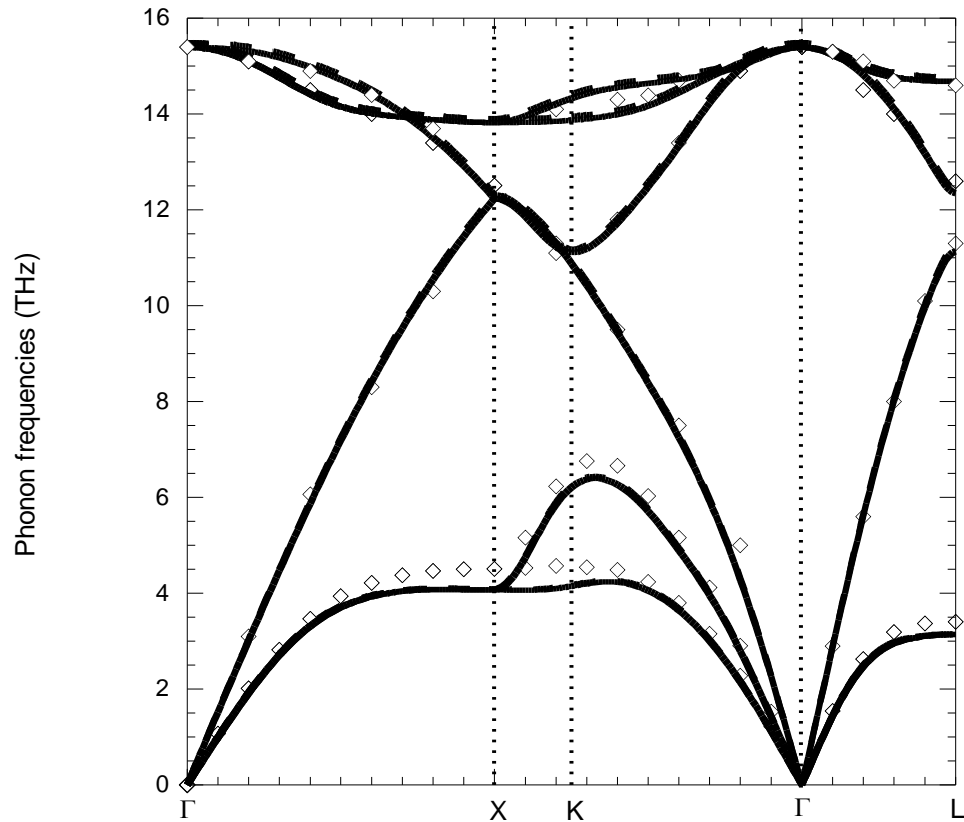

Figure 6-2; Phonon dispersion curves of silicon along high symmetry directions for cut-off energies of 35Ry (solid curves) and 80Ry (dashed curves). The measured values[37] are indicated by open diamonds.

Figure 6-2 demonstrates that the DFPT method with a sufficiently high value of E_{cut} gives a good fit to the measured data for all branches over most of the Brillouin zone. The important acoustic

branches, however, are below the measured data away from the zone center. Reducing E_{cut} to 35Ry has no noticeable effect on the phonon dispersions.

Previous studies of silicon have produced closer fits to the measured phonon dispersions than the calculations shown here. The main cause of these discrepancies is the value of the lattice constant. In Figure 6-3, the phonon dispersion curves of silicon with a lattice constant of 10.15 Bohr (solid curve) is compared to those calculated with the room temperature lattice constant of 10.2665 Bohr (dashed curve) and the experimentally measured values[37] (open diamonds).
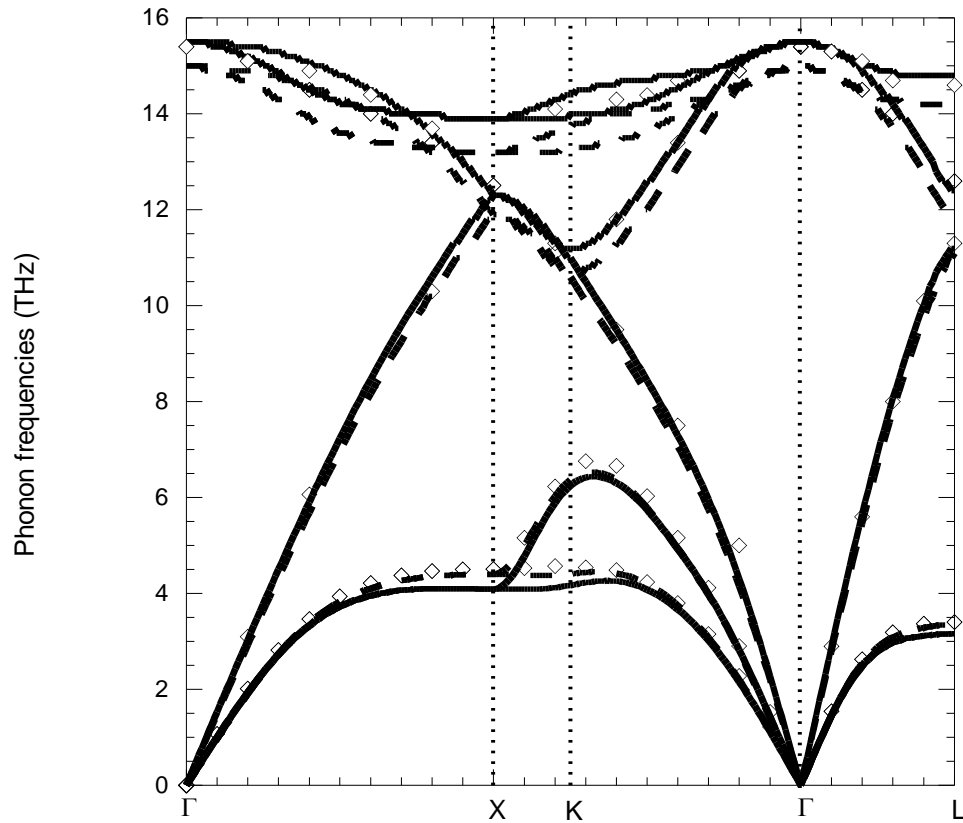
Figure 6-3; Phonon dispersion curves of silicon with a lattice constant of 10.15 Bohr (solid curves), 10.2665 Bohr (dashed curves) and the experimentally measured values[37] (open diamonds).

Clearly, increasing the lattice constant significantly improves the agreement with the experimentally measured acoustic modes. The optic modes are not quite as well represented, however. Different pseudopotentials can also give rise to a better determination of the lattice constant and hence better fits to the measured data. This fact is well known in the literature (ref. 85, for example). The goal of this study, however, is to demonstrate the predictive capability of the ab initio BTE method. As such, the BHS pseudopotentials were used for all harmonic and anharmonic IFCs and the lattice constants used are those predicted by these pseudopotentials. The effect of increasing the lattice constant is also discussed in the following sections on the mode Grüneisen parameters, linear thermal expansion coefficient and the thermal conductivity calculations.

6.2.3 Mode Grüneisen parameters

The mode Grüneisen parameters can be calculated in two different ways; one involving the harmonic IFCs only and the second requiring both the harmonic and the third-order anharmonic IFCs (equations 3.12-2 and 3.12-3). The phonon dispersion curves arising from the harmonic IFCs are in extremely good agreement with experimental values (as seen in Figure 6-2) giving confidence in their accuracy. There is no physical property calculated using the anharmonic IFCs as the sole input that can be visually compared with measurement. Comparing the results from the two calculation methods with each other and with measurement provides a visual check of the accuracy of the anharmonic IFCs. This comparison is shown In Figure 6-4 along high symmetry directions. The solid curves show the Grüneisen parameters calculated using harmonic IFCs alone, the open diamonds are for the calculations involving both sets of IFCs and the open squares are measurements.[86]

The agreement between the two calculation methods is extremely good over the entirety of the Brillouin zone. The agreement with the limited experimental values is also extremely good for the optic branches, but the acoustic branches show some deviation. It should be noted that the experimental errors are much larger for the acoustic branches than for the optic branches.
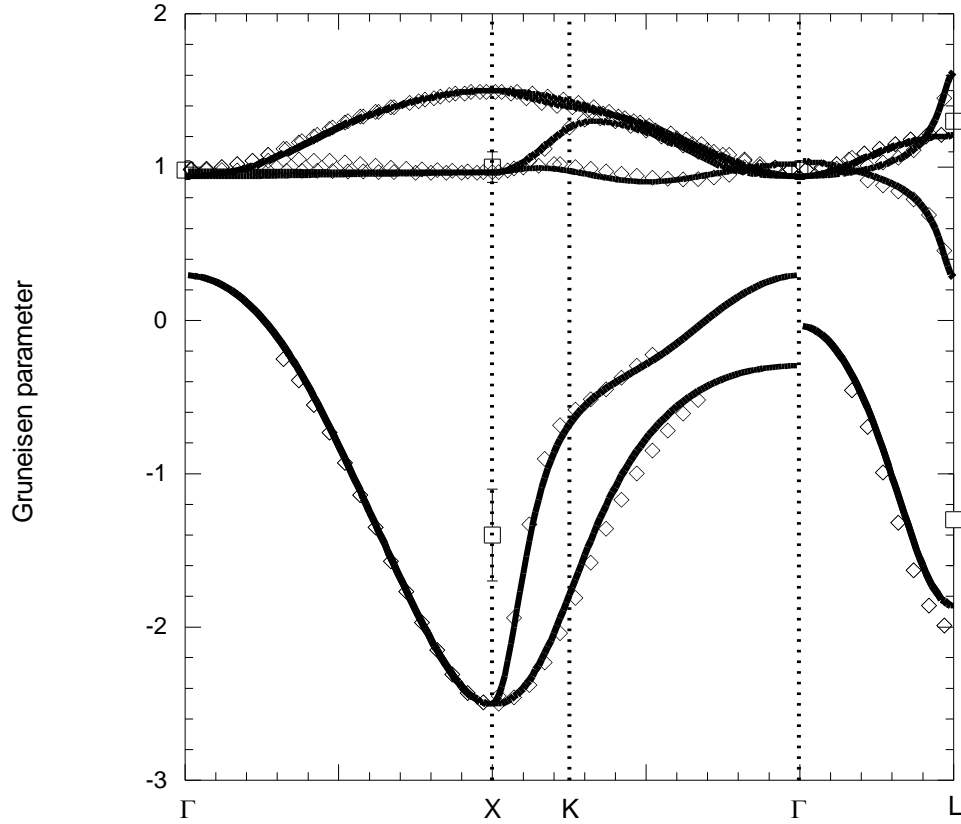
Figure 6-4; Mode Grüneisen parameters calculated with harmonic IFCs (solid curve), harmonic and third-order anharmonic IFCs (open diamonds) and measured values[86] (open squares).

The mode Grüneisen parameters are dependent on the unit cell volume and hence the lattice constant (equation 3.12-1). It is expected that errors in the lattice constant would lead to errors in the microscopic forces and consequently, $\gamma_j(\vec{q})$. To illustrate this point, $\gamma_j(\vec{q})$ for selected branches calculated using equation 3.12-3 and lattice constants of 10.15 Bohr (solid curve), 10.25 Bohr (long-dashed curve) and 10.2665 Bohr (short-dashed curve) and compared with the measured values[86] in Figure 6-5.

The optic branches are essentially unaffected by the change in the lattice constant and agree with the measured values. The acoustic branches, on the other hand, are strongly influenced by the lattice
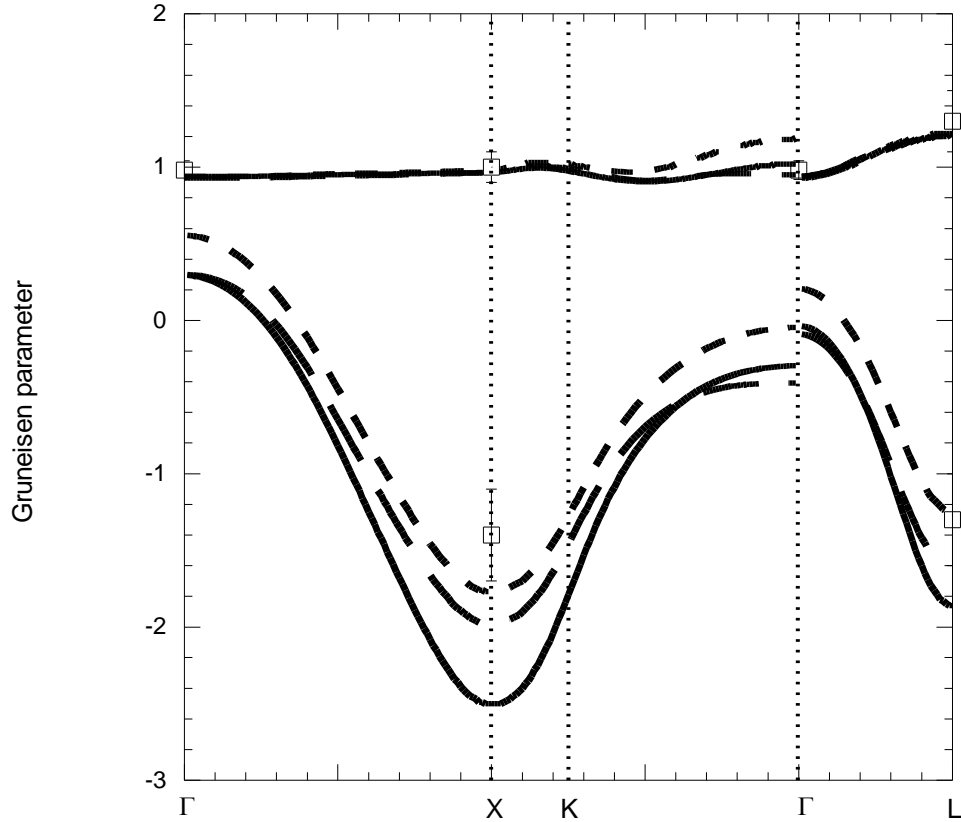
Figure 6-5; Mode Grüneisen parameter for one acoustic and one optic branch in silicon along high symmetry directions in the first Brillouin zone for lattice constants of 10.15 Bohr (solid curve), 10.25 Bohr (long-dashed curve) and 10.2665 Bohr (short-dashed curve). The measured values[86] are included as open squares for comparison.

constant used. With the 300K experimental lattice constant of 10.2665 Bohr, the calculated values of $\gamma_j(\vec{q})$ are much closer to the measurements than the corresponding calculations with smaller lattice constants.

6.2.4   Linear thermal expansion coefficients and cut-off energy

In order to determine E_{cut}, the behavior of the linear thermal expansion coefficients, $\alpha(T)$, is studied. A value of E_{cut} that provides convergence in the ground state energy and accurately describes the phonon dispersion curves is not necessarily large enough to achieve convergence in

$\alpha(T)$. A possible reason for this is the coarser Monkhorst-Pack grid used in the calculation of the anharmonic IFCs. The temperature dependence of $\alpha(T)$ is calculated for a range of different values of E_{cut} until convergence is achieved. Further, $\alpha(T)$ is very sensitive to the anharmonicity of the crystal and the lattice constant, so comparison with experimentally measured values helps determine the accuracy with which the crystal anharmonicity is captured by the model. The variation of $\alpha(T)$ with temperature for E_{cut} values of 25Ry (solid curve), 35Ry (long-dashed curve), 45Ry (short-dashed curve), 80Ry (dashed-dotted curve) and 90Ry (open diamonds) are compared with experimental measurements[87] (open squares) in Figure 6-6.

The linear thermal expansion coefficients calculated with $E_{cut} = 90$Ry has a subset of its values shown with open diamonds in Figure 6-6 in order to easily distinguish them from the dashed-dotted curve of $E_{cut} = 80$Ry. Figure 6-6 demonstrates that convergence in $\alpha(T)$ is achieved with a value of 80Ry for E_{cut} and so this value is adopted for the remainder of the calculations. The value of E_{cut} in the literature for similar calculations is often smaller than the value used here. There are two possible reasons for this. Firstly, the harmonic calculations (e.g. the calculation of phonon dispersion curves) do not require this high of a value. It is the calculations of the anharmonic IFCs that drive the value of E_{cut}. Secondly, recent works often make use of ultrasoft pseudopotentials to describe the core electron wavefunctions. These pseudopotentials have the advantage of creating very smooth wavefunctions inside the core region, thus minimizing the number of plane waves required to describe them. The most time-consuming step in the calculations is the calculation of the three-phonon scattering phase space and so the computational expense of higher cut-off energies is not problematic and the BHS pseudopotentials are used to provide consistency across all materials studied.

The calculated values of $\alpha(T)$ are consistently lower than the measured values over the whole temperature range considered. As previously remarked, the calculated 0K lattice constant is smaller than that experimentally observed (see Table 6-1). It is therefore expected that $\alpha(T)$ will be incorrect at low temperature and the discrepancy will get worse with increasing temperature as the

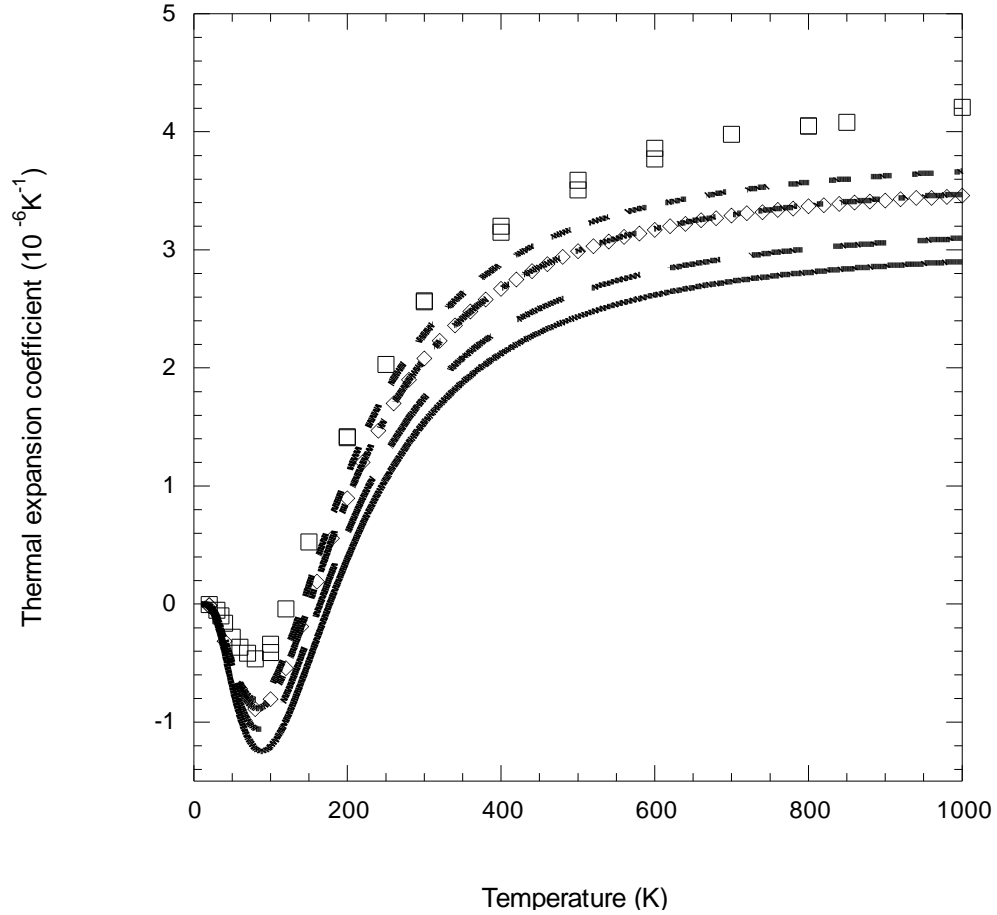crystal lattice expands (ignoring the low temperature contraction). This behavior has already been

Figure 6-6; Linear thermal expansion coefficient as a function of temperature for cut-off energies of 25Ry (solid curve), 35Ry (long-dashed curve), 45Ry (short-dashed curve), 80Ry (dashed-dotted curve), 90Ry (open diamonds) and experimental values[87] (open squares).

observed in diamond[88] and has been addressed by calculating the temperature dependence of the lattice constant by considering the minimum in the Helmholtz free energy[89].

In an attempt to highlight this problem, calculations of $\alpha(T)$ using different lattice constants are performed. For each lattice constant, a new set of IFCs are calculated. In Figure 6-7, $\alpha(T)$ is compared for lattice constants of 10.15 Bohr (solid curve), 10.2 Bohr (long-dashed curve), 10.25

Bohr (short-dashed curve) and the room temperature value of 10.2665 Bohr (dashed-dotted line). The measured[87] values (open squares) are again included for reference.
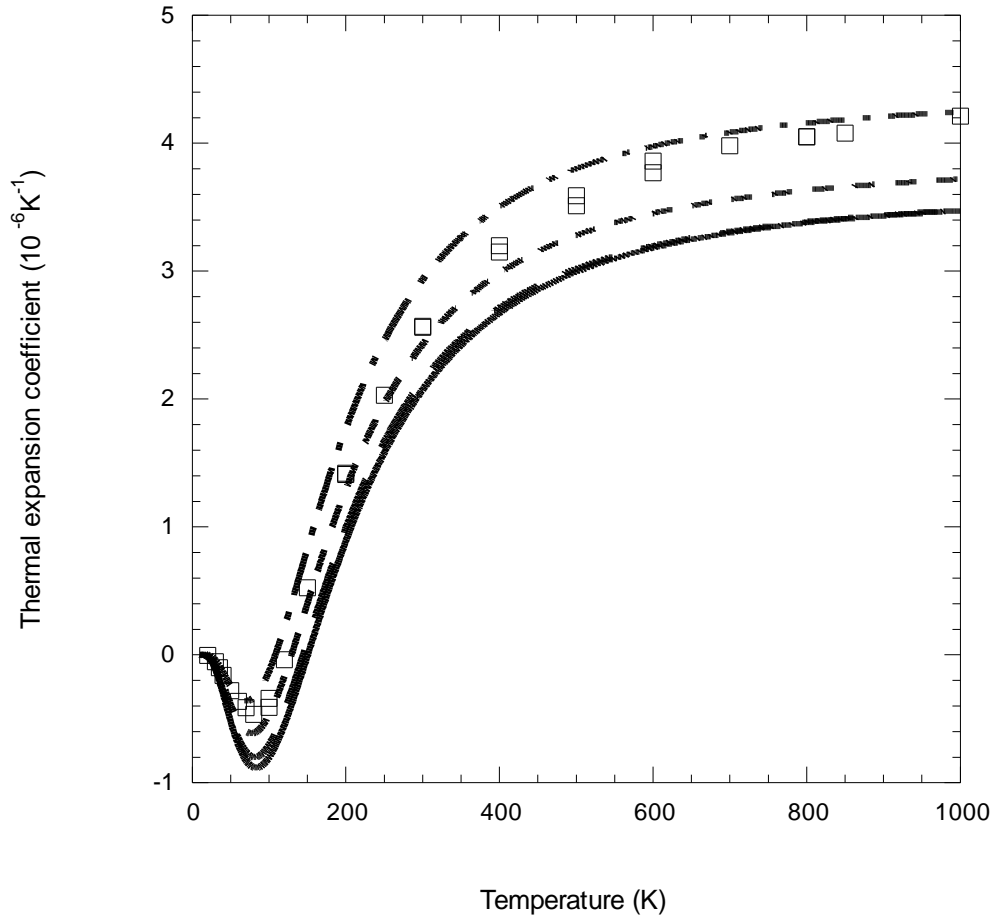

Figure 6-7; $\alpha(T)$ of silicon for lattice constants of 10.15 Bohr (solid curve), 10.2 Bohr (long-dashed curve), 10.25 Bohr (short-dashed curve) and the room temperature value of 10.2665 Bohr (dashed-dotted curve). The experimentally measured values[87] are shown as open squares.

The results for $\alpha(T)$ for a lattice constant of 10.25 Bohr are only slightly below the measured values up to about 300K. Above this value, the calculated values again saturate as the measured values continue to climb. The results for $\alpha(T)$ for the room temperature lattice constant of 10.2665 Bohr are slightly higher than the measured values.

From the results of the previous section, the observed increase in $\alpha(T)$ with the increase in the lattice constant is expected. $\alpha(T)$ is essentially a sum of $\gamma_j(\vec{q})$ weighted by the mode specific heat (equation 3.12-3). From Figure 6-5, it is clear that increasing the lattice constant increases $\gamma_j(\vec{q})$ for the acoustic branches over almost the entire Brillouin zone. Consequently a sum of $\gamma_j(\vec{q})$ must also increase and so the observed increase in $\alpha(T)$ is expected.

A point that should be kept in mind is that the electronic ground state energy of silicon is minimized at a lattice constant of 10.15 Bohr and so errors are introduced into the calculations of $\alpha(T)$ when larger lattice constants are used. It is not obvious how using a lattice constant that is inconsistent with the ground state of the lattice would affect the results. For this reason, the lattice constant calculated to be the ground state lattice constant is used in all calculations, despite the fact that is known to be too small.

Further, a significant goal of this work is to demonstrate the potential of the ab initio method in thermal conductivity *predictions.* In this context, the lattice constant predicted by the ab initio calculations is used. Using the measured lattice constant presupposes experimental measurements and is incompatible with the predictive approach.

6.2.5 Lattice thermal conductivity

The lattice constant and cut-off energy are established through the calculations described in the previous sections. With these values known, the harmonic and anharmonic IFCs are calculated and so all inputs required for calculations of κ_L are available.

Naturally occurring silicon[20] is composed of 92.2% ^{28}Si, 4.7% ^{29}Si and 3.1% ^{30}Si and isotopically enriched silicon is 99.983% ^{28}Si, 0.014% ^{29}Si and 0.003% ^{30}Si. The mass of naturally occurring silicon is taken to be 28.086 and since this is extremely close to the isotopically enriched mass (28.0), all calculations are performed using this value. The mass variance parameter, g_2 for the naturally occurring and isotopically enriched samples are 2.01×10^{-4} and 2.33×10^{-6} respectively. The temperature dependent κ_L of naturally occurring (dashed curve) and isotopically enriched (solid

curve) silicon are compared with experimentally measured values[20] (open squares and diamonds) in Figure 6-8.
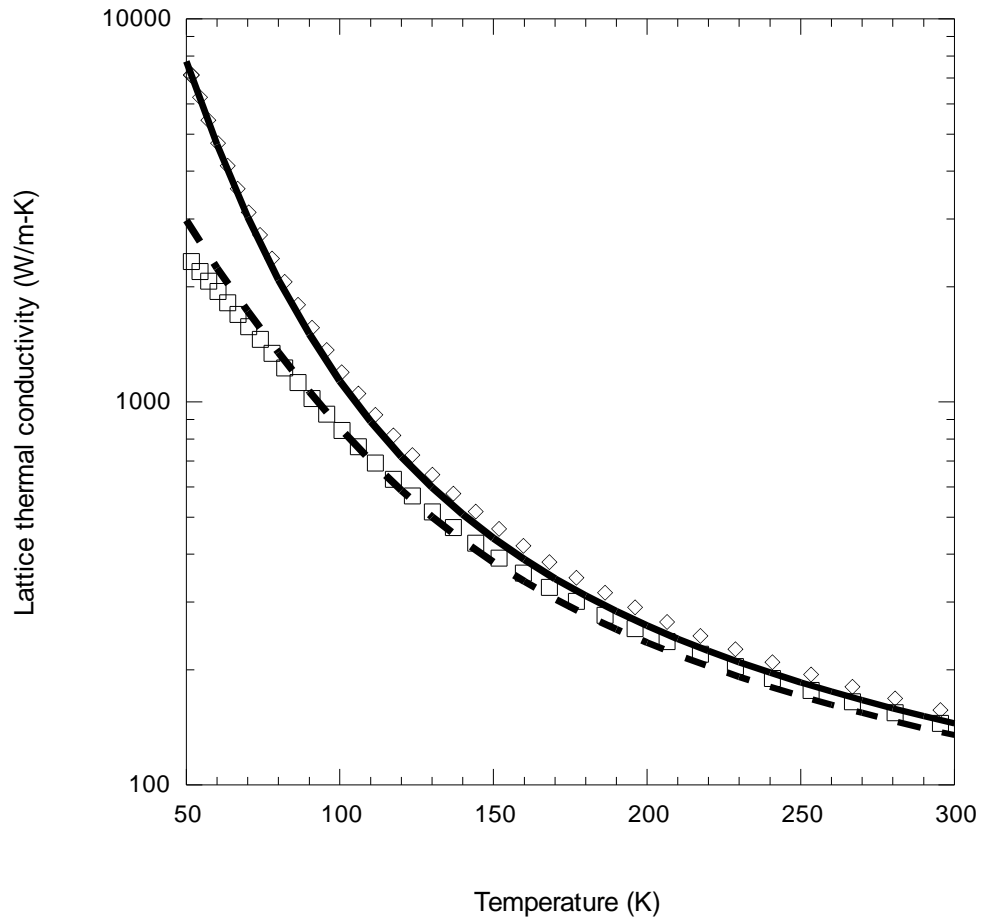

Figure 6-8; Calculated lattice thermal conductivity of naturally occurring (dashed curve) and isotopically enriched (solid curve) silicon compared with the corresponding measured values[20] (open squares and circles).

   The agreement between the ab initio calculations and the measured values is extremely good over the entire temperature range considered. The validity of the calculations at low temperatures where umklapp scattering is no longer the dominant scattering mechanism becomes questionable. For the isotopically enriched sample, the agreement is good all the way down to 50K. The extremely small concentration of isotopic impurities ensures that three-phonon umklapp scattering is still the

dominant scattering mechanism even at these very low temperatures. Ultimately, κ_L for the measured sample will peak and then decrease with decreasing temperature (the peak occurs at approximately 26K), whereas the calculations will diverge to infinity.

For the naturally occurring sample, the calculations and the experimental data begin to separate below approximately 80K. Three-phonon scattering no longer dominates for this sample and so the validity of the calculated results becomes questionable. As the calculations push to lower temperatures, the freezing out of umklapp processes leads to a divergence in the thermal conductivity that cannot be checked by the included impurity scattering terms. As the three-phonon scattering becomes less dominant, the calculated and measured curves must necessarily separate.

The experimental measurements only extend to 300K and so no comparison can be made above this temperature. As the temperature increases, the results for the naturally occurring and enriched silicon converge. This can be understood as the contribution from the isotopic impurities becoming insignificant compared with the three-phonon scattering. It is therefore expected that the two different isotopic compositions would converge at high enough temperatures.

The lattice constant used in the calculations is known to have a marked effect on all of the material parameters so far studied. At 300K, κ_L calculated using a lattice constant of 10.15 Bohr is 145W/m-K. The value calculated using a lattice constant of 10.25 Bohr is 139W/m-K, a drop of 4%.

6.3 Germanium

All of the material properties studied for silicon in section 6.2 are also studied for germanium using the same procedure with one exception. The isotopic composition of germanium is such that the masses of the naturally occurring and isotopically enriched samples are sufficiently different that they need to be accounted for. The lattice constant used for all the germanium calculations is 10.52 Bohr and the cutoff-energy is 35Ry. The phonon dispersion curves for germanium using these parameters are compared with experimentally measured values[90] in Figure 6-9.
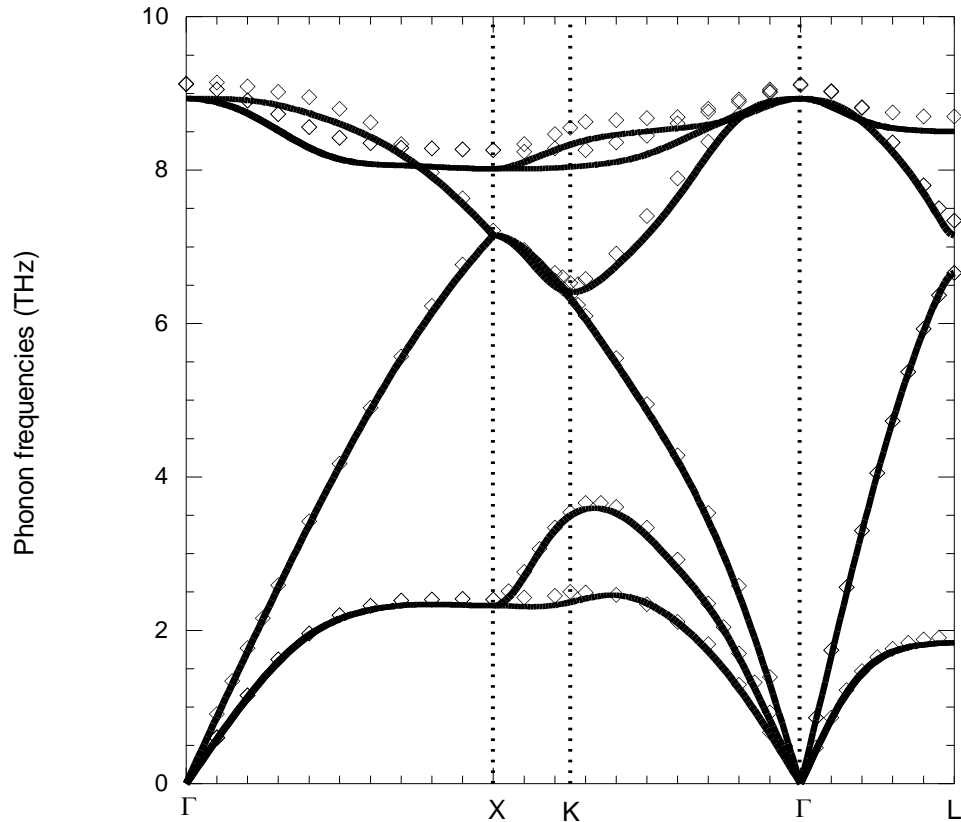
Figure 6-9; Comparison of the calculated (solid curves) and measured[90] (open diamonds) phonon dispersions in germanium.

The agreement between the calculations and the measurements are extremely good for all branches across the whole Brillouin zone. The measurements in Figure 6-9 are for germanium at 80K. Comparison with 300K data would not produce quite as good a fit; a situation that could then be rectified by increasing the lattice constant analogously with silicon.

The calculated $\alpha(T)$ for cut-off energies of 25Ry (solid curve), 45Ry (open squares) and 60Ry (open diamonds) as a function of temperature are compared with experimental values[87] (open circles) in Figure 6-10.

The data for cut-off energies of 45Ry and 60Ry are included in Figure 6-10 as open squares and diamonds respectively so as not to obscure the data as the convergence is much more rapid than for

silicon. The converged cut-off energy is determined to be 35Ry. As with silicon, $\alpha(T)$ is consistently
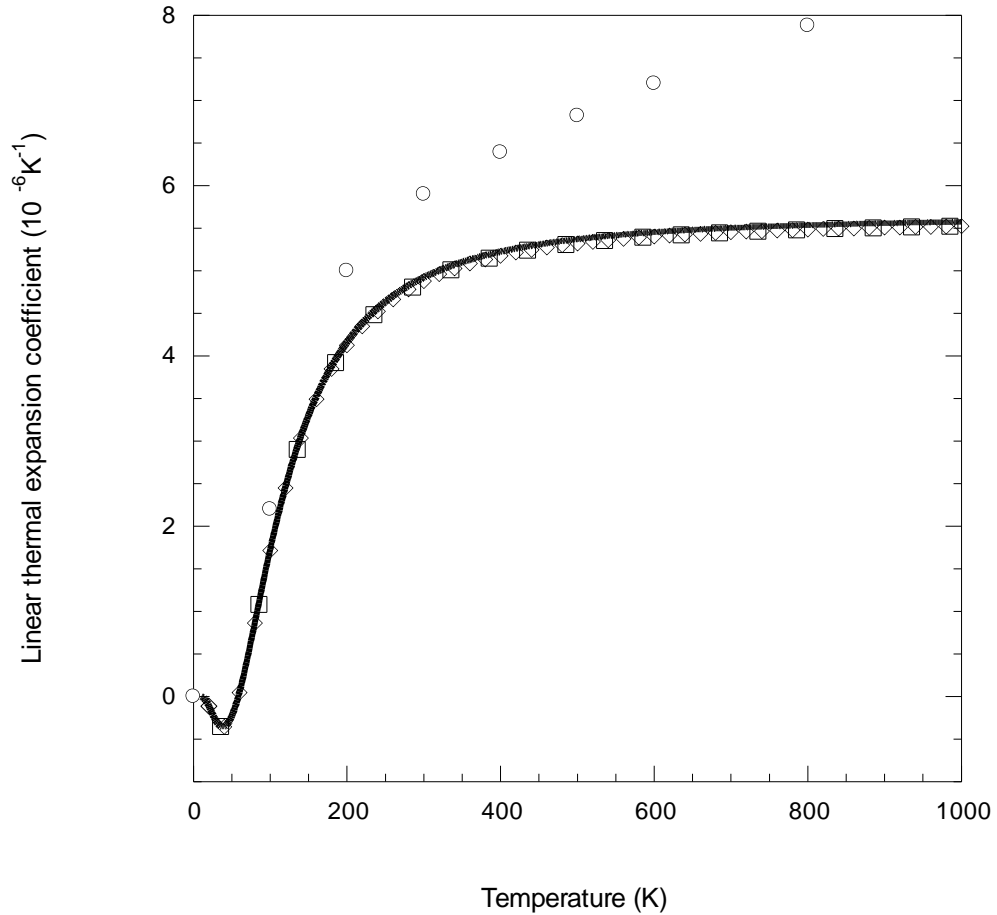

Figure 6-10; Calculated linear thermal expansion coefficient of germanium for cut-off energies of 25Ry (solid curve), 45Ry (open squares) and 60Ry (open diamonds) compared with experimental values[87] (open circles).

smaller than the measured values. The experimental data continues to rise for the whole temperature range shown, whereas the calculations saturate above approximately 400K as a result of the lattice constant being fixed (at a value smaller than the experimentally determined value) for the entire temperature range. This saturation behavior is visible in the silicon case (Figure 6-6), however, it occurs at a higher temperature in line with silicon's higher Debye temperature

97

$(\Theta_D^{Ge} \sim 374K$ and $\Theta_D^{Si} \sim 645K)$. The low temperature comparison is very good, although the number of measured data points is sparse in this region.

The composition of naturally occurring germanium[24] is 20.5% [70]Ge, 27.4 [72]Ge, 7.8% [73]Ge, 36.5% [74]Ge and 7.8% [76]Ge. The mass of naturally occurring germanium is taken to be 72.61; that of isotopically enriched germanium (>99.99% [70]Ge) being 70. The mass enters into the calculation of both the harmonic IFCs and the three-phonon scattering rates. The change in the dispersion curves resulting from the change in the harmonic IFCs is negligible, however, the effect on the scattering rates causes a noticeable change in κ_L. This confirms the requirement to explicitly account for the different average isotopic masses. The mass variance parameter, g_2 has values of 8.162x10^{-8} and 5.889x10^{-4} for isotopically enriched (dashed curve) and naturally occurring[24] (solid curve) samples respectively. The calculated values of κ_L are compared with the measured values[24] in Figure 6-11.

The agreement between the ab initio calculations and experiment is, once more, extremely good. As discussed in section 6.2.5, the two curves converge with increasing temperature. The divergence of the calculated and measured curves at low temperature is not evident in these plots. The maximum in the measured value of κ_L occurs at approximately 16K, much lower than in the silicon case; a direct result of the lower Debye temperature of germanium. This fact ensures that three-phonon scattering is still the dominant mechanism, even at these low temperatures.

The energy scale of germanium is lower than that of silicon; the maximum optical zone center frequencies for germanium and silicon are 8.92 THz and 15.48 THz respectively. As a result of this, at low temperatures, more phonon modes are excited in germanium than in silicon and consequently, three-phonon scattering is more likely to impede thermal transport. Combined with germanium's smaller acoustic velocities, this helps to explain the lower values of κ_L in germanium.
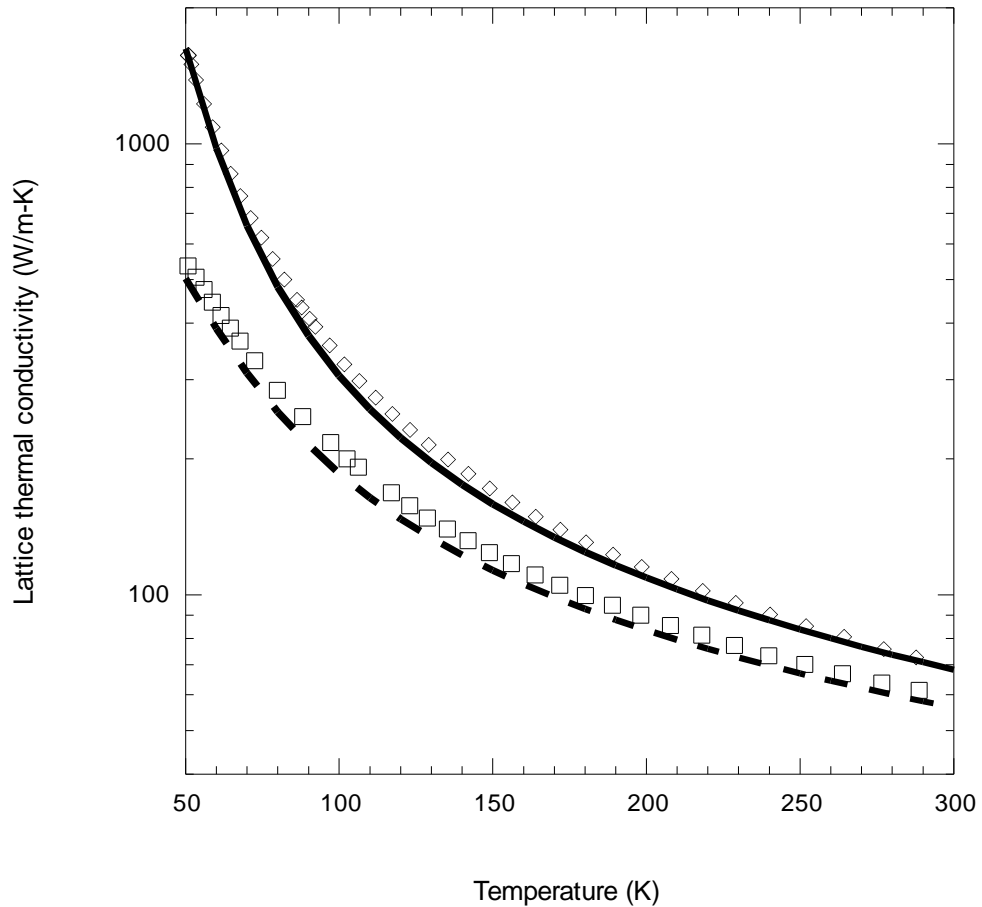
Figure 6-11; Lattice thermal conductivity calculations of naturally occurring (dashed curve) and isotopically enriched (solid curve) germanium compared with measured values[24] (open squares and diamonds).

6.4 Diamond

Diamond is an unusual material, whose lattice thermal conductivity is extremely large compared to the other group IV materials. This is due, in part, to the large acoustic velocities in diamond as compared to the other group IV materials. The flattening of the transverse acoustic (TA) modes that is typical of these materials is not observed in diamond as can be seen from the phonon dispersion calculations (solid curves) and experimental results[91] (open diamonds) in Figure 6-12.
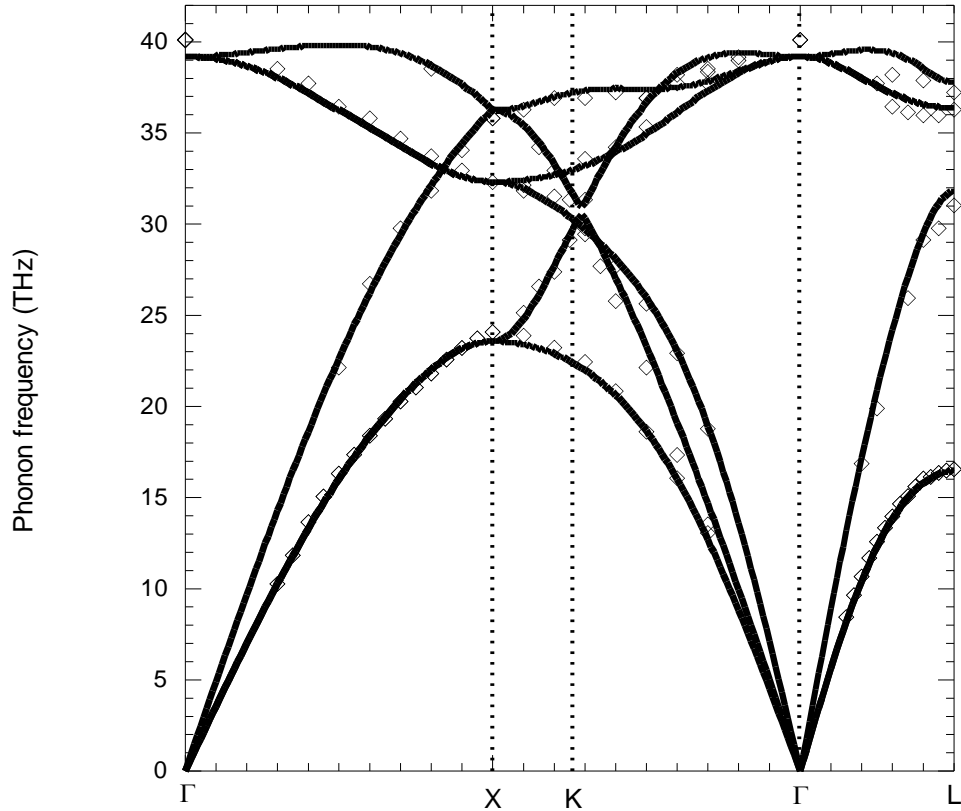
Figure 6-12; Phonon dispersion curves of diamond along high symmetry directions for a cut-off energy of 100Ry (solid curves). The measured values[91] are indicated by open diamonds.

The calculated transverse acoustic (TA) and longitudinal acoustic (LA) velocities as well as the maximum optical zone-center frequencies for silicon, germanium and diamond are listed in Table 6-2. The measured velocities are shown in parentheses.

	v_{TA} **(m/s)**	v_{LA} **(m/s)**	$\omega_{max}^{optical}$ **(THz)**
Si	5413 (5843)[92]	8216 (8420)[92]	15.48
Ge	3251 (3542)[93]	4844 (4914)[93]	8.92
Diamond	12567 (12830)[94]	17326 (17520)[29]	39.17

Table 6-2; The transverse acoustic (TA) and longitudinal acoustic (LA) velocities and maximum zone-center optical frequencies for Si, Ge and diamond.

The diamond structure materials all have four electrons in the outer shell (e.g. $2s^2\,2p^2$ in diamond and $3s^2\,3p^2$ in silicon) that hybridize to form sp^3 bonds. These directional tetrahedral bonds are very strong, but particularly so in diamond where the bonds, and consequently the lattice constant, are much shorter than in silicon and germanium. When combined with the light atomic masses, these extremely stiff bonds help to explain the high phonon frequencies in diamond.

Further, the phase space for umklapp scattering in diamond is unusually weak. The atypical thermal properties of diamond make it a challenging test of any predictive theory used to describe it. For this reason, diamond is considered a good material for the validation of the ab initio BTE method.

The diamond Grüneisen parameters along high symmetry directions are shown in Figure 6-13.
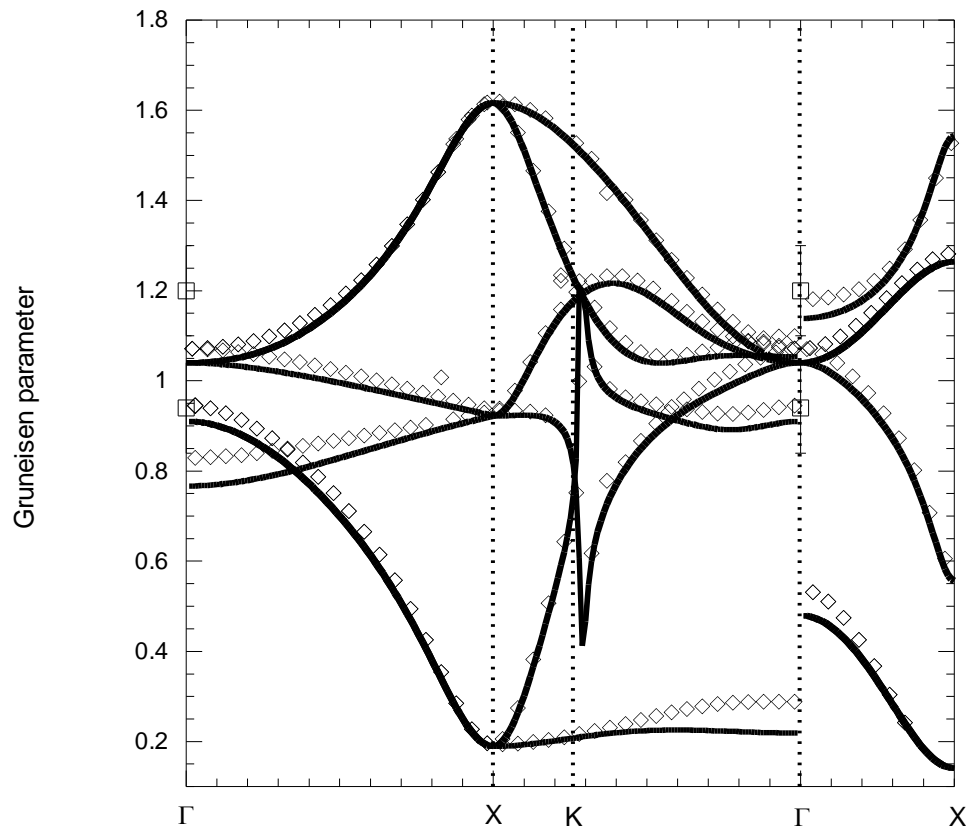

Figure 6-13; Grüneisen parameters for diamond calculated using equation 3.12-2 (open diamonds) and equation 3.12-3 (solid curves). Measured data[95] (open squares) are included for reference.

The parameters calculated with equation 3.12-2 are shown as open diamonds and those calculated with equation 3.12-3 are shown as solid curves. The only measured values[95] are for the optic modes; the open squares represent values determined using both elastic constant and P-V data.

The temperature dependence of $\alpha(T)$ is shown in Figure 6-14.
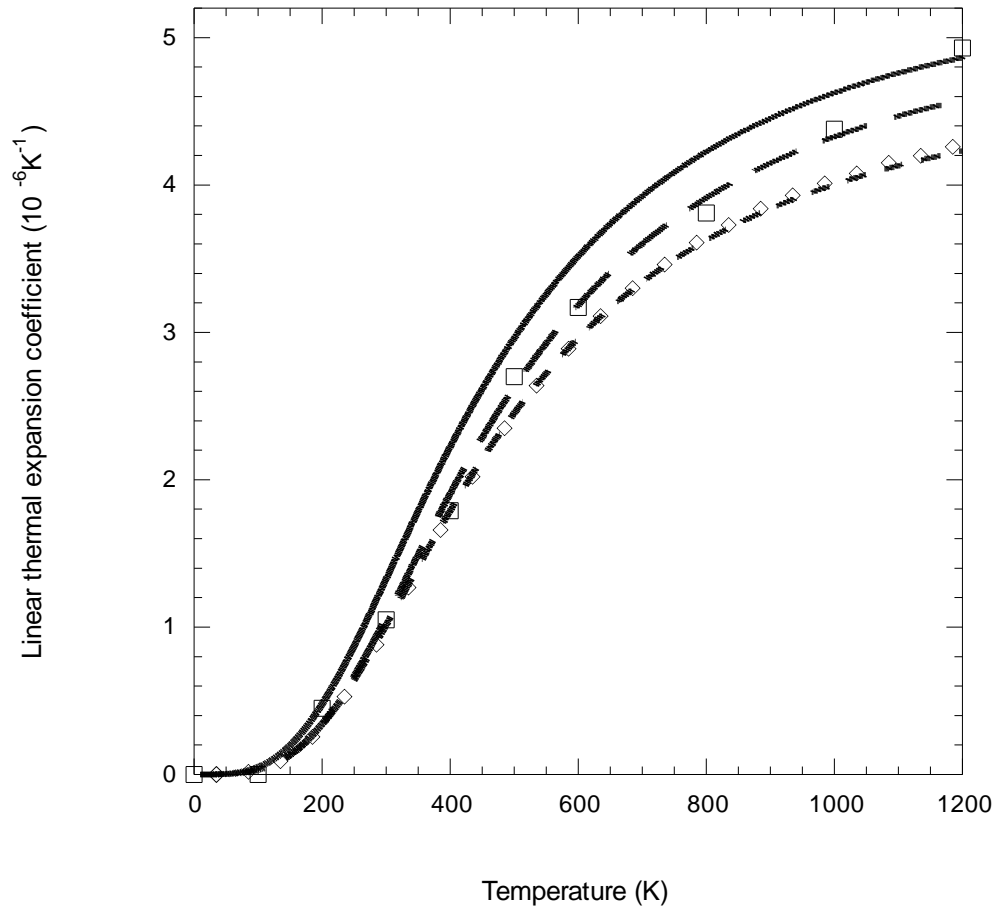

Figure 6-14; $\alpha(T)$ of diamond for cut-off energies of 60Ry (solid curve), 80Ry (long-dashed curve), 100Ry (short-dashed curve), 120Ry (open diamonds) and measurements[87] (open squares).

As with silicon and germanium, the calculations are consistently lower than the measured values across the whole temperature range. The calculations for E_{cut} values of 60Ry (solid curve), 80Ry (long-dashed curve), 100Ry (short-dashed curve) and 120Ry (open diamonds) are compared with

experiment (open squares)[87] and demonstrate that an E_{cut} of 100Ry is required to achieve convergence.

Isotopically enriched diamond samples of 0.07% and 0.1% ^{13}C are available[96]; the remaining atoms being ^{12}C. The mass variance parameter, g_2 for these samples is 4.857x10^{-6}. In Figure 6-16, the calculated values of κ_L for isotopically enriched diamond (solid curve) are compared with the following measured values: open circles[96], crosses[97] are isotopically enriched samples with 0.07% ^{13}C and the open diamonds[98] are for isotopically enriched samples with 0.1% ^{13}C.
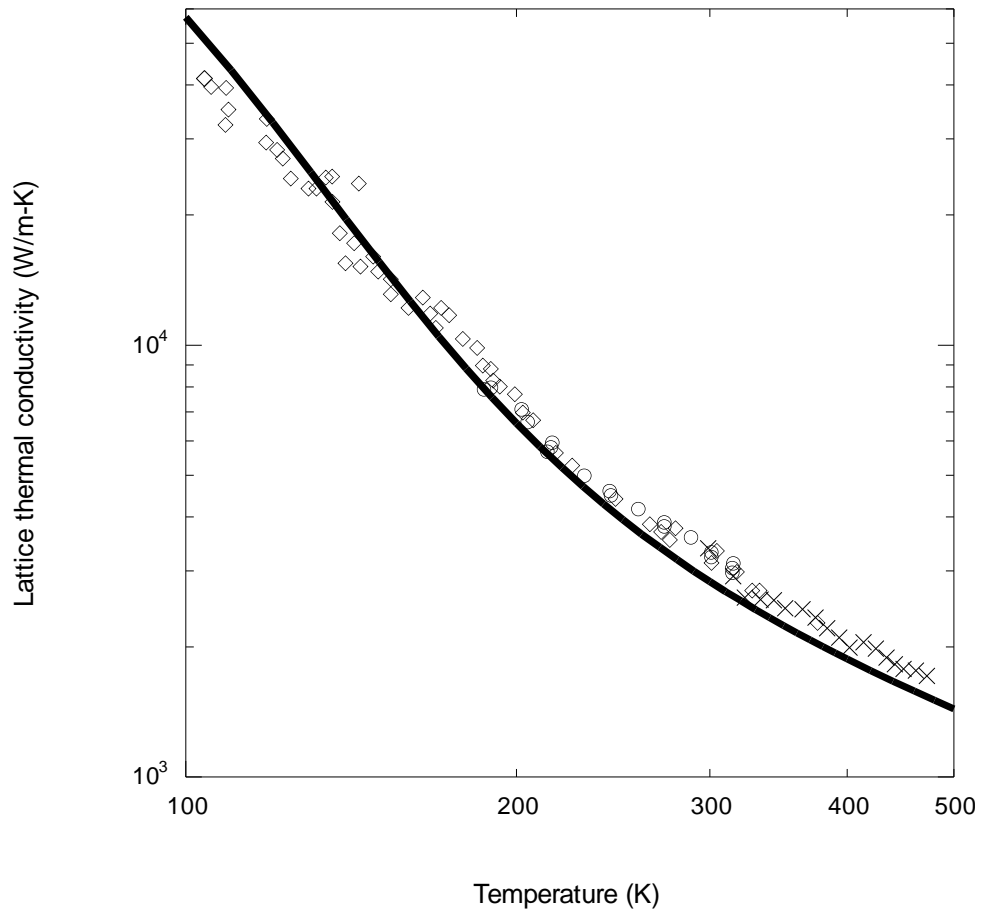

Figure 6-15; Calculated (solid curve) κ_L of isotopically enriched diamond compared with measured 0.07% ^{13}C (open circles[96] and crosses[97]) and 0.1% ^{13}C (open diamonds[98]) samples.

103

Naturally occurring diamond is composed of 1.1% ^{13}C. The mass variance parameter, g_2 in this case is 7.541x10^{-5}. The calculated values of κ_L (solid curve) for naturally occurring diamond are compared with measurements in Figure 6-16. The open diamonds[99], open squares[96] and crosses[99] are for naturally occurring type IIa crystals and the open cirlces[97], open triangles[96] and plusses[98] are for synthetically produced 1.1% ^{13}C crystals.
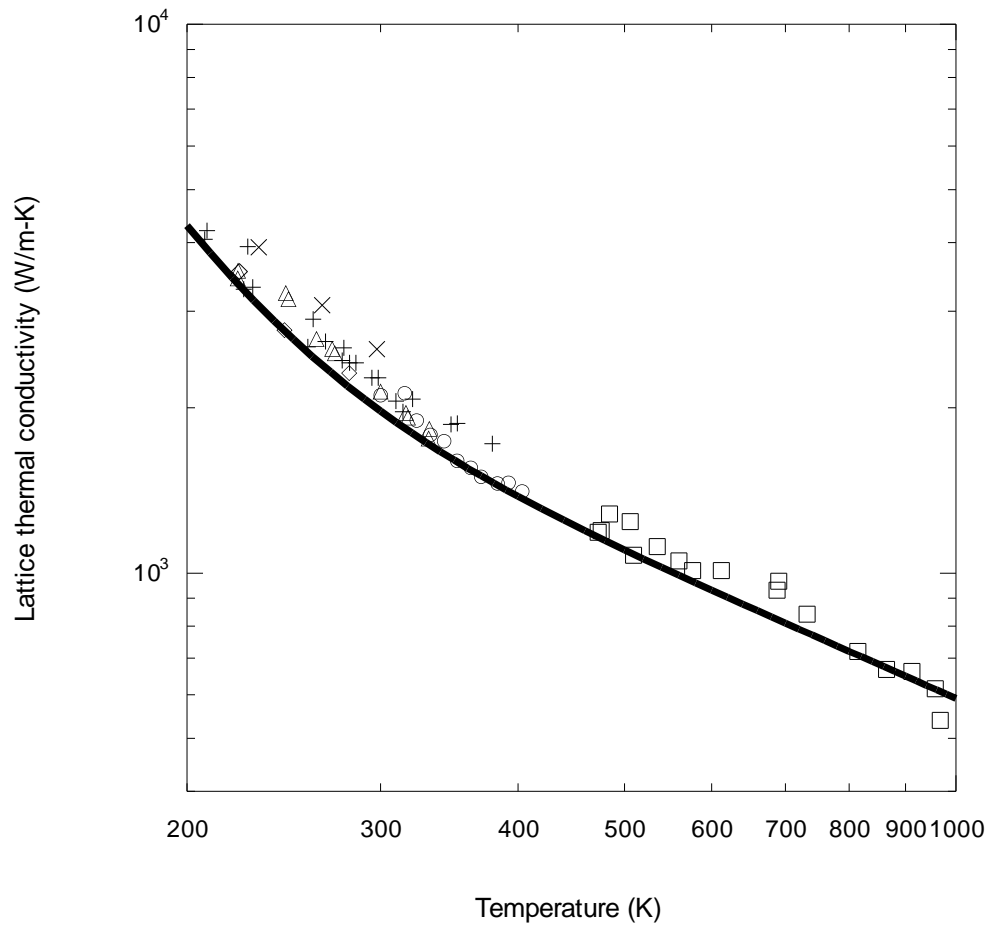

Figure 6-16; Calculated κ_L of naturally occurring (solid curve) diamond compared with measurements of type IIa (open diamonds[99], open squares[96] and crosses[99]) and synthetically produced diamonds with 1.1% ^{13}C (open circles[97], open triangles[96] and plusses[98]).

Naturally occurring diamonds always contain substitutional impurities, the most common being nitrogen. The diamonds are classified as either type I or type II dependent on the nitrogen

concentration, with type II diamonds being the highest purity. Type IIa crystals are electrically insulating and purer than the semiconducting type IIb crystals. The semiconducting behavior results from a concentration of boron impurities present in type IIb crystals. As the calculations make no account for the nitrogen (or any other substitutional) impurities, they are compared with the measurements of the type IIa crystals. The synthetic diamonds with 1.1% [13]C also contain other impurities, with nitrogen again being the most abundant. In the literature, naturally occurring IIa diamonds have been measured with κ_L as high as 2559W/m-K[27] and synthetic diamonds with 1.1% [13]C with κ_L as low as 2102W/m-K[97] at room temperature. These numbers suggest that the synthetic diamonds could actually have a larger substitutional impurity concentration than the naturally occurring ones. The calculated room temperature κ_L is 1973W/m-K, below the measured values.

Due to the unusual nature of diamond, there is value in calculating κ_L using different pseudopotentials to establish the possible variance in the results. Using the same procedure outlined in section 6.2, both Kerker[100] and Von Barth-Car[101] pseudopotentials are used to generate harmonic and third-order anharmonic IFCs. For both pseudopotentials, the ground state lattice constant is again 6.675 Bohr. Convergence in $\alpha(T)$ occurs for cut-off energies of 80Ry and 100Ry with the Kerker and the von Barth-Car pseudopotentials respectively.

Figure 6-17 presents the three distinct ab initio calculations of κ_L of isotopically enriched diamond for the BHS (solid curve), Kerker (dashed curve) and von Barth-Car (dotted curve) pseudopotentials. The open circles[96], crosses[102] are isotopically enriched samples with 0.07% [13]C and the open diamonds[103] are for isotopically enriched samples with 0.1% [13]C for reference.

Results for the naturally occurring diamond show the same general trends and behavior as those for the isotopically enriched samples. They are consequently not plotted as they do not demonstrate any new results. It is very difficult to distinguish the dotted curve generated using the von Barth-Car pseudopotential as it lies directly beneath the dashed curve generated with the Kerker pseudopotential.
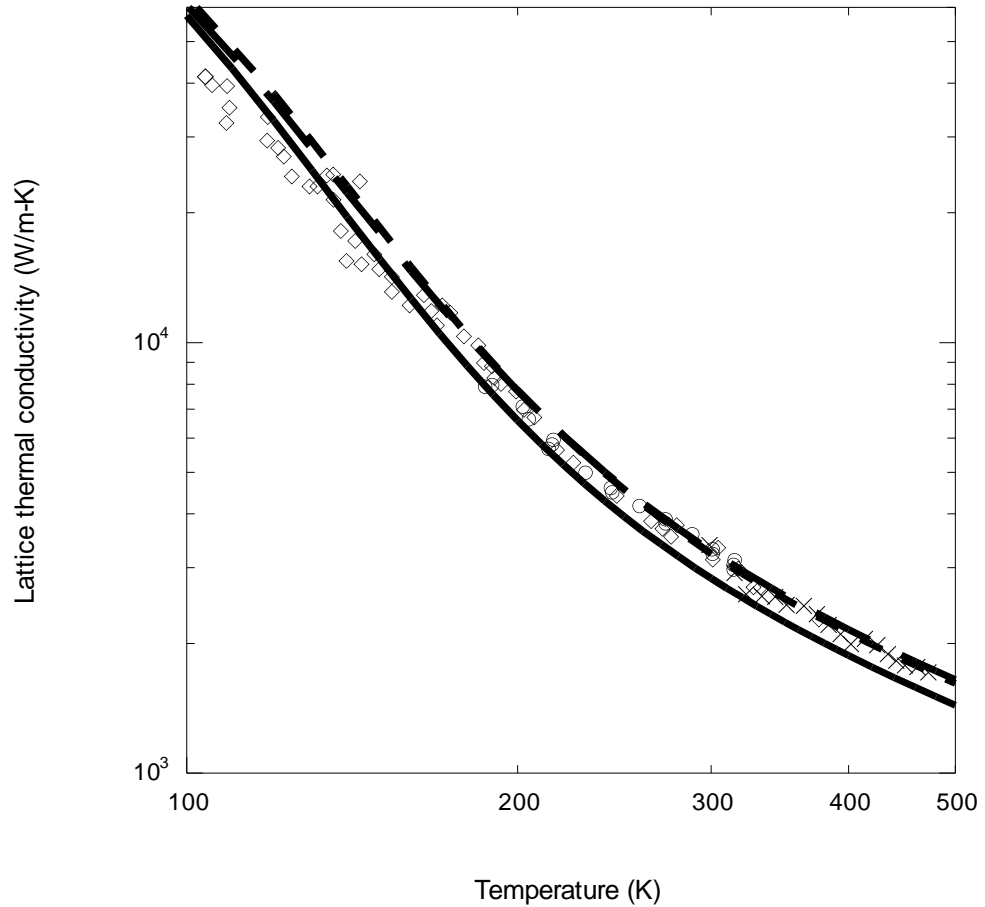
Figure 6-17; κ_L **of isotopically enriched diamond using the BHS (solid curve), Kerker (long-dashed curve) and von Barth-Car (short-dashed curve) pseudopotentials. The experimental data are included for reference.**

It is not the case that the curves place an upper and lower bound on the calculations. Figure 6-17 does show that the deviation in the calculations can be of the order of the deviation of the measured values in the temperature range shown. Similar comparisons for silicon do not show such a large variation. This level of variation in calculations of an unusual material with no adjustable parameters is still extremely good.

6.4.1 Diamond three-phonon phase space

It is commonly assumed that the unusually large thermal conductivity of diamond is due to the large phonon velocities as compared with other group IV materials. These velocities do play a significant role, however they are not the only factor; the unusually weak umklapp scattering also contributes. In an attempt to quantify the role of these two mechanisms, calculations of $\kappa_L^{(i)}$ for silicon are modified by using the diamond phonon frequencies and velocities in equation 3.2-5. In this way, the anharmonicity captured in the term, $\tau_{\lambda\alpha}$, and the three-phonon scattering phase space is based on silicon, but the harmonic terms (phonon frequencies and eigenvectors) are calculated for diamond. Performing this calculation increases the value of the room temperature $\kappa_L^{(i)}$ from 145W/m-K to 712W/m-K, a five-fold increase.

The converse calculation, using the silicon phonon frequencies and eigenvectors and the diamond phase space and three-phonon scattering strengths, causes $\kappa_L^{(i)}$ of diamond to drop from its room temperature value of 2996W/m-K to 1021W/m-K. These results demonstrate that the three-phonon phase space is at least of equal importance as the increased phonon velocities in accounting for the unusually high values of κ_L in diamond. These comparisons are illustrative only, as the decreased phase space is related to the phonon dispersions and the two factors cannot be accurately treated independently.

6.5 Physical interpretation of the iteration process

The iterative solution to the linearized phonon BTE using IFCs obtained through ab initio methods is a major improvement over the RTA in a number of ways. One of the major improvements is the explicit calculation of the three-phonon scattering strengths using the anharmonicity of the crystal. A further fundamental difference is the iteration procedure, which goes beyond the single-mode RTA that is commonly used. The zeroth-order solution to the BTE is equivalent to the single-mode RTA, but the fundamental physical differences between it and the converged solution is explained in detail here. Note that the zeroth-order solution is only equivalent to the single-mode

relaxation time approximation in that the non-equilibrium distribution functions are calculated for *independent* phonons. It is *not* equivalent to an RTA in the sense that inelastic scattering is explicitly dealt with; something that is not compatible with the RTA formalism.

The calculation of κ_L is a numerical sum over a Gaussian quadrature of the product of the mode specific heat, group velocity and the scattering time, τ. At zeroth-order, the non-equilibrium distribution functions for each phonon λ on the Gaussian grid are calculated. These non-equilibrium distributions are calculated independently and there is no coupling between them. This calculation can be equated with the single-mode relaxation time.

The iteration procedure accounts for the fact that the non-equilibrium distribution functions for all phonons are, in actuality, coupled together. The iteration procedure couples together the zeroth-order distributions and calculates new values at each step. Ultimately, the iteration procedure convergences on the real coupled distribution functions.

Marked differences in the behavior of the iteration procedure can be seen between silicon and diamond. For isotopically pure silicon at room temperature, the zeroth-order and converged values of κ_L are 141W/m-K and 145W/m-K respectively. The iteration procedure increases κ_L by only 2.8%. The equivalent values for diamond are 2030W/m-K and 2996W/m-K, a 48% increase. The zeroth-order (solid curve) and converged (dashed curve) values of κ_L for diamond are plotted as a function of temperature in Figure 6-18. The dotted curve represents the percentage increase in κ_L in the iteration procedure.

Figure 6-18 demonstrates that the iteration procedure has a larger effect as the temperature is decreased. This behavior can be understood in terms of the interplay between the three-phonon normal and umklapp scattering processes. The majority of phonons, especially as the temperature is decreased, have small wavevectors $\vec{q}$ and, as such, are usually involved in normal scattering processes. These processes cannot provide thermal resistance, however, they can modify the phonon distributions to larger $\{\vec{q}\}$ wavevectors. Note that the total momentum is not increased (normal processes cannot alter this), but two small $\vec{q}$ phonons can be destroyed to create one larger $\vec{q}$

phonon, conserving the total momentum. Each step of the iteration procedure represents an attempt

at describing the modified phonon distribution functions that solve the BTE.
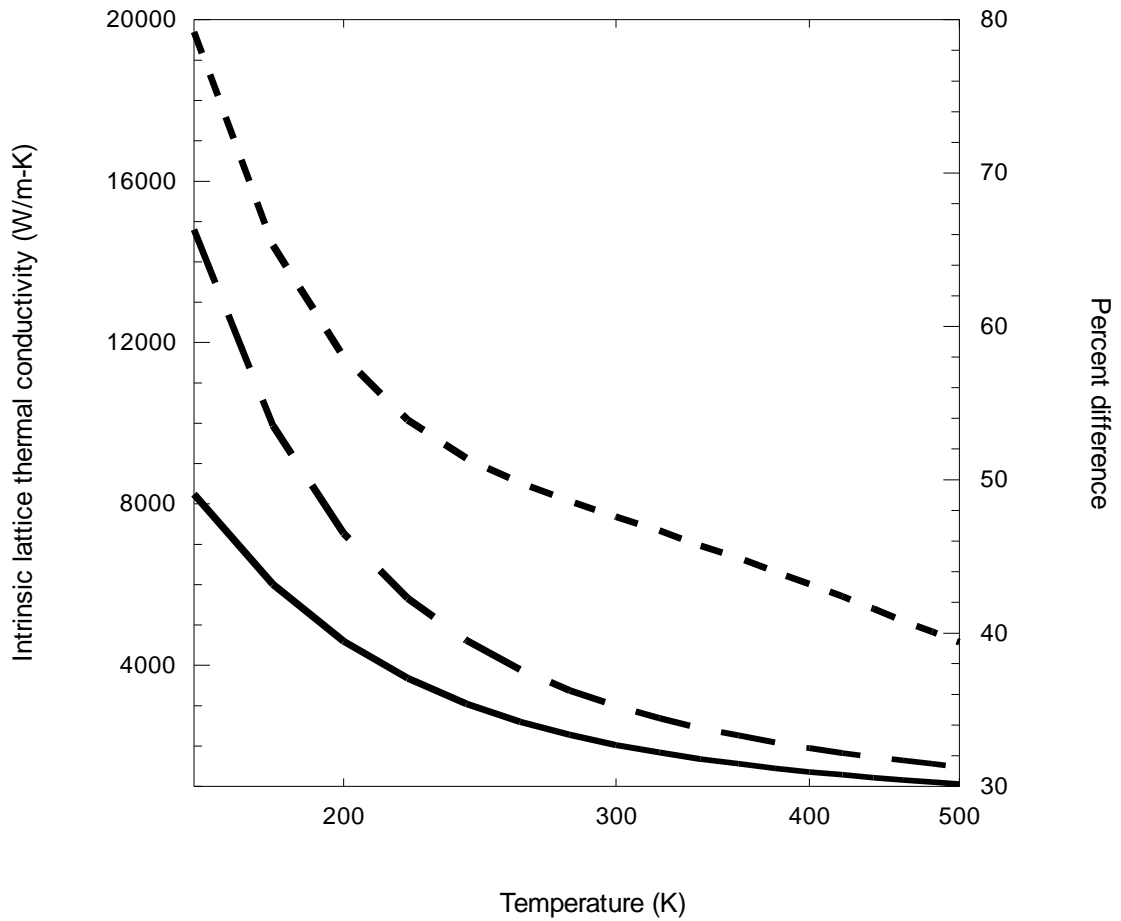

Figure 6-18; The zeroth-order (solid curve) and converged (dashed curve) calculation of κ_L in diamond. The dotted curve represents the percentage difference between the zeroth-order and converged results.

In diamond, a large number of iterations are required before the normal scattering processes have forced the phonon distribution functions to high enough $\{\vec{q}\}$, that umklapp scattering becomes significant. These umklapp scattering processes tend to destroy phonons with large wavevectors and produce phonons with smaller wavevectors and so eventually a steady-state is reached where the

normal and umklapp scattering mechanisms balance. At lower temperatures, it takes the iteration procedure longer to achieve this as the initial phonon distribution has a smaller average set of $\{\vec{q}\}$.

In silicon and germanium, the normal and umklapp scattering phase spaces are comparable and so this steady-state situation is achieved rapidly and without a significant change to the zeroth-order distribution functions. This results in converged results very similar to the zeroth-order ones. As the temperature is decreased, the difference between the zeroth-order and converged solutions also increases. At 50K, κ_L for silicon rises 19% from 6928W/m-K to 8259W/m-K.
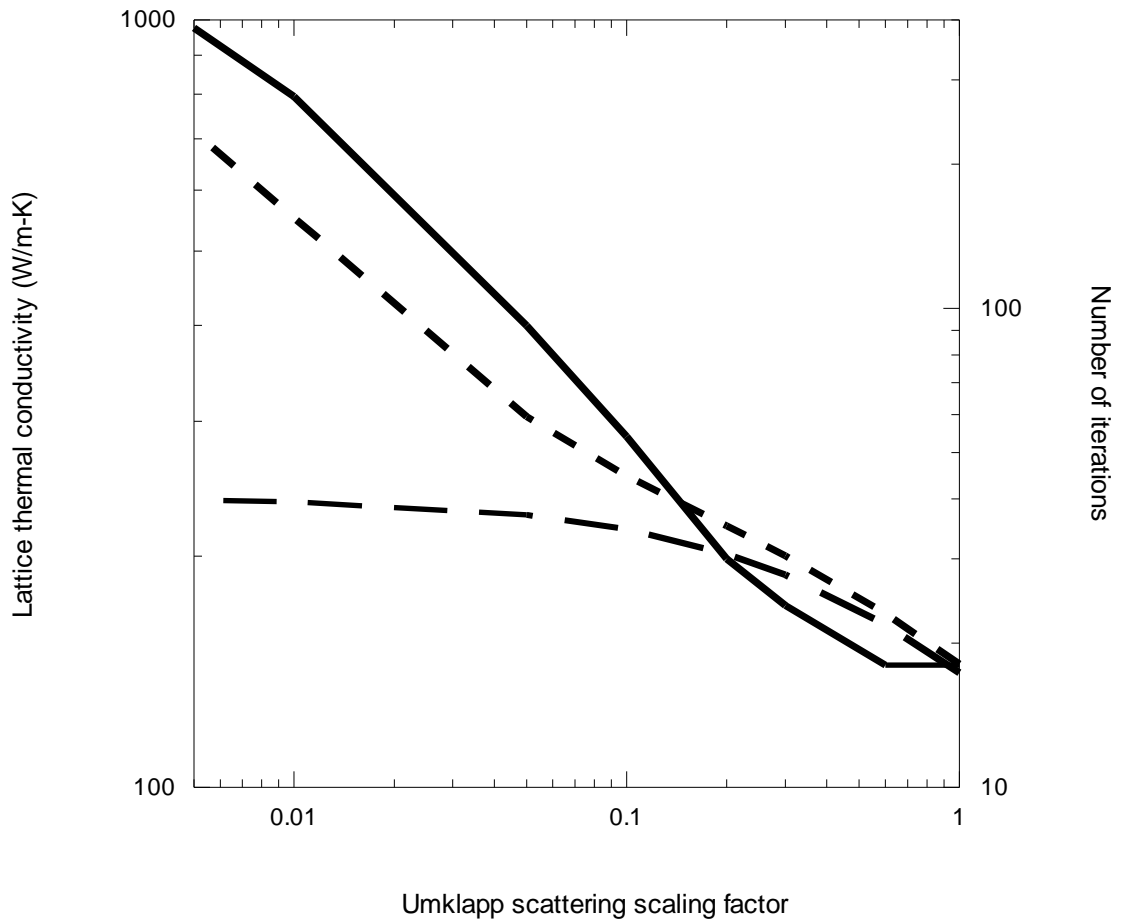

Figure 6-19; The effect of reducing the strength of umklapp scattering on the zeroth-order (dashed curve) and converged (dotted curve) lattice thermal conductivities of silicon. The number of iterations (solid curve) required for convergence are plotted on the right axis.

The iteration procedure is also responsible for recovering the divergence in the thermal conductivity of a pure, defect free crystal as the temperature is decreased. Reducing the temperature has the effect of freezing out the umklapp scattering processes. Thus, reducing the strength of the umklapp scattering processes is equivalent to reducing the temperature. In the limit of zero umklapp scattering, the thermal resistance disappears and κ_L should diverge. This behavior is faithfully reproduced by the iteration procedure.

In Figure 6-19, the results of this investigation are presented for silicon. Each three-phonon umklapp scattering process is multiplied by a scaling factor, $S_U \leq 1$. As this factor is decreased, the strength of umklapp scattering is also decreased. The solid curve shows the number of iterations required for convergence to be achieved and is plotted on the right axis. The zeroth-order solution (dashed curve) and the converged solution (dotted curve) are plotted on the left axis.

With decreasing temperature, the zeroth-order solution increases and then saturates below $S_U \sim 0.05$. As the zeroth-order solution is equivalent to the single-mode relaxation time approximation, this can be viewed as the normal processes contributing to the thermal resistance. With decreasing S_U, it becomes more difficult to find a solution to the BTE and this is reflected in the number of iterations required for convergence to be achieved. With $S_U = 0.001$, convergence cannot be achieved within 500 iterations. The converged value of κ_L at this point is over 1000W/m-K. The converged solution is diverging from the zeroth-order solution and so in the limit of $S_U \rightarrow 0$, $\kappa_L \rightarrow \infty$ as required. The graphical depiction of this divergence is compelling, but it can also be seen mathematically as follows. If the iteration (equation 3.7-4) is cast in the following way

$$F_{\lambda\alpha} = F_{\lambda\alpha}^0 + \Delta F \qquad \qquad \textbf{6.5-1}$$

then it becomes evident that the converged solution has $F_{\lambda\alpha} \approx \Delta F$. For this equality to be true, then

$$F_{\lambda\alpha} Q_\lambda = \sum_{\lambda'\lambda''} \left[W_{\lambda\lambda'\lambda''}^+ (F_{\lambda''\alpha} - F_{\lambda'\alpha}) + \frac{1}{2} W_{\lambda\lambda'\lambda''}^- (F_{\lambda''\alpha} + F_{\lambda'\alpha}) \right] \qquad \textbf{6.5-2}$$

Moving the left hand side over to the right hand side and expanding Q_λ yields

$$\sum_{\lambda'\lambda''} \left[W_{\lambda\lambda'\lambda''}^{+} \left(F_{\lambda''\alpha} - F_{\lambda'\alpha} - F_{\lambda\alpha} \right) + \frac{1}{2} W_{\lambda\lambda'\lambda''}^{-} \left(F_{\lambda''\alpha} + F_{\lambda'\alpha} - F_{\lambda\alpha} \right) \right] = 0 \qquad \text{6.5-3}$$

By comparison with equation 3.6-4, this is equivalent to the vanishing of the collision term. With the vanishing of the collision term, the only way to satisfy equation 3.6-6 is to set the temperature gradient to zero. However, there still exist non-equilibrium distribution functions and so a thermal current exists in the absence of a temperature gradient. This is equivalent to the thermal conductivity being infinite. Therefore, for any calculated result where the converged κ_L is vastly larger than the zeroth-order value, implies $\Delta F \gg F_\lambda^0$ and $\kappa_L \to \infty$.

6.6 Group III-V semiconductors

The calculations required for the polar group III-V semiconductors are more complex and time-consuming than those for the group IV materials. The macroscopic electric field requires that the non-analytic part of the dynamical matrix be evaluated when calculating the phonon frequencies and eigenvectors. This added computational complexity limits the reciprocal space grid densities that can be practicably used. For example, the calculation of the three-phonon scattering phase space for III-V materials using a $6 \times 6 \times 6$ Monkhorst-Pack grid for the harmonic IFCs and a $4 \times 4 \times 4$ Monkhorst-Pack grid for the third-order anharmonic IFCs takes two to three times longer than equivalent group IV calculations.

The inversion symmetry operations that are applied in calculating the third-order anharmonic IFCs for the group IV materials cannot be used for the corresponding III-V calculations. Excepting this added complexity, the calculations for the material parameters investigated in this study remain

	Lattice constant (Bohr)	Cut-off energy, E_{cut}
GaAs	10.42 (10.687)	35Ry
GaP	10.02 (10.303)	45Ry
InP	10.70 (11.094)	60Ry

Table 6-3; The calculated lattice constants and cut-off energies for the studied III-V materials.

the same as discussed for silicon in section 6.2. Table 6-3 lists the values of the lattice constants and cut-off energies used for the III-V materials studied. The measured room temperature lattice constants[29] are included in parentheses.

The harmonic calculations are of the same quality as those for group IV materials. To demonstrate this, the calculated and measured[49] phonon dispersion curves for GaAs are shown in Figure 6-20.
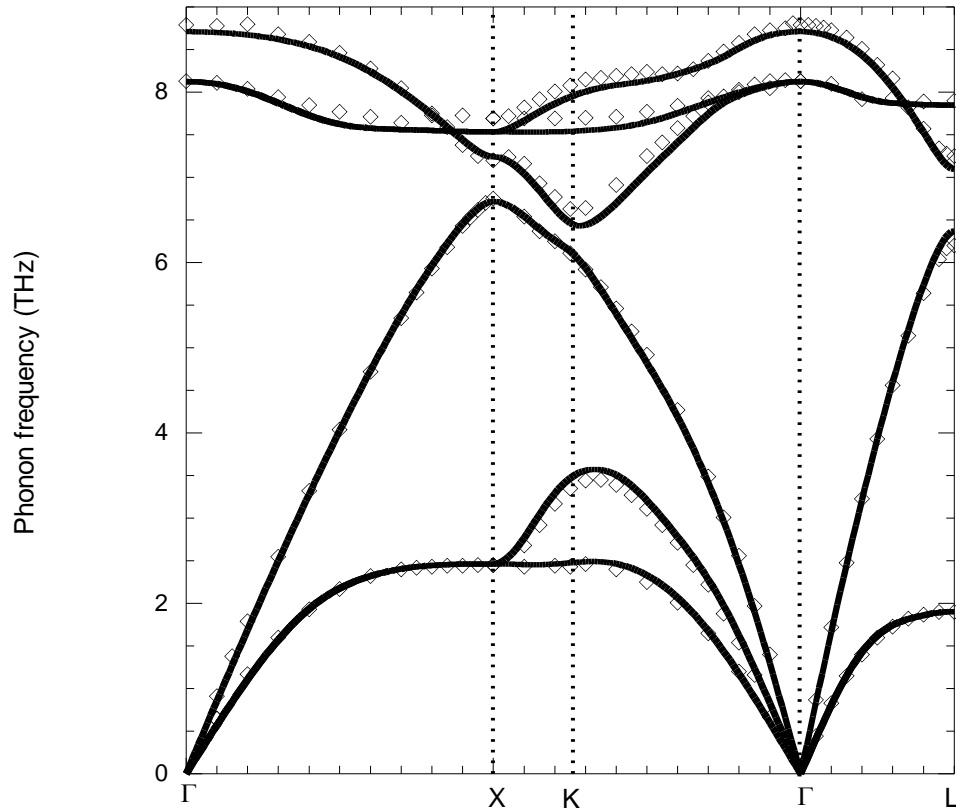

Figure 6-20; Calculated (solid curves) and measured[49] (open diamonds) phonon dispersion curves of GaAs along high symmetry directions.

The most noticeable difference between the phonon dispersion curves of the polar III-V materials and the non-polar group IV materials is the splitting of the optic branches at the Γ-point. The ab initio calculations reproduce the phonon dispersions, and this feature in particular, extremely well.

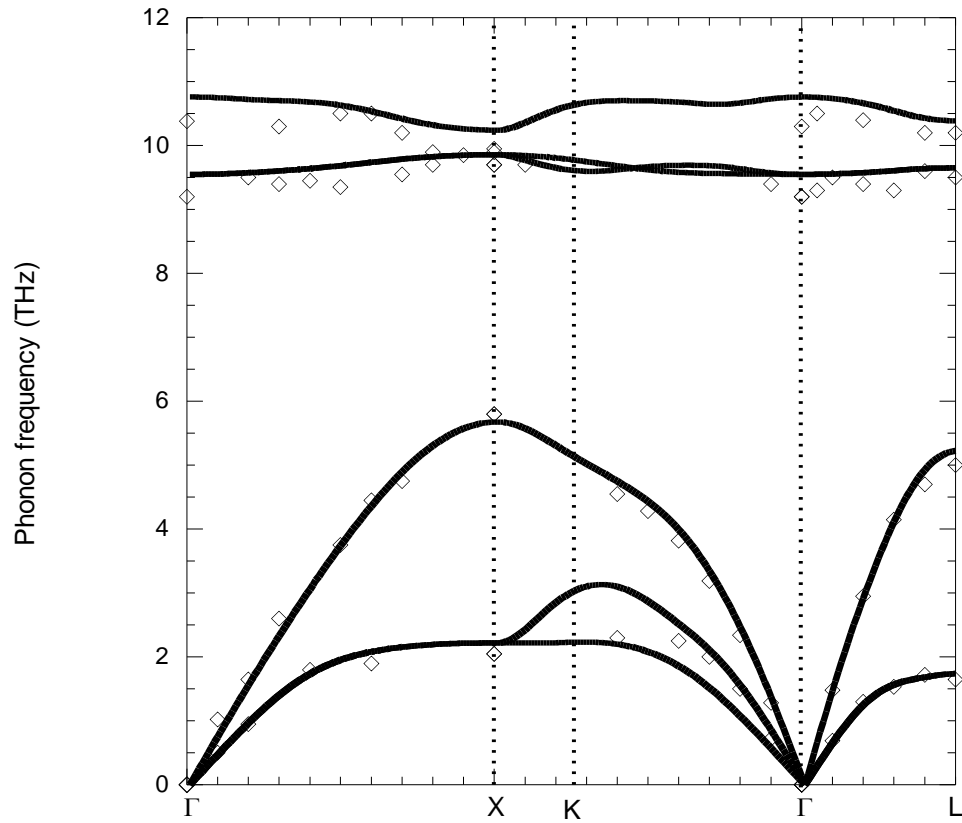The calculated and measured[104] phonon dispersion curves for indium phospide are shown in Figure 6-21.

Figure 6-21; Calculated (solid curves) and measured (open diamonds) phonon dispersion curves of InP along high symmetry directions.

The errors in the measured points are typically of the order 0.1THz, although some, including the transverse optic modes, have some errors of the order 1THz. With this in mind, the agreement between the calculations and the measurements is again extremely good. The phonon dispersions for the other materials are not included as the quality of the ab initio calculations is already well established.

The two methods of calculating the Grüneisen parameters for InP are compared in Figure 6-22. The values calculated from the harmonic IFCs are shown as open diamonds while those using the anharmonic IFCs are shown as solid curves.
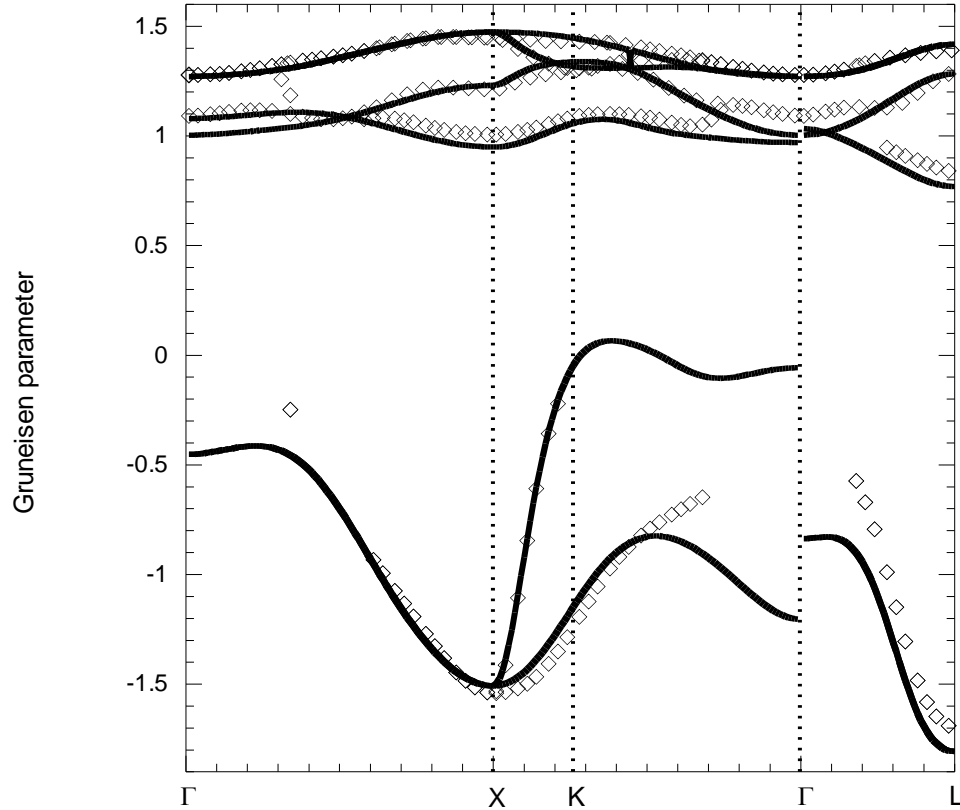

Figure 6-22; Grüneisen parameters of InP calculated using the harmonic IFCs (open diamonds) and both harmonic and anharmonic IFCs.

The data calculated from the harmonic IFCs is not well defined for a large portion of the Brillouin zone close to the zone center. It is in this region that the macroscopic field has the its largest contribution. The values in the optic modes are in very good agreement with each other, however the acoustic modes show good agreement in some regions and poor agreement in others. This could be a result of the k-point mesh for the anharmonic IFCs being too coarse, but computational requirements preclude the investigation of denser meshes.

The temperature dependence of the linear thermal expansion coefficients of GaP are plotted in Figure 6-23. The same phenomena and shortfalls as for the group IV materials are observed.
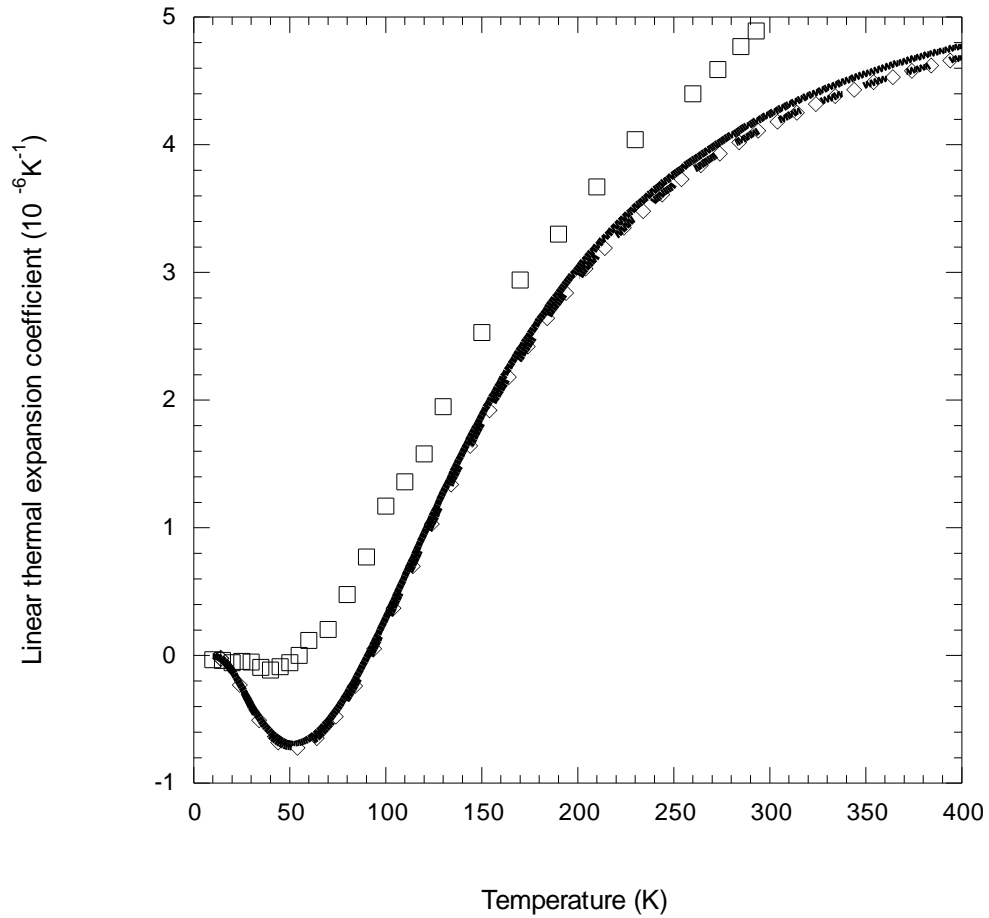
Figure 6-23; The temperature dependence of the linear thermal expansion coefficient of GaP for cut-off energies of 25Ry (solid curve), 45Ry (dashed curve) and 55Ry (open diamonds). The measured values[105] are shown as open squares.

The final calculations are for κ_L. All of the ab initio BTE calculations are for isotopically pure samples. Figure 6-24 shows the calculated temperature dependence of κ_L for isotopically pure GaAs (solid curve) compared with measured data[106] for isotopically enriched (open diamonds) and naturally occurring (open squares) GaAs samples. The naturally occurring samples consist of

116

60.11% [69]Ga and 39.89% [71]Ga. Arsenic is a monoisotopic element. The isotopically enriched crystals have 99.6% [71]Ga.
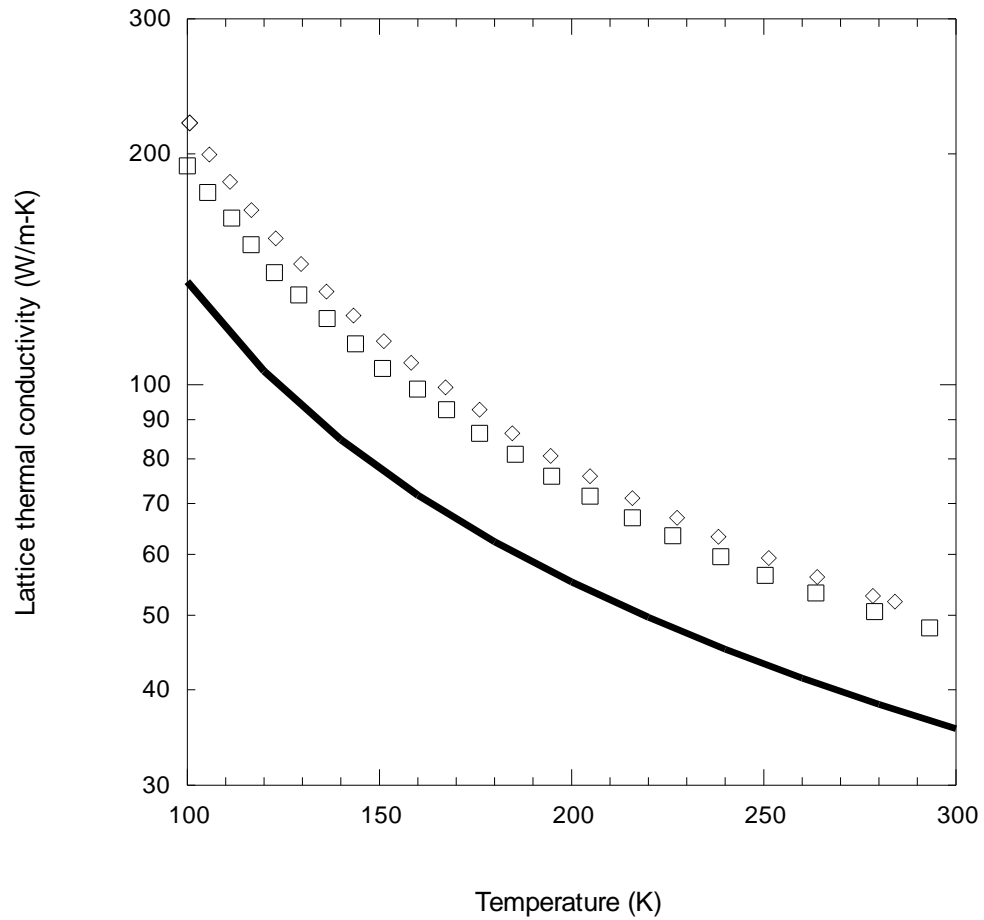
Figure 6-24; Thermal conductivity calculations (solid curve) of GaAs compared with measurements[106] of isotopically enriched (open diamonds) and naturally occurring (open squares) GaAs samples.

The calculations are consistently below both sets of measurements. Since the calculations are for an isotopically pure crystal, calculations are expected to be higher than the measurements. The reason for this discrepancy is not well understood, but may be related to the errors demonstrated in the Grüneisen parameters resulting from some problem with the anharmonic IFCs.

Figure 6-25 shows the temperature dependence of the calculated κ_L for GaP (solid curve) and InP (dashed curve) compared with the corresponding experimentally measured values for GaP[107] (open diamonds) and InP[108] (open squares).
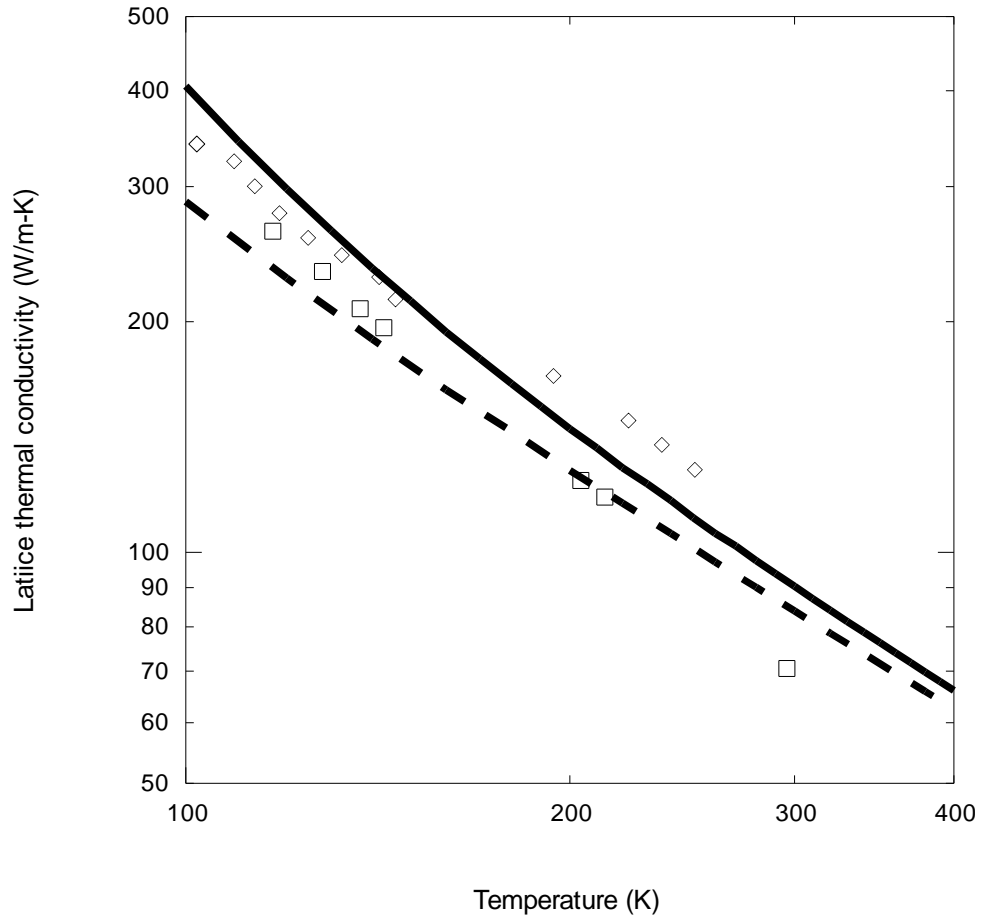
Figure 6-25; Thermal conductivity calculations of GaP (solid curve) and InP (dashed curve) compared with the corresponding measured values (open diamonds[107] and open squares[108]).

In both of the GaP and InP, the measured values intersect the calculated values. In the case of InP, the measured values show a temperature dependence of the form[108] $\kappa \sim T^{-3/2}$ as opposed to the expected high temperature form $\kappa \sim T^{-1}$. The reason for this is speculated to be due to point impurity defects as the effect of isotopic defects is estimated to be small.

118

7 Relaxation times

In chapter 3, an iterative solution to the linearized Boltzmann equation was developed that allows the explicit evaluation of the complex collision term. The complexity of the required calculations coupled with the computational demands is such that for the last half century, relaxation time approximations (RTAs) have been necessary to circumvent the evaluation of this term, vastly simplifying the calculations of κ_L. The practical value of such a method is clear. For most semiconductor and insulating materials, there are a number of different phonon scattering mechanisms, e.g. scattering from defects, impurities and boundaries as well as phonon-phonon scattering that contribute to κ_L. The validity of the RTA when used to describe inelastic phonon-phonon scattering mechanisms is questionable, however.

Previous attempts at deriving forms for relaxation times have centered on some core approximations. At the core, is the single-mode relaxation time approximation that allows each phonon's non-equilibrium distribution function to be calculated independently of the other phonons. Also, the assumption of low temperatures, small phonon frequencies and linear (Debye) dispersions are used and all optic phonons are typically omitted from the calculations. The resulting forms have been modified over time, but all stem from these same underlying approximations. Due to the usefulness of RTAs in many different calculations, these forms have then been used to study many different materials and properties, often in situations where the underlying approximations are no valid.[21]

The three-phonon scattering times are accessible to the ab initio method used in this study. In the following sections, a brief history of the RTA method is given and then the approximations are investigated and their validity tested. Finally, the ab initio method described in chapter 6 to calculate κ_L of semiconducting and insulating materials is used to develop improved RTA forms, specifically for use at room temperature and above.

Another major topic in this section involves highlighting the crucial importance that optic phonons play in determining κ_L.

7.1 Commonly used relaxation times

After the work of Debye[109] and Peierls[110] who first formulated the ideas of treating the thermal resistance in non-metals as resulting from the anharmonic scattering of vibrational waves, many papers invoked a number of approximations in an attempt to calculate κ_L. Initially, the crystal was assumed to be isotropic and this led to the prediction that all infinite non-metals should have divergent thermal conductivities when only longitudinal modes in the small $\vec{q}$ limit are considered. This was not observed experimentally and so attempts to better describe the crystal were made. Pomeranchuk[111-113] invoked four-phonon processes, Herpin[114] used imperfections in the crystal lattice and then Klemens[1] then provided a detailed treatment of κ_L, but dismissed the divergence as an effect eliminated by umklapp processes.

A thorough treatment by Herring[115] used the anisotropy of the crystal as a means of explaining away the divergence. In order to solve the BTE in the RTA, the collision term is written in terms of a relaxation time τ

$$\frac{\partial n_j(\vec{q})}{\partial t}\bigg]_{(\alpha)} = -\frac{n_j(\vec{q}) - n_j^0(\vec{q})}{\tau_{(\alpha)}} = -\frac{n_j^1(\vec{q})}{\tau_{(\alpha)}} \qquad \text{7.1-1}$$

where $n_j(\vec{q})$ is the number of phonons in mode $(j, \vec{q})$, $n_j^0(\vec{q})$ is the equilibrium Bose distribution and $n_j^1(\vec{q})$ is the deviation from the equilibrium distribution. Relaxation times were defined for all of the different phonon scattering mechanisms (denoted by the subscript α): normal and umklapp three-phonon scattering, impurity scattering, boundary scattering etc. Some of the more influential RTA models are described briefly in the following sections.

7.1.1 Callaway model[2]

The observation that normal and umklapp scattering processes are fundamentally different and need to be treated separately was addressed by Callaway. The umklapp processes tend to relax a phonon system back to the equilibrium Bose-Einstein distribution. The normal processes, however, conserve momentum and so cannot alter the sum of the phonon wavevectors, $\sum \vec{q} = constant$. If a

thermal current is established in a material and the thermal gradient is removed, the thermal current will continue to flow if normal scattering is the only scattering mechanism available. Therefore, in contrast to umklapp scattering, normal processes relax the phonon system back to a displaced (or flowing) distribution, $n_j(\vec{q}, \vec{\mu})$.

$$n_j(\vec{q}, \vec{\mu}) = \frac{1}{exp[(\hbar\omega - \vec{\mu} \cdot \vec{q})/k_B T] - 1} \qquad \textbf{7.1-2}$$

where $\vec{\mu}$ defines the total crystal wavevector of the flowing distribution. The relaxation times describing normal processes and scattering processes that do not conserve momentum are defined as τ_N and τ_U. Since $\vec{\mu}$ is related to the small temperature gradient, it itself is small and so the flowing distribution can be written[116]

$$n_j(\vec{q}, \vec{\mu}) = n_j^0(\vec{q}) + \frac{\vec{\mu} \cdot \vec{q}}{k_B T} n_j^0(\vec{q})\left(n_j^0(\vec{q}) + 1\right) \qquad \textbf{7.1-3}$$

The deviation from equilibrium, $n_j^1(\vec{q}) = n_j(\vec{q}) - n_j^0(\vec{q})$ is expressed as

$$n_j^1(\vec{q}) = -\tau_T \vec{v} \cdot \nabla T \frac{\hbar\omega}{k_B T^2} n_j^0(\vec{q})\left(n_j^0(\vec{q}) + 1\right) \qquad \textbf{7.1-4}$$

where $\tau_T = \tau_c(1 + \beta/\tau_N)$ and $\tau_c^{-1} = \tau_N^{-1} + \tau_U^{-1}$ is a combined collision relaxation time. The term $(1 + \beta/\tau_N)$ is a correction to the conventional relaxation time, τ_c that accounts for the nature of the normal scattering processes. In order to determine the form of the total relaxation time it is assumed that the phonon dispersions are reduced to a single linear, isotropic branch, hence $\omega = cq$, where c is the speed of sound in the crystal. The Callaway model breaks the thermal conductivity calculation into two parts,

$$\kappa_L = \kappa_1 + \kappa_2 \qquad \textbf{7.1-5}$$

where the two parts can be written

$$\kappa_1 = \frac{k_B^4}{2\pi^2 \hbar^3 c} \int_0^{\Theta/\mathrm{T}} dx \tau_c \frac{x^4 e^x}{(e^x - 1)^2} \qquad \textbf{7.1-6}$$

121

$$\kappa_2 = \frac{k_B^4 \beta}{2\pi^2 \hbar^3 c} \int_0^{\Theta/\mathrm{T}} dx \frac{\tau_c}{\tau_N} \frac{x^4 e^x}{(e^x - 1)^2}$$

where the substitution $x = \hbar\omega/k_B T$ has been made and Θ is the Debye temperature. Equation 7.1-7 includes the factor β and is divided through by τ_N. The term β is calculated using the fact that normal processes conserve momentum and takes the form

$$\beta = \left. \int_0^{\Theta/\mathrm{T}} dx \frac{\tau}{\tau_N} \frac{x^4 e^x}{(e^x - 1)^2} \middle/ \int_0^{\Theta/\mathrm{T}} dx \frac{1}{\tau_N} \left(1 - \frac{\tau}{\tau_N}\right) \frac{x^4 e^x}{(e^x - 1)^2} \right.$$

This method of calculating κ_L has the satisfying physical consequence that in the limit of no umklapp scattering, $\tau_U \to \infty$, then $\tau \to \tau_N$ and $\beta \to \infty$, which means that κ_L diverges as required.

The final step in achieving a model capable of calculating κ_L is to fix the form of the relaxation times for the different scattering mechanisms. Herring[115] established, in the single-mode RTA, that the relaxation time associated with a longitudinal acoustic phonon of small wavevector $\vec{q}$ can be calculated as

$$\tau^{-1} = q^a T^{5-a}$$

at low temperatures. The exponent, a is determined by crystal symmetries. This relation was derived for a total relaxation time where normal and umklapp scattering are not treated separately.

Callaway used this relation to provide relaxation times for the separated normal and umklapp processes. The exponent a was chosen to be two for mathematical simplicity. The value of a is also constrained by the fact that the κ_L integral will only converge for $a \leq 2$. Callaway assumed the forms $\tau_N^{-1} = A\omega^2 T^3$ for normal processes and $\tau_U^{-1} = B\omega^2 T^3 e^{-\Theta/b\mathrm{T}}$ for umklapp processes, where b is a constant characteristic of the vibrational spectrum and A and B are adjustable parameters to be fixed by comparison with experimental measurements. The extra temperature dependent term in the umklapp relaxation time accounts for the exponential weakening of this scattering mechanism at low temperatures.

7.1.2 Holland model[117]

The Callaway model produces good agreement with some experimental data at low temperatures, but requires extensive numerical integration to calculate κ_L. A model proposed by Holland[117] attempted to simplify the Callaway model and use the detailed phonon spectrum and density of states measurements that had just become available to remove some of the restrictive approximations. Here, the heat flow carried by the transverse acoustic (TA) and longitudinal acoustic (LA) branches were separated out and treated separately. The umklapp scattering, whose relaxation times had previously been assigned rather than derived were also given more attention.

7.1.3 More recent developments

The RTA approach has been used extensively since its development. Indeed, the method has been used for many different structures, at all temperature ranges, even well outside the low-temperature, small $\vec{q}$ and Debye limit for which the methods were originally developed. This is testament to the complexity of explicitly calculating the effects of three-phonon scattering. The list of works that use the RTA and further developments is extensive and this section is not intended to be an exhaustive chronology of the RTA, however, to motivate the forms of the relaxation times, some previously calculated versions are highlighted.

In studying germanium crystals with different isotopic compositions, M. Asen-Palmer et al.[3] used the Callaway and Holland models along with modified versions to compare theory with measurement. Morelli et al.[118] adopted a modified Callaway model and attempted to apply physical arguments to the calculation of the set of coefficients $\{B\}$ appearing in the following expressions.

$$\left[\tau_U^{L(T)}(\omega)\right]^{-1} = B_U^{L(T)}\omega^2 T e^{-\Theta_{\mathrm{L(T)}}/3\mathrm{T}} \qquad \textbf{7.1-10}$$

where the coefficient is calculated as

$$B_U^{L(T)} \approx \frac{\hbar\gamma_{L(T)}^2}{Mv_{L(T)}^2\Theta_{\mathrm{L(T)}}} \qquad \textbf{7.1-11}$$

where $\gamma_{L(T)}$ is the mode Grüneisen parameter of the longitudinal (transverse) mode, M is the average mass of an atom in the crystal, $\Theta_{\mathrm{L(T)}}$ is a modified Debye temperature based on the zone-boundary

longitudinal (transverse) acoustic frequency, ω_{max} and $v_{L(T)}$ is the velocity of the longitudinal (transverse) branch. The forms for the normal processes are

$$[\tau_N^L(\omega)]^{-1} = B_N^L \omega^2 T^3 \qquad \text{7.1-12}$$

$$[\tau_N^T(\omega)]^{-1} = B_N^T \omega T^4 \qquad \text{7.1-13}$$

and the coefficients are given by

$$B_U^L \approx \frac{k_B^3 \gamma_L^2 V}{M \hbar^2 v_L^5} \qquad \text{7.1-14}$$

$$B_U^T \approx \frac{k_B^4 \gamma_T^2 V}{M \hbar^3 v_T^5} \qquad \text{7.1-15}$$

The values of the mode Grüneisen parameters were taken to be adjustable in order to fit the calculations to the experimental data. Prior to the development of high room temperature relaxation time forms, some of the approximations behind the previously discussed RTA models are discussed.

7.2 Small momentum approximation

One of the commonly made approximations is that the only phonons responsible for thermal transport in the low temperature limit are the long-wavelength acoustic phonons. The phonon dispersions are then treated as a single isotropic branch in the linear Debye limit, where $\omega = cq$. The three-phonon scattering phase space search allows this approximation to be probed directly. Each scattering process involves three phonons and a total momentum vector, q_{tot} dependent on the magnitudes of all three of these phonons can be constructed as

$$q_{tot} = \sqrt{|\vec{q}|^2 + |\vec{q}'|^2 + |\vec{q}''|^2} \qquad \text{7.2-1}$$

All of the three-phonon scattering processes that obey the conservation conditions in equation 3.11-10 are tabulated according to their q_{tot}. This allows a plot of the number of events versus the magnitude of q_{tot} to be constructed. In Figure 7-1, this plot is constructed for the following scattering channels: all three phonons in the acoustic branches (a-a-a) in normal (solid curve) and umklapp (long-dashed curve) processes. Scattering processes where one phonon is in an optic

124

branch (a-a-o) are also divided into normal (short-dashed curve) and umklapp (dashed-dotted curve) processes. In all of these scattering processes, the phonon $\vec{q}$ is in the longitudinal acoustic branch.
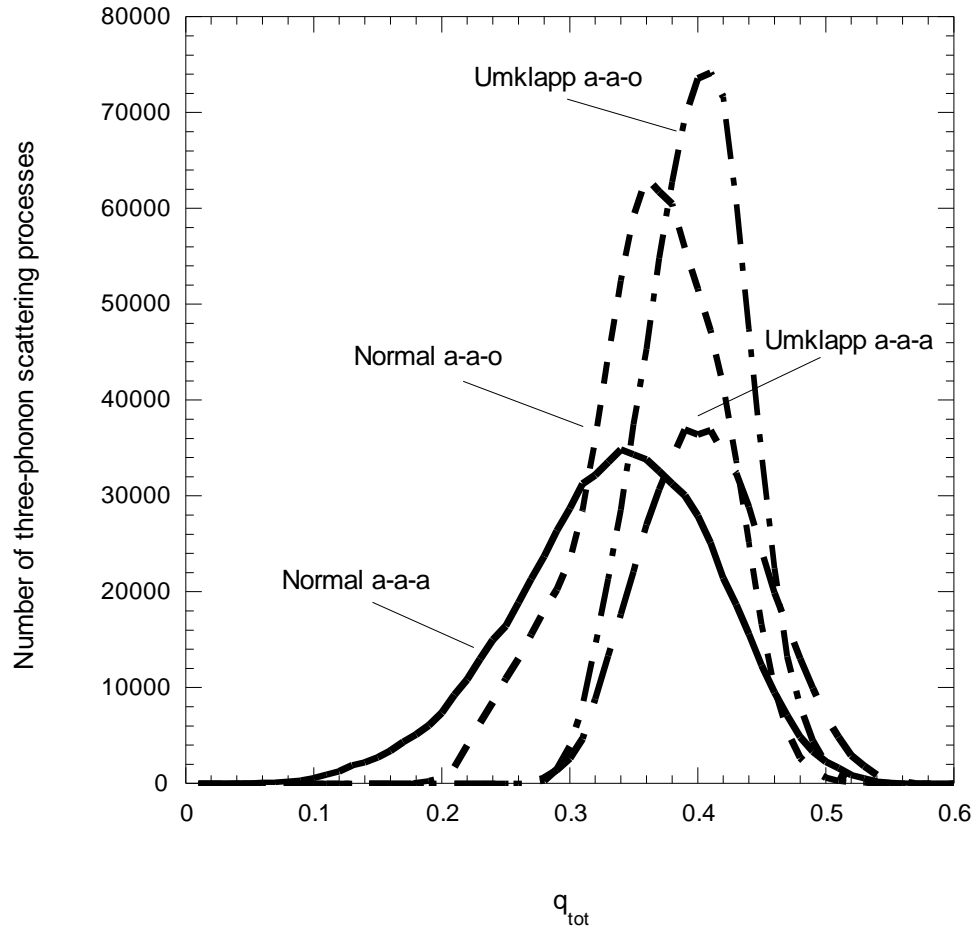

Figure 7-1; Distribution of the three-phonon scattering processes with respect to the magnitude of the total momentum, q_{tot}. The normal a-a-a (solid curve), umklapp a-a-a (long-dashed curve), normal a-a-o (short-dashed curve) and umklapp a-a-o (dashed-dotted curve) are plotted separately.

One of the most obvious features of Figure 7-1 is that there are far more scattering channels involving two acoustic and one optic phonon than three acoustic phonons (see section 7.4). It is also

clear that the umklapp processes have, on average, a larger total momentum vector as would be expected.

The conclusions to be drawn from Figure 7-1 are not immediately apparent. It is clear that the vast majority of three-phonon scattering processes that simultaneously satisfy momentum and energy conservation occur away from the zone center. The relaxation time is inversely proportional to the scattering strength and so it is large where there are fewer scattering processes. The largest contribution to κ_L therefore occurs for small values of q_{tot}, when there are *very few* scattering channels. A lack of scattering ensures that the phonons are long-lived and can carry heat through the crystal. Thus, it is close to the zone center where there are not many allowable scattering processes that the relaxation time has its largest value and hence the largest contribution to the lattice thermal conductivity.

As $q_{tot} \to 0$, the umklapp scattering curves (long-dashed and dashed-dotted) fall to zero more rapidly than do the normal curves. As expected, for small $\vec{q}$, it is the normal scattering channels that will be most important. Care must be taken when drawing conclusions from this figure, however, as no phonons are treated in isolation. Thus, while q_{tot} may be small, it does not necessarily follow that the individual phonons involved in the scattering process have small $\vec{q}$.

7.3   Validity of the relaxation time approximation

The RTAs are underpinned by the assumption that the non-equilibrium phonon distribution of phonon $\vec{q}$ is calculated independently of the other phonons; the so-called single-mode RTA. Since the zeroth-order solution to the linearized BTE is formally equivalent to this approximation, the single-mode RTA can be directly analyzed. For silicon and germanium, the zeroth-order solution does not differ significantly from the converged result at room temperature; 2.8% and 6% for silicon and germanium respectively. This means that coupling together the non-equilibrium distribution functions (a role of the iteration procedure) does not significantly alter the result. Consequently, the single-mode RTA is expected to be a reasonable approximation.

For diamond, on the other hand, the room temperature increase of κ_L from the zeroth-order to the converged solution is 48%. This suggests that the zeroth-order non-equilibrium distribution functions are not a good approximation to the actual distributions that are solutions to the BTE. In diamond this is due to the small phase space for umklapp scattering that requires the iteration process to significantly shift the phonon distribution functions to allow the umklapp scattering to contribute (see 6.5 section for further discussion). The single-mode RTA is therefore a poor approximation when applied to diamond as there is significant coupling between the different non-equilibrium distributions.

The room temperature forms of the relaxation times developed in this section depend on the separation of the normal and umklapp scattering processes using Matthiessen's rule

$$\frac{1}{\tau} = \sum_i \frac{1}{\tau_i} \hspace{3cm} \text{7.3-1}$$

where the sum runs over all the different scattering mechanisms. This relation is valid for the uncoupled zeroth-order solution, but not for the converged one. This means that all RTA forms are based on the zeroth-order solution which is a very poor approximation for diamond.

In conclusion, the single-mode RTA is only valid for materials where the iteration process has a small effect on the thermal conductivity.

7.4   Role of optic phonons

The RTAs developed in section 7.1 were all derived using the linear Debye model for the phonon dispersions and the approximation that the optic phonons play an insignificant role in the calculation of κ_L. The basis for this argument is that the low occupation of the high-energy optic phonons coupled with their low group velocities ensure that they contribute little to κ_L. In principle, this argument is valid up to and beyond room temperature. The acoustic phonons do carry the vast majority of the heat in the crystal and the optic phonons contribute little in the integral calculation of

κ_L. For example, the room temperature κ_L of isotopically enriched silicon is 145W/m-K, of which only 7W/m-K ($< 5\%$) is contributed by the optic branches.

The optic phonons are critically important, however, in their capacity to provide scattering channels for the acoustic phonons. The phase space search on a 32 point Gaussian grid yields on the order of ten million distinct three phonon scattering processes. These processes can be broken down according to event type (normal or umklapp) and according to the branches of the phonons involved; a-a-a refers to acoustic-acoustic-acoustic scattering in which all three phonons involved in the scattering process are from acoustic branches. Those scattering events involving one optic phonon are designated as a-a-o. Table 7-1 lists the percentage of the scattering processes that are umklapp processes when the phonon, λ is in an acoustic branch. When the phonon λ can come from any of the branches, including the optic branches, this percentage is essentially unchanged. Also included are the percentage of scattering processes for phonon $\vec{q}$ in the TA and LA branches that involve one optic phonon for silicon, germanium and diamond.

	Umklapp	a-a-o in TA	a-a-o in LA
Silicon	50%	59%	58%
Germanium	52%	53%	54%
Diamond	28%	88%	55%

Table 7-1; Percentage of three-phonon scattering processes that are umklapp processes and the percentage that involve one optic phonon.

Over 50% of all three-phonon scattering processes involve an optic phonon for all the materials. For diamond, this is even more pronounced with nearly 90% of the scattering processes from the TA mode involving one optic phonon. The importance of the optic modes is only increased when acoustic-optic-optic scattering is also included. It is clear, therefore, that in calculating the scattering time, $\tau_{\lambda\alpha}$, the role of the optic phonons is critical and their omission will yield incorrect forms for the relaxation times. Figure 7-2 shows the temperature dependence of κ_L for isotopically enriched silicon. The solid curve shows the ab initio calculations of κ_L and the open diamonds are the

measured values.[20] The dashed curve is κ_L when all three-phonon scattering processes involving an optic phonon are removed.

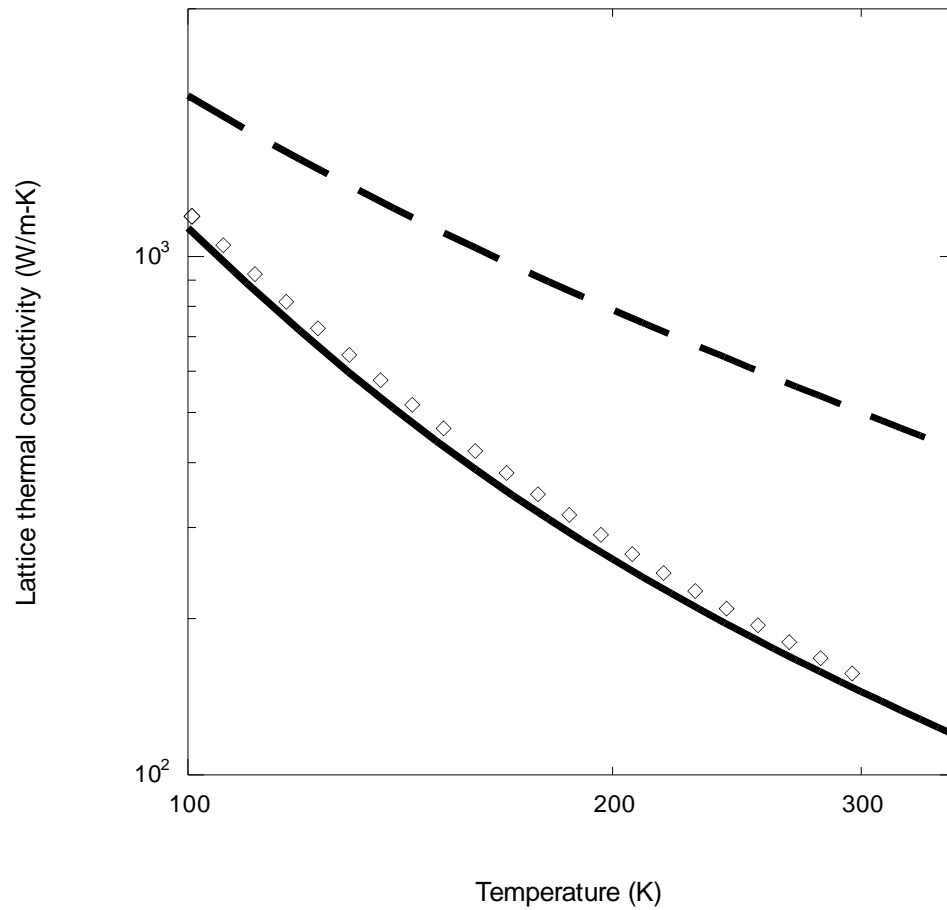**Figure 7-2; Ab initio calculation of κ_L for isotopically enriched silicon (solid curve) compared with the experimentally measured values[20] (open diamonds). The dashed curve is the calculation with all scattering channels involving an optic phonon removed.**

For silicon, removing optic mode scattering increases the room temperature isotopically enriched κ_L from 145W/m-K to 500W/m-K. As the temperature is decreased, the isotopic impurity scattering becomes more dominant as three-phonon scattering processes get frozen out; those involving an optic phonon are the first to be frozen out. This means that the two curves converge as they are both dominated by the same impurity scattering.

Figure 7-3 shows the temperature dependence of κ_L for isotopically pure and enriched diamond. As for silicon, the solid and long-dashed curves show the ab initio calculations of κ_L for the isotopically enriched sample, with and without scattering channels involving an optic phonon. The open diamonds are the measured values.[98] The short-dashed and dashed-dotted curves are the ab initio calculation of the isotopically pure sample with and without three-phonon scattering processes involving an optic phonon.
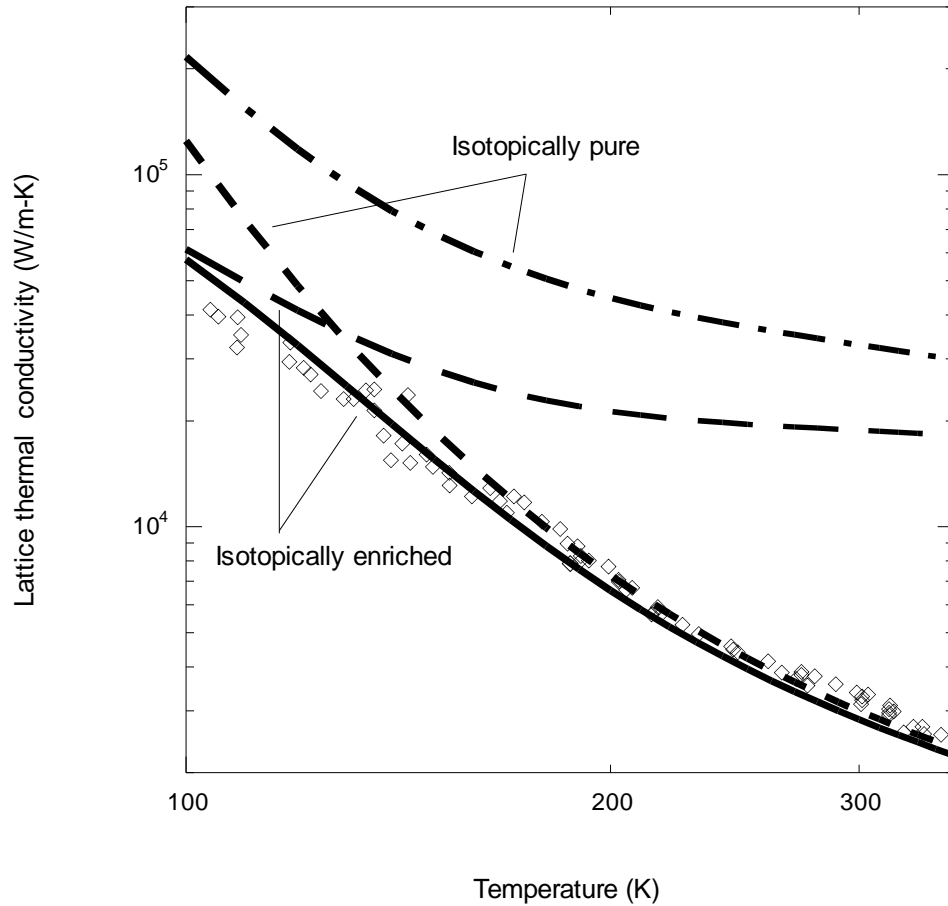

Figure 7-3; Ab initio calculation of κ_L for isotopically enriched (solid curve) and isotopically pure (short-dashed curve) diamond compared with the experimentally measured values[98] (open diamonds). Also plotted are the calculations with all scattering channels involving an optic phonon removed for the enriched (long-dashed curve) and pure (dashed-dotted curve) samples.

The effect of removing scattering channels involving an optic phonon is more striking for diamond. The room temperature value of κ_L for the isotopically enriched sample increases from 2833W/m-K to 18813W/m-K. κ_L for the isotopically pure sample is increased from 2996W/m-K to 32870W/m-K, more than an order of magnitude increase. From Table 7-1 it is clear that the removal of optic scattering channels should have a greater effect on diamond than on silicon, as nearly 90% of the scattering processes in diamond involve an optic phonon. As the temperature is decreased, the curves for isotopically enriched and pure diamond converge as in the silicon case. It should be noted that following the discussion in section 6.5, the converged value is significantly larger than the zeroth-order solution and so these results represent a divergence in κ_L when optic scattering channels are removed.

The difference between κ_L calculated with and without optic phonon scattering channels increases with temperature for all of the plotted cases. This reflects the fact that as temperature increases, the strength of the optic phonon scattering channels is enhanced as their populations increase.

The other striking feature of Figure 7-3 is that the isotopically enriched diamond with the optic scattering channels removed appears to show very weak temperature dependence. At high temperature, the temperature dependence of κ_L enters through the scattering time τ. The temperature dependence of τ is given by

$$\tau_j(\vec{q}) \sim TF_{\lambda\beta} \sim \frac{n_\lambda^0(n_\lambda^0+1)}{Q_\lambda}$$

7.4-1

If isotopic scattering is the only scattering mechanism considered, then $Q_\lambda \sim n_\lambda^0(n_\lambda^0+1)$ and so the scattering time becomes temperature independent. The weak temperature dependence of the isotopically enriched curve with the optic scattering channels removed in Figure 7-3 suggests that the three-phonon scattering is very weak and the impurity scattering is playing a more dominant role. As a result of the unusually small phase space for umklapp scattering in diamond, the removal of optic scattering channels reduces even further the ability of umklapp scattering to limit κ_L. This

behavior is not mirrored in silicon as umklapp scattering remains the dominant mechanism in this case.

7.5 Room temperature relaxation times

7.5.1 Constructing the relaxation times

In order to confidently use RTAs for the calculation of κ_L at temperatures around room temperature and above, the forms for τ cannot be derived using low temperature/small phonon frequency approximations. Also, the optic phonons have been shown to be critical in providing channels for three-phonon scattering and so cannot be omitted from the calculations.

In the calculation of κ_L, a phonon relaxation time, $\tau_{j\beta}(\vec{q})$ is calculated. The acoustic/optic channels and the normal/umklapp processes can be isolated in the calculation of the zeroth-order value of $\tau_{j\beta}(\vec{q})$, but not for iterated values; the iteration procedure couples together the different processes. For this reason, all the RTA results are derived from the zeroth-order solution.

To maintain consistency with previous RTA studies, the relaxation time is written as a product of temperature and frequency dependent parts, $\tau^{-1} \sim f(\omega)g(T)$. In the BTE formalism, the relaxation times take the form, $\tau^{-1}_{\lambda(N,U)} \sim n_\lambda^0(n_\lambda^0 + 1)/Q_{\lambda(N,U)}$, where the N and U refer to the normal and umklapp scattering processes. At high temperature, the Bose factors, $n_\lambda^0 \sim k_B T/\hbar\omega_\lambda$ allowing the separation of the frequency and temperature. This separation at low temperatures requires a low frequency approximation, in order to satisfy $\hbar\omega_\lambda/k_B T \ll 1$. The frequency dependent part is assumed to have the form, $f(\omega) = \omega^n$, where n is a constant to be determined with the constraint that the total relaxation time has $n \leq 2$ at small frequencies to avoid a divergence in κ_L. Figure 7-4 shows the ab initio data for the longitudinal normal relaxation time $\tau_N^L(\omega)$ as a function of frequency for silicon at 300K. The solid line represents a function, $\tau_N^{-1} \sim \omega^2$.
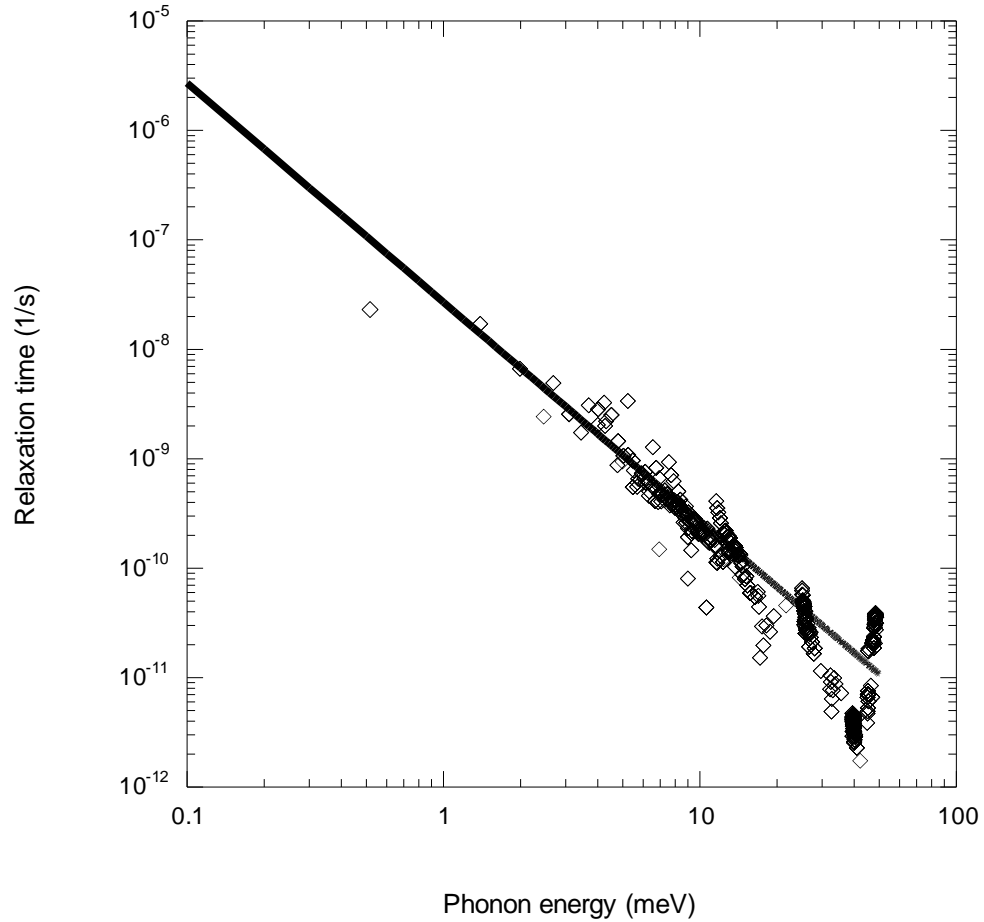
Figure 7-4; Longitudinal normal relaxation time versus frequency for silicon at 300K.

The data is generated using a non-uniform Gaussian grid with sixteen Gaussian points in the first eighth of the Brillouin zone and sixteen points in the final seven-eighths of the Brillouin zone. Despite the denser Gaussian grid close to zone center, the data is still heavily weighted towards high frequencies. This is a result of the scattering time being a function of the phonon wavevector $\vec{q}$, not the frequency ω. Further away from the zone center, the constant $|\vec{q}|$ surface increases in size and it is expected that at each $|\vec{q}|$ value, the number of distinct values of ω associated with it increases. This is observed as a larger spread in the data at large frequencies in Figure 7-4.

The function $\tau_N^{-1} \sim \omega^2$ provides a good fit to the ab initio data for the majority of the frequency range. The spread in data increases as temperature decreases, so the fit to the data is best at high temperatures and becomes poor for low temperatures. This becomes clear in the next figure.

133

The exponent n is determined for all four combinations of transverse/longitudinal and normal/umklapp processes, for silicon and germanium at approximately sixty-five different temperatures in the approximate range dictated by each materials Debye temperature, $\Theta_D/10$ to $2\Theta_D$. Figure 7-5 shows the temperature dependence of the power law exponents for the transverse normal mode (bottom curves) and the transverse umklapp mode (top curves) for silicon (solid curves) and germanium (dashed curves).
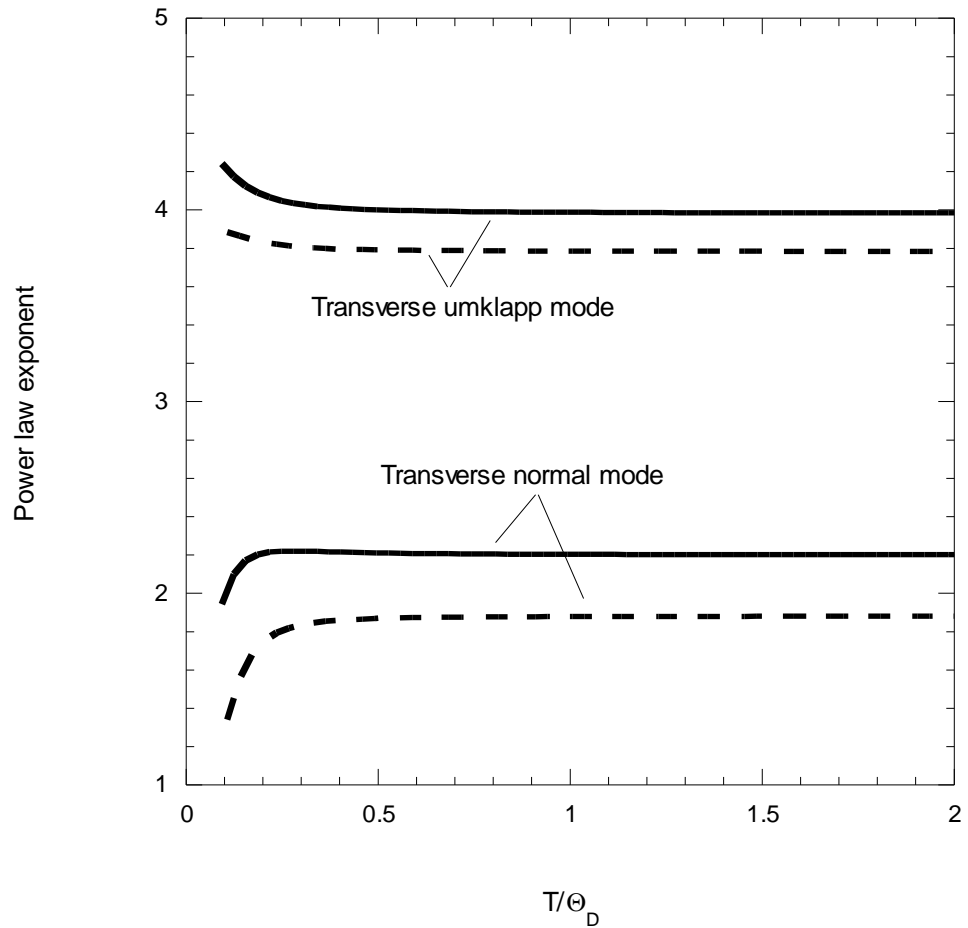

Figure 7-5; Power law exponents as a function of temperature for silicon (solid curves) and germanium (dashed curves) for the transverse normal (lower curves) and transverse umklapp (upper curves) modes.

The power law exponents appear to be well defined for temperatures of the order 0.4 Θ_D and above, but not below. At lower temperatures, the ab initio scattering time data has a larger spread, so the determined value of n is less well fit to the data. This behavior also demonstrates that the assumption that the dependence on frequency and temperature can be separated is breaking down and n is acquiring temperature dependence. In this limit, the high temperature RTA is no longer valid. The desired RT model is intended to be valid at room temperature and above and the exponents extracted from Figure 7-5 can be used in this limit with confidence. In all cases, the exponents are close to integral values (1.8 and 3.78 for the transverse normal and umklapp processes respectively are the furthest from integral values) and so for simplicity, integral values are assumed. For all normal scattering channels, $n = 2$ and for all umklapp channels, $n = 4$.

Motivated by previous forms, the temperature dependence of the relaxation time is assumed to be described by one of the following forms

1. $g(T) \sim AT$

2. $g(T) \sim AT exp\left[-B/T\right]$

3. $g(T) \sim AT^2 exp[-BT]]$

4. $g(T) \sim AT(1 - exp[-BT])$

where A and B are coefficients to be determined and T is the temperature. Several of these forms produce very good fits to the data, but the fourth is consistently the best for all of the scattering processes and branches. This form also shows the physically realistic property that in the limit of high temperature, the correct $\kappa \sim \tau \sim T^{-1}$ is recovered. In order to maintain generality in the form of the relaxation times for different materials, the parameter B is cast in terms of the Debye temperature, $B = \gamma/\Theta_D$. For both silicon and germanium, the parameter γ is determined to be close to three. The final forms of the relaxation times can finally be defined as

$$\tau_{TN}^{-1} = A_{TN}(\hbar\omega)^2 T \left(1 - exp\left[-\frac{3T}{\Theta_D}\right]\right)$$

$$\tau_{LN}^{-1} = A_{LN}(\hbar\omega)^2 T \left(1 - exp\left[-\frac{3T}{\Theta_D}\right]\right)$$

$$\tau_{TU}^{-1} = A_{TU}(\hbar\omega)^4 T \left(1 - exp\left[-\frac{3T}{\Theta_D}\right]\right)$$

$$\tau_{LU}^{-1} = A_{LU}(\hbar\omega)^4 T \left(1 - exp\left[-\frac{3T}{\Theta_D}\right]\right)$$

7.5-1

where the only remaining unknowns are the material dependent coefficients, $\{A\}$. In the literature, different methods of calculating the Debye temperature have been employed. Previous RTA calculations involve an integral over the Debye sphere; the limits of integration being determined by the Debye temperature. The typical value of Θ_D is in this case, far too large when only considering acoustic modes. To address this, a mode specific Debye temperature[96] can be defined by

$$\Theta_i = \left(\frac{\Theta\pi^2}{V}\right)\frac{\hbar v_i}{k_B}$$

7.5-2

where v_i is the velocity of the ith mode. This is often combined with an average velocity, resulting in a Debye temperature that is still too large for the transverse acoustic modes. Another method[118] of calculating a mode Debye temperature is to use the zone boundary frequency, ω_{max}.

$$\Theta_D = \frac{\hbar\omega_{max}}{k_B}$$

7.5-3

In this study, the conventional Debye temperature as derived in specific heat measurements is used (this is a lot higher than the "temperature" of the highest acoustic phonons). The role of the Debye temperature is to set the scale of the energies involved in the relaxation times. In previous RTAs, only the acoustic modes are considered and so this scale is set by the acoustic phonons. In this room temperature RTA, however, the optic phonons are of crucial importance and so the energy scale needs to reflect their influence.

Initial estimates of the coefficients are attained by fitting the ab initio scattering time data with $\tau^{-1}(\omega, T) = Af(\omega)g(T)$, where the forms of $f(\omega)$ and $g(T)$ are known at a given temperature.

Guided by these values, each branch contribution to the total κ_L is calculated using the high temperature RTA for a large range of normal and umklapp coefficients. For each pair of coefficients, the absolute value of the difference between the RTA and ab initio calculations of κ_L is determined. This difference is plotted for the longitudinal branch in silicon at 300K in Figure 7-6.
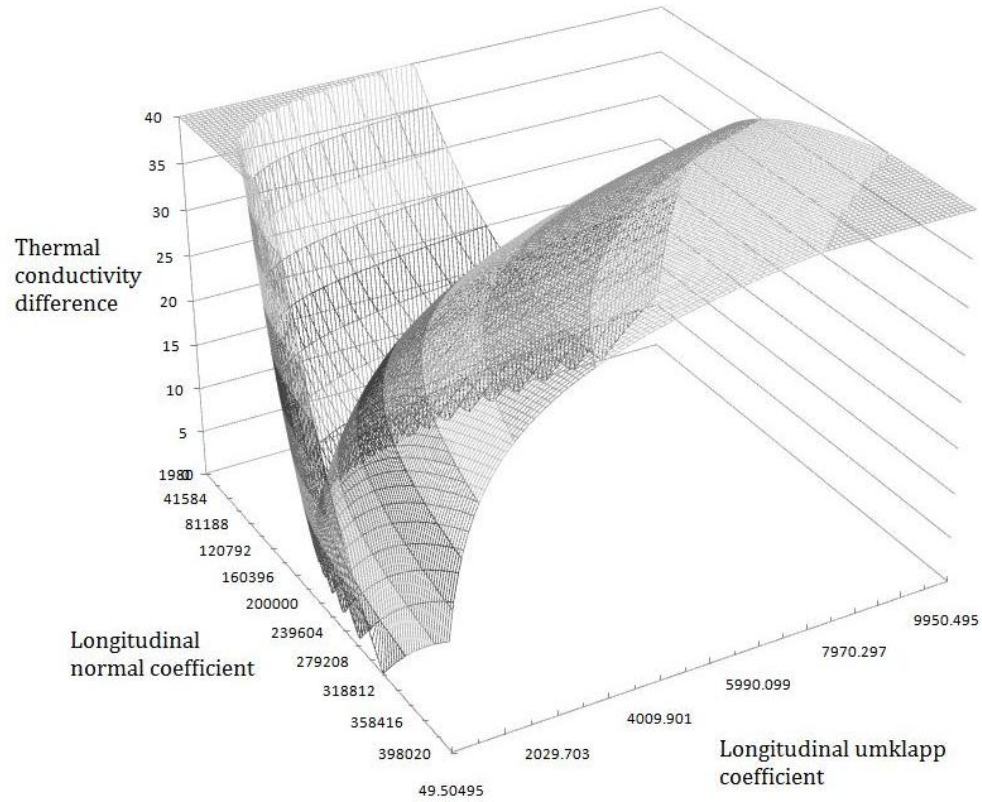

Figure 7-6; The longitudinal normal and umklapp coefficient space for silicon at 300K. The surface height represents the absolute value of the difference between the RTA and ab initio κ_L calculations. The trough in the surface represents the values of A_{LN} and A_{LU} that give rise to the same branch contribution to κ_L as the zeroth-order ab initio BTE calculations.

The trough in Figure 7-6 represents the combination of coefficients that give rise to the exact solution found by the zeroth-order ab initio BTE calculations. The coefficients that give rise to the best visual fit to the ab initio data at several temperatures (as an example, see Figure 7-4) and lie on the trough in Figure 7-6 are selected. The coefficients found for the two transverse branches are very

close and so they are combined into a single transverse branch, whose coefficients are the average of those found for the two individual branches.

The values of the coefficients found in this manner and the power law exponents for silicon and germanium are presented in Table 7-2.

	Normal processes			Umklapp processes		
	$(\hbar\omega)^x$	A_{TN} s^{-1} meV^{-2} K^{-1}	A_{LN} s^{-1} meV^{-2} K^{-1}	$(\hbar\omega)^x$	A_{TU} s^{-1} meV^{-4} K^{-1}	A_{LU} s^{-1} meV^{-4} K^{-1}
Si	2	253322	163921	4	2012	507
Ge	2	460248	401980	4	8634	1990

Table 7-2; The power law coefficients and exponents for the normal and umklapp processes in the TA and LA branches of silicon and germanium.

With all of the parameters established, the RTA forms developed can be used for calculating κ_L.

7.5.2 Room temperature and above RTA results

The integral equation for κ_L in equation 3.2-5 is solved with the form of the relaxation time, $\tau_{\lambda\alpha}$ being the combination of the normal and umklapp scattering contributions combined according to Matthiessen's rule (equation 7.3-1). Figure 7-7 compares the ab initio calculations of the TA and the LA branches of silicon with the RTA calculations.

The coefficients $\{A\}$ are optimized to fit the 300K data and so the agreement for the longitudinal branch at 300K is exact. Since the two transverse branches are treated with one set of parameters, one is over and the other under predicted. The sum of the branches agrees exactly with the sum of the ab initio transverse branches at 300K. Over the temperature range considered, the agreement between the zeroth-order ab initio BTE and RTA calculations is remarkably good. At low temperatures, some deviation between the curves is evident as is expected for a high temperature RTA.

The contribution to κ_L from the optic branches has not been included in the results for the RTA. At 300K, κ_L is approximately 145W/m-K for silicon. Excluding the optic modes, the corresponding value of κ_L is approximately 138W/m-K, a decrease of less than 5%, a level of error acceptable in an RTA calculation. Note that the optic branches are still present in their capacity to provide scattering channels for the acoustic phonons.
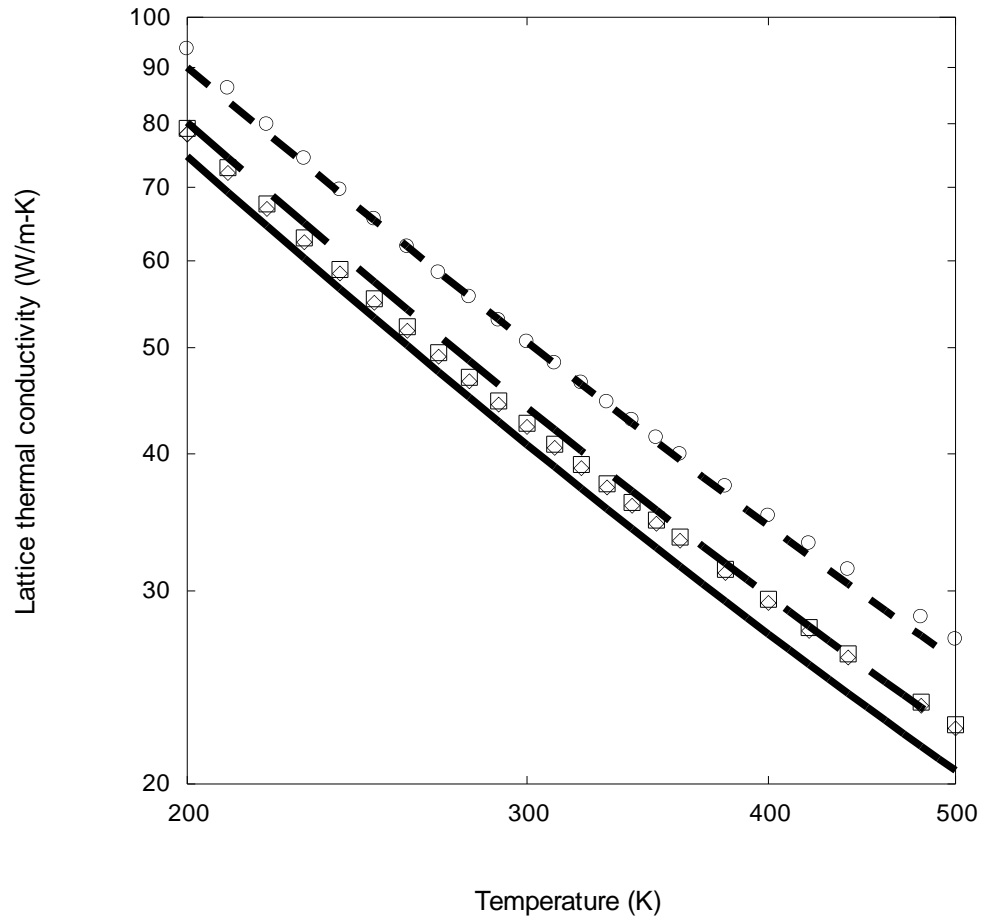

Figure 7-7; Temperature dependence of the RTA calculations of κ_L of the TA (solid and long-dashed curves) and the LA (short-dashed curve) branches of silicon compared with the zeroth-order ab initio BTE calculations (open diamonds, open squares and open circles).

A comparison of the RTA and ab initio BTE calculations of κ_L for silicon and germanium are shown in Figure 7-8 and Figure 7-9 respectively. The open diamonds are the *converged* ab initio BTE

calculations (not the zeroth-order calculations used to derive the RTA) *including* the optic branches, the open squares are the zeroth-order ab initio BTE calculations with the optic modes omitted and the solid curves are the RTA results. The dashed curves are the RTA calculations when the coefficient of umklapp scattering is set to zero.
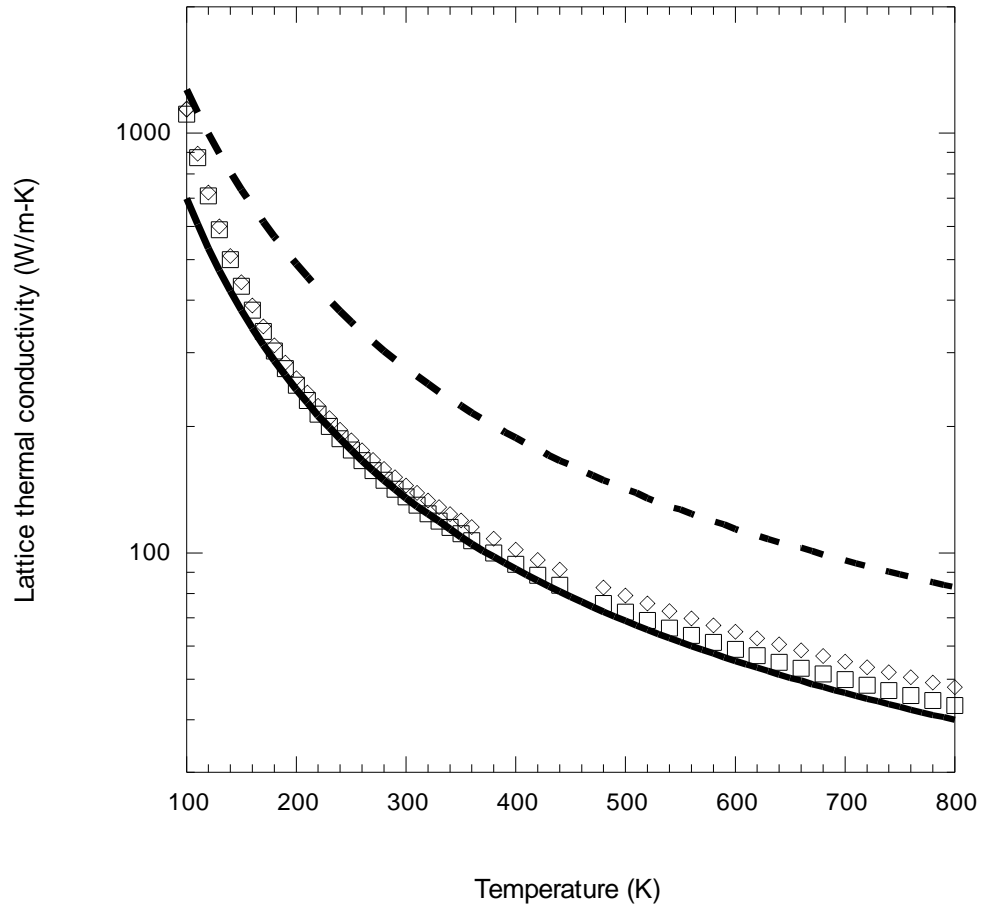

Figure 7-8; Temperature dependence of κ_L for silicon. Included are the full ab initio BTE calculations including all branches (open diamonds), the ab initio zeroth-order BTE calculations with the optic branches omitted (open squares) and the RTA results (solid curve). The dashed curve represents the RTA results with umklapp scattering removed.

Figure 7-9; Temperature dependence of κ_L for germanium. Included are the full ab initio BTE calculations including all branches (open diamonds), the ab initio zeroth-order BTE calculations with the optic branches omitted (open squares) and the RTA results (solid curve). The dashed curve represents the RTA results with umklapp scattering removed.
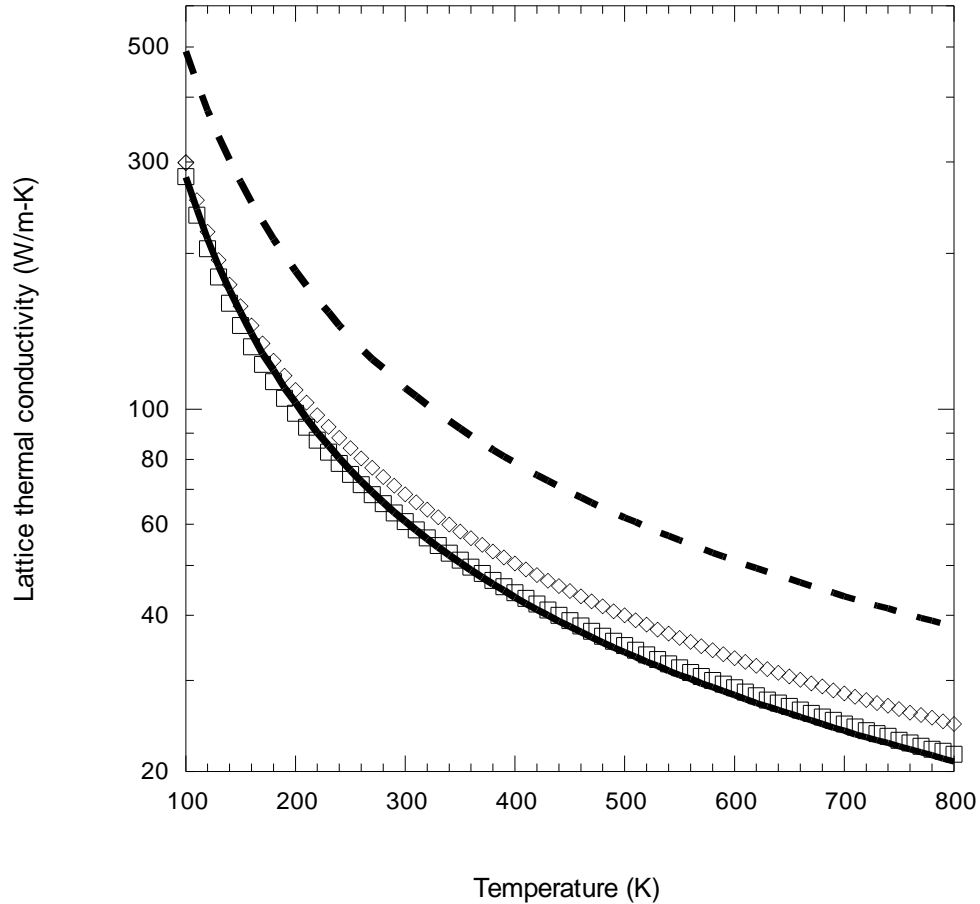
The agreement between the RTA calculations and the zeroth-order ab initio data is extremely good over the large temperature range considered.

The dashed curves represent the value of κ_L if umklapp scattering is removed. For both materials, an approximate doubling of κ_L results from removing the umklapp scattering processes. This demonstrates that frequencies away from zone center (where umklapp scattering becomes significant) still contribute significantly to κ_L. Close to the zone center, the number of channels available for umklapp scattering is very limited and so it is expected that normal processes will

dominate the behavior of κ_L in this region. With increasing $\vec{q}$ and ω, the dominance should smoothly move to umklapp scattering, leading to the physical expectation that the umklapp relaxation time should have a higher power dependence on the frequency, as observed. In Figure 7-10, this behavior is demonstrated for a transverse acoustic branch at 300K in silicon. The solid curve is the total relaxation time, constructed from the normal (long-dashed curve) and umklapp (short-dashed curve) relaxation times using Matthiessen's rule (equation 7.3-1)
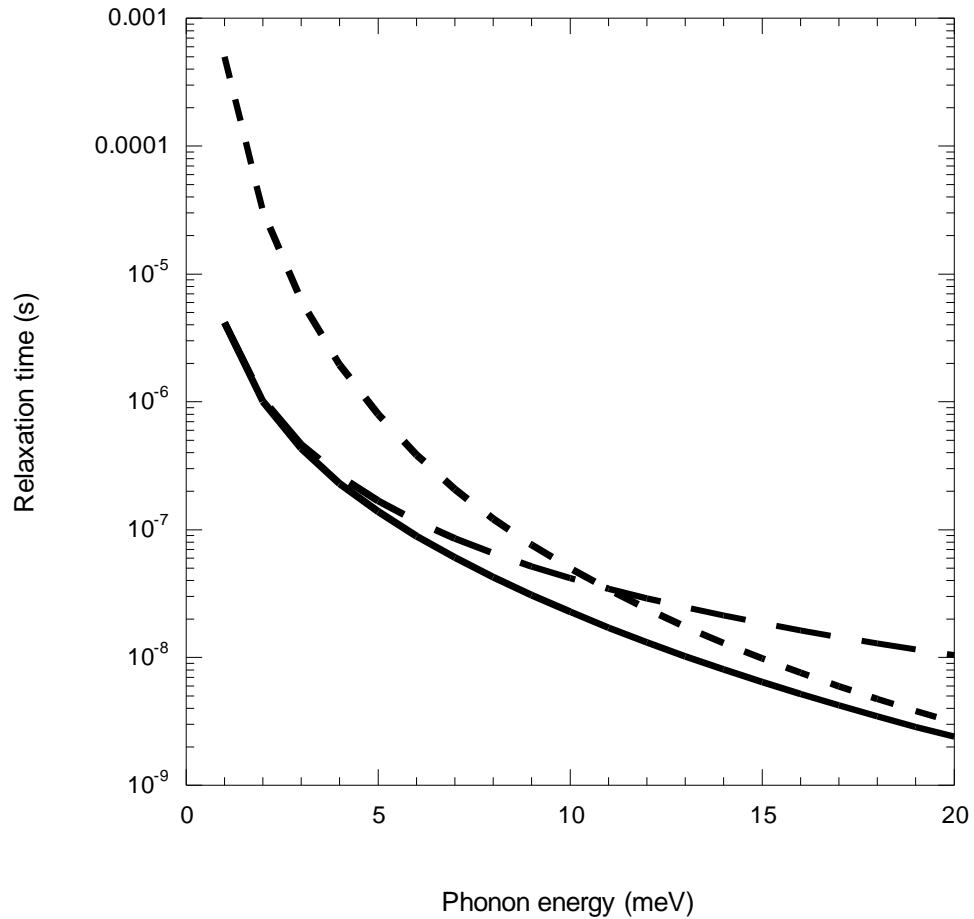

Figure 7-10; The dependence of the normal (long-dashed curve), umklapp (short-dashed curve) and the total (solid curve) relaxation times on the phonon frequency (energy) for branch 1 in silicon at 300K.

At low phonon frequencies, the total relaxation time is equal to the normal relaxation time. With increasing frequency, the ω^4 dependence of the umklapp relaxation time ensures the umklapp relaxation time approaches and then surpasses the normal relaxation time in dominance. This physically realistic crossover behavior is common to all the branches.

8 Conclusions

An iterative solution to the linearized Boltzmann transport equation has been developed that explicitly accounts for the intrinsic three-phonon scattering by way of third-order anharmonic interatomic force constants as well as isotopic impurity and boundary scattering.

This was used in conjunction with a set of commonly used empirical interatomic potentials to calculate the thermal conductivity. The comparison with experimental data for silicon was poor for all models. The reason for the poor performance of these potentials was their inability to accurately describe the phonon dispersion curves and account for the crystal anharmonicity.

The adiabatic bond charge model, which does an excellent job of reproducing phonon dispersion curves for the considered materials was then used to investigate the thermal conductivity of Si/Ge superlattices. Increasing the mass ratio between constituent atoms and the superlattice order was shown to decrease the thermal conductivity, but by a smaller amount than suggested by constant relaxation time methods or by using the Keating interatomic potential. The necessity of accurate descriptions of the phonon properties was thus confirmed. By comparison with experimental data for GaAs/AlAs superlattices, the strength of extrinsic scattering processes, specifically interface scattering, was shown to be much larger than previously assumed.

The main outcome of this work, however, was the development of a theoretical construct in which parameter-free lattice thermal conductivity calculations can be performed. This was achieved by combining the power of density functional perturbation theory in calculating the microscopic interatomic forces with the full solution to the Boltzmann transport equation. The phonon dispersions, Grüneisen parameters, linear thermal expansion coefficients and thermal conductivities of several group IV and III-V semiconductors were calculated and compared with measured values. The calculations were, for the most part, in very good agreement with experiment. This is especially true for the group IV materials. The unusual behavior of diamond was considered a stringent test of the method, and the calculated properties were again in good agreement with measurement. The predictive capacity of the theoretical approach was thus validated.

144

Due to the computational complexity of the ab initio approach, a relaxation time approximation method was developed for use at room temperatures and above. The relaxation times were based on the calculated ab initio data and were free of the restrictive approximations that are commonly employed. The crucial role played by optic phonons was also highlighted. The thermal conductivities calculated using the high temperature forms showed good agreement with the ab initio data over a wide range of temperatures, suggesting that the employed forms are physically reasonable.

9 Acknowledgements

I would like to acknowledge significant and ongoing support from my advisor David Broido. I was never lacking for guidance and support in all aspects of life at Boston College. Many discussions on the physics involved in this study as well as computational methods with both David Broido and Lucas Lindsay were indispensable in the course of the PhD.

The anharmonic IFC calculations were all performed using a Fortran program developed by D. Strauch's group at the University of Regensburg. I am indebted to the work of this group in developing this program and allowing me to utilize it in the thermal conductivity calculations presented herein. I am also indebted to Derek Stewart for (amongst other things) setting the program up on the Boston College computational cluster and aiding in its operation. Derek also provided much support in regards to the Quantum-Espresso ab initio package and general discussions on the work undertaken.

The extent of the work performed here would have been impossible without the support of Barry Schaudt and the Boston College computing cluster. The computational expense of the calculations herein is vast and would not have been achievable without the available resources provided by them.

I would also like to thank the National Science Foundation, the American Chemical Society Petroleum Research Fund and Boston College for financial support of this research.

Many members of the Physics department have provided support, distraction and kept me sane. Special mention must go to Joyce Light, Nancy Chevry, Jan Engelbrecht, Andrzej Herczynski and Cy Opeil.

For much of my time at Boston College, I have developed interests in new pastimes, art forms and distractions entirely due to the enthusiasm and companionship of Kristie Loncich. My time at Boston College would have been much the worse in her absence and I am glad for all that I have experienced with her and who she has helped me become.

I cannot omit the friends that I have come to rely on in Boston, both for their support when I needed it and for making my experience so memorable and a time I will always look back on with

fond memories. Specifically and in no particular order, Francis and Liang Niestemski, Brian and Lisa Morrison, Lucas and Louise Lindsay (and obviously Eliza), Kevin and Heather Sullivan, John Feldmann, Frank Bello, Ryan and Fumi Johnson and everyone else who has helped make my time here so enjoyable.

Last, but certainly not least, my parents, Ian and Elaine Ward have always supported me; first in my decision to come to study in America and then with all aspects of my life. Without the unconditional backing that I know that I can count on from both my parents and the rest of my family, completing this part of my studies would have been very difficult.

[1] P. G. Klemens, Proc. Roy. Soc. (London) **A208**, 108 (1951).

[2] J. Callaway, Phys. Rev. **113**, 1046 (1958).

[3] M. Asen-Palmer, K. Bartkowski, E. Gmelin, M. Cardona, A. P. Zhernov, A. V. Inyushkin, A. Taldenkov, V. I. Ozhogin, K. M. Itoh, and E. E. Haller, Phys. Rev. B **56**, 9431 (1997).

[4] A. J. C. Ladd, B. Moran and W. G. Hoover, Phys. Rev. B **34**, 5058 (1986).

[5] J. E. Turney, E. S. Landry, A. J. H. McGaughey and C. H. Amon, Phys. Rev. B **79**, 064301 (2009).

[6] M. Omini and A. Sparavigna, Phys. Rev. B **53**, 9064 (1996).

[7] D. A. Broido, A. Ward and N. Mingo, Phys. Rev. B **72**, 014308 (2005).

[8] D. G. Cahill, W. K. Ford, K. E. Goodson, G. D. Mahan, A. Majumdar, H. J. Maris, R. Merlin and S. R. Phillpot, J. Appl. Phys., **93**, 793 (2003).

[9] G. D. Mahan, B. Sales and J. Sharp, Phys. Today **50** (3), 42 (1997).

[10] F. Di Salvo, Science **285**, 703 (1999).

[11] W. Weber. Phys. Rev. B **15**, 4789 (1976).

[12] W. Weber and K. C. Rustagi, Solid State Commun. **18**, 673 (1976).

[13] A. Ward and D. A. Broido, Phys. Rev. B **77**, 245328 (2008).

[14] W. E. Bies, R. J. Radtke and H. Ehrenreich, J. Appl. Phys. **88**, 1498 (2000).

[15] M. T. Yin and M. L. Cohen, Phys. Rev. B **26**, 3259 (1982).

[16] P. Giannozzi, S. de Gironcoli, P. Pavone and S. Baroni, Phys. Rev. B **43**, 7231 (1990).

[17] S. Baroni, S. de Gironcoli, A. Dal Corso and P. Gianozzi, Rev. Mod. Phys. **73**, 515 (2001).

[18] X. Gonze and J. –P. Vigneron, Phys. Rev. B **39**, 13120 (1989).

[19] G. Deinzer, G. Birner and D. Strauch, Phys. Rev. B **67**, 144304 (2003).

[20] A.Y. Inyushkin, A. N. Taldenkov, A. M. Gibin, A. V. Gusev and H. J- Pohl, Phys. Stat. Sol. (c) **1**, 2995 (2004).

[21] R. P. Joshi, P. G. Neudeck and C. Fazi, J. Appl. Phys. **88**, 265 (2000).

[22] R. A. Coldwell-Horsfall, Phys. Rev. **129**, 22 (1962).

[23] D. J. Ecsedy and P. G. Klemens, Phys. Rev. B **15**, 5957 (1977).

[24] V. I. Ozhogin, A. V. Inyushkin, A. N. Taldenkov, A. V. Tikhomirov and G. E. Popov, JETP Lett. 63, 490 (1996).

[25] T. Ruf, R. W. Henn, M. Asen-Palmer, E. Gmelin, M. Cardona, H.-J. Pohl, G. G. Devyatych, and P. G. Sennikov, Solid State Commun. **115**, 243 (2000).

[26] W. S. Capinski, H. J. Maris, E. Bauser, I. Silier, M. Asen-Palmer, T. Ruf, M. Cardona, and E. Gmelin, Appl. Phys. Lett. **71**, 2109 (1997).

[27] R. Berman, P. R. W. Hudson and M. Martinez, J. Phys. C: Solid State Phys. **8**, L430 (1975).

[28] R. Berman, Phys. Rev. B **45**, 5726 (1992).

[29] Online archive on physical properties of semiconductors at www.ioffe.ru/sva/nsm/semicond/index.html.

[30] J. Fabian and P. B. Allen, Phys. Rev. Lett. **79**, 1885 (1997).

[31] P. K. Schelling, S. R. Phillpot and P. Keblinski, Phys. Rev. B **65**, 144306 (2002).

[32] L. Sun and J. Y. Murthy, Appl. Phys. Lett. **89**, 171919 (2006).

[33] J. E. Turney, E. S. Landry, A. J. H. McGaughey and C. H. Amon, Phys. Rev. B **79**, 064301 (2009).

[34] P. N. Keating, Phys. Rev. **145**, 637 (1966).

[35] J. Tersoff, Phys. Rev. B **37**, 6991 (1987).

[36] J. Tersoff, Phys. Rev. B **38**, 9902 (1988).

[37] G. Dolling, "*Symposium on Inelastic Scattering of Neutrons in Solids and Liquids*" (IAEA, Vienna, 1968), Vol. II, p. 37.

[38] F. H. Stillinger and T. A. Weber, Phys. Rev. B **31**, 5262 (1985).

[39] M. Z. Bazant, E. Kaxiras and J. F. Justo, Phys. Rev. B **56**, 8542 (1997).

[40] J. F. Justo, M. Z. Bazant, E. Kaxiras, V. V. Bulatov and S. Yip, Phys. Rev. B **58**, 2539 (1998).

[41] J. C. Phillips, Phys. Rev. **166**, 832 (1968).

[42] R. M. Martin, Phys. Rev. **186**, 871 (1969).

[43] A. A. Maraduduin et al., Solid State Physics, Vol. Suppl. 3. (Academic, New York) (1971).

[44] G. Dolling, *Inelastic Scattering of Neutrons in Solids and Liquids* (IAEA, Vienna, 1963), Vol. I, p. 37.

[45] G. Nilsson and G. Nelin, Phys. Rev. B **3**, 364 (1971).

[46] G. Nelin and G. Nilsson, Phys. Rev. B **5**, 3151 (1972).

[47] G. Nilsson and G. Nelin, Phys. Rev. B **6**, 3777 (1972).

[48] A. A. Maradudin, *Dynamical Properties of Solids.* [ed.] A.A. Maradudin G.K. Horton. s.l. : North Holland, Amsterdam, 1974. pp. 3-82.

[49] D. Strauch and B. Dorner, J. Phys.: Condens. Matter **2**, 1457 (1990).

[50] L. Colombo and P. Giannozzi, Solid State Comm. **96**, 49 (1995).

[51] P. Hyldgaard and G. D. Mahan, Phys. Rev. B **56**, 10754 (1997).

[52] S. Tamura, Y. Tanaka and H. J. Maris, Phys. Rev. B **60**, 2627 (1999).

[53] D. A. Broido and T. L. Reineke, Phys. Rev. B **70**, 081310(R) (2004).

[54] E. F. Steigmeier and I. Kudman, Phys. Rev. **141**, 767 (1966).

[55] R. Venkatasubramanian, Phys. Rev. B **61**, 3091 (2000).

[56] S. Y. Ren and J. D. Dow, Phys. Rev. B **25**, 3750 (1982).

[57] A. V. Inyushkin, A. N. Taldenkov, A. Yu Yakubovsky, A. V. Markov, L. Moreno-Garsia and B. N. Sharonov, Semicond. Sci. Technol. **18**, 685 (2003).

[58] W. S. Capinski, H. J. Maris, T. Ruf, M. Cardona, K. Ploog and D. S. Katzer, Phys. Rev. B **59**, 8105 (1999).

[59] B. C. Daly, H. J. Maris, K. I. Imamura and S. Tamura, Phys. Rev. B **66**, 024301 (2002).

[60] P. Hohenberg and W. Kohn, Phys. Rev. **136**, B864 (1964).

[61] W. Kohn and L. J. Sham, Phys. Rev. **140**, A1133 (1965).

[62] D. M. Ceperley and B. J. Alder, Phys. Rev. Lett. **45,** 566 (1980).

[63] J. Perdew and A. Zunger, Phys. Rev. B **23**, 5048 (1981).

[64] J. P. Perdew and Y. Wang, Phys. Rev B **45** 13244 (1992).

[65] J. P. Perdew, K. Burke and M. Ernzerhof, Phys. Rev. Lett. **77** 3865 (1996).

[66] A. Dal Corso, Science and supercomputing at CINECA – Report 2001.

[67] H. Hellmann, *Einführung in die Quantenchemie* (Deuticke & Co., Leipzig, 1937).

[68] R. P. Feynman, Phys. Rev. **56**, 340 (1939).

[69] P. Pulay, Mol. Phys. **17**, 197 (1969).

[70] A. A. Quong and B. M. Klein, Phys. Rev. B **46**, 10734 (1992).

[71] S. de Gironcoli, Phys. Rev. B **51**, 6773 (1995).

[72] M. Born and K. Huang, *Dynamical theory of Crystal Lattices* (Oxford University Press, Oxford) (1954).

[73] W. Cochran and R. A. Cowley, J. Phys. Chem. Solids **23**, 447 (1962).

[74] R. D. King-Smith and D. Vanderbilt, Phys. Rev. B **47**, 1651 (1993).

[75] R. Resta, Rev. Mod. Phys. **66**, 899 (1994).

[76] G. B. Bachelet, D. R. Hamann and M. Schlüter, Phys. Rev. B **26**, 4199 (1982).

[77] L. I. Schiff, *Quantum Mechanics* (McGraw-Hill, New York, 1968).

[78] R. W. Shaw and W. A. Harrisson, Phys. Rev. **163**, 604 (1967).

[79] M. Malorny, *Theorie und Numerik von nicht-linearen Kumulanten höherer Ordnung*, PhD thesis, University of Regensburg, 2008.

[80] P. Giannozzi et. al. http://www.quantum-espresso.org.

[81] S. Baroni, P. Giannozzi and A. Testa, Phys. Rev. Lett. **58**, 1861 (1987a).

[82] X. Gonze, Phys. Rev. A **52**, 1096 (1995b).

[83] E. N. Zein, Phys. Solid State **26**, 1825 (1984).

[84] D. A. Broido, M. Malorny, G. Birner, N. Mingo and D. A. Stewart, Appl. Phys. Lett. **91**, 231922 (2007).

[85] S. Wei and M. Y. Chou, Phys. Rev. Lett. **69**, 2799 (1992).

[86] B. A. Weinstein and G, J, Piermarini, Phys. Rev. B **12**, 1172 (1975).

[87] G. A. Slack and S. F. Bartram, J. Appl. Phys. **46**, 89 (1975).

[88] P. Pavone, K. Karch, O. Schütt, W. Windl, D. Strauch, P. Giannozzi and S. Baroni, Phys. Rev. B **48**, 3156 (1993).

[89] N. Mounet and N. Marzari, Phys. Rev. B **71**, 205214 (2005).

[90] G. Nilsson and G. Nelin, Phys. Rev. B **3**, 364 (1971).

[91] J. L. Warren, J. L. Yarnell, G. Dolling and R. A. Cowley, Phys. Rev. **158**, 805 (1967).

[92] H. J. McSkimin, J. Appl. Phys, **24**, 988 (1953).

[93] H. J. McSkimin and P. Andreatch Jr., J. Appl. Phys. **34**, 651 (1963).

[94] H. J. McSkimin, P. Andreatch Jr. and P. Glynn, J. Appl. Phys. **43**, 985 (1972).

[95] S. S. Mitra, O. Brafman, W. B. Daniels and R. K. Crawford, Phys. Rev. **186**, 942 (1969).

[96] J. R. Olson, R. O. Pohl, J. W. Vandersande, A. Zoltan, T. T. Anthony and W. F. Banholzer, Phys. Rev. B **47**, 14850 (1993).

[97] D. G. Onn, A. Witek, Y. Z. Qiu, T. R. Anthony and W. F. Banholzer, Phys. Rev. Lett. **68**, 2806 (1992).

[98] L. Wei, P. K. Kuo, R. L. Thomas, T. R. Anthony and W. F. Banholzer, Phys. Rev. Lett. **70**, 3764 (1993).

[99] P. H. Borcherds, G. F. Alfrey, D. H. Saunderson and A. D. B. Woods, J. Phys. C: Solid State Phys. **8**, 2022 (1975).

[100] G. P. Kerker, J. Phys. C: Solid State Phys. **13**, L189 (1980).

[101] U. von Barth and R. Car (unpublished) for a brief description of this method, see A. Dal Corso, S. Baroni, R. Resta and S. de Gironcoli, Phys. Rev. B **47**, 3588 (1993).

[102] D. G. Onn, A. Witek, Y. Z. Qiu, T. R. Anthony and W. F. Banholzer, Phys. Rev. Lett. **68**, 2806 (1992).

[103] L. Wei, P. K. Kuo, R. L. Thomas, T. R. Anthony and W. F. Banholzer, Phys. Rev. Lett. **70**, 3764 (1993).

[104] P. H. Borcherds, G. F. Alfrey, D. H. Saunderson and A. D. B. Woods, J. Phys. C: Solid State Phys. **8**, 2022 (1975).

[105] K. Haruna, H. Maeta, K. Ohashi, T. Koike, J. Phys. C: Solid State Phys. **19**, 5149 (1986).

[106] A. V. Inyushkin, A. N. Taldenkov, A. Yu Yakubovsky, A. V. Markov, L. Moreno-Garsia and B. N. Sharonov, Semicond. Sci. Technol. **18**, 685 (2003).

[107] V. M. Muzhdaba, A. Ya. Nashel'skii, P. V. Tamarin and S. S. Shalyt, Sov. Phys. Solid State, **10**, 2265 (1968).

[108] S. A. Aliev, A. Ya. Nashel'skii and S. S. Shalyt, Sov. Phys. Solid State, **7**, 1287 (1964).

[109] P. Debye, *Vorträge über die kinetische Theorie der Materie und der Elektrizität* (Teubner, Leipzig, 1914).

[110] R. Peierls. Ann. Phys. **3**, 1055 (1929).

[111] I. Pomeranchuk, J. Phys. (U.S.S.R) **4**, 259 (1941).

[112] I. Pomeranchuk, J. Phys. (U.S.S.R) **6**, 237 (1942).

[113] I. Pomeranchuk, Phys. Rev. **60**, 820 (1952).

[114] A. Herpin, Ann. Phys **7**, 91 (1952).

[115] C. Herring, Phys. Rev. **95**, 954 (1954).

[116] P. G. Klemens, *Encyclopedia of Physics*, edited by S. Flügge (Springer-Verlag, Berlin, 1956), Vol. 14, p.198.

[117] M. G. Holland, Phys. Rev. **132**, 2461 (1963).

[118] D. T. Morelli, J. P. Heremans and G. A. Slack, Phys. Rev. B **66**, 195304 (2002).